

T-4374

**DETECTION OF SHALLOW SUBSURFACE LAYERS  
BY HIGH-FREQUENCY ELECTROMAGNETIC  
SOUNDING**

**ARTHUR LAKES LIBRARY  
COLORADO SCHOOL OF MINES  
GOLDEN, CO 80401**

by

Duff C. Stewart

ProQuest Number: 10796558

All rights reserved

INFORMATION TO ALL USERS

The quality of this reproduction is dependent upon the quality of the copy submitted.

In the unlikely event that the author did not send a complete manuscript and there are missing pages, these will be noted. Also, if material had to be removed, a note will indicate the deletion.



ProQuest 10796558

Published by ProQuest LLC (2019). Copyright of the Dissertation is held by the Author.

All rights reserved.

This work is protected against unauthorized copying under Title 17, United States Code  
Microform Edition © ProQuest LLC.

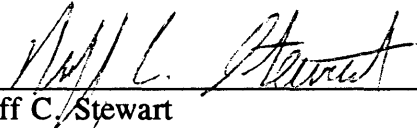
ProQuest LLC.  
789 East Eisenhower Parkway  
P.O. Box 1346  
Ann Arbor, MI 48106 – 1346

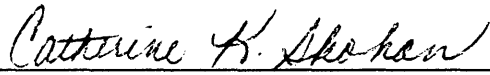
T-4374

A thesis submitted to the faculty and the Board of Trustees of the Colorado School of Mines in partial fulfillment of the requirements for the degree of Doctor of Philosophy (Geophysics).

Golden, Colorado


Date 5/4/93

Signed:   
Duff C. Stewart

Approved:   
Dr. Catherine K. Skokan  
Thesis Advisor

Golden, Colorado

Date May 5, 1993

  
Dr. Phillip R. Romig  
Professor and Head  
Department of Geophysics

## ABSTRACT

Existing surface electromagnetic tools are unsuitable for detailed investigation of the upper 5 to 10 m of the earth or, as with ground-penetrating radar, are only effective in a resistive environment. A new instrument designed for frequency-domain sounding in this depth range uses short coil spacings of 5 m or less, and a frequency range of 300 kHz to 30 MHz. In this frequency range both conduction currents (controlled by electrical conductivity) and displacement currents (controlled by dielectric permittivity) are important.

Most computer programs written for low-frequency electromagnetic modeling neglect displacement currents, and are thus unsuited for accurate high-frequency modeling and interpretation. New forward and inverse computer programs written for high-frequency investigations include displacement currents in layered-earth models. The computer programs and instrument are used to evaluate the effectiveness of shallow high-frequency sounding based on measurement of the polarization ellipse and the spatial gradient of magnetic fields.

Forward model studies show that it is possible to measure the electrical resistivity, dielectric permittivity, and thickness of individual earth layers. The influence of dielectric permittivity provides the ability to resolve thin layers, especially if the instrument frequency range can be extended to 50 MHz.

Field tests of the instrument and inversion program are shown for survey sites located in Colorado, Iowa, and Nevada. These examples demonstrate the potential for detailed shallow mapping with vertical resolution superior to existing low-frequency EM tools. Although data collection and inversion are much slower than for low-frequency methods, additional information is obtained inasmuch as there usually is a dielectric permittivity contrast as well as a resistivity contrast at boundaries between different materials. Determination of dielectric permittivity is particularly valuable for environmental waste applications, where the presence of some contaminants may have little effect on observed resistivity, but a large effect on observed permittivity.

TABLE OF CONTENTS

ABSTRACT . . . . . iii

LIST OF FIGURES . . . . . viii

LIST OF TABLES . . . . . xiii

LIST OF SYMBOLS . . . . . xiv

ACKNOWLEDGMENTS . . . . . xv

INTRODUCTION . . . . . 1

    Limitations of Existing EM Methods . . . . . 2

        In-Situ Probes . . . . . 2

        Ground-Penetrating Radar . . . . . 3

        Time-Domain EM . . . . . 3

        Terrain Conductivity . . . . . 4

    High Frequency Sounding . . . . . 4

        Previous Studies . . . . . 6

    Electrical Properties of Earth Materials . . . . . 7

        Neglect of Frequency Dependence . . . . . 8

THEORY . . . . . 10

    Solving For The Vector Potential . . . . . 15

        The Primary Field Potential . . . . . 15

        The Secondary Field Potential . . . . . 19

        The Total Vector Potential . . . . . 20

    Boundary Conditions and the Electromagnetic Field Equations . . . . . 21

    Skin Depth . . . . . 25

|  |    |
|--|----|
| Computer Modeling Programs . . . . .                               | 29 |
| Modification of the Field Equations . . . . .                      | 29 |
| Forward and Inverse Programs . . . . .                             | 32 |
| Inclusion of the Air Layer . . . . .                               | 32 |
| EM Field Parameters Measured . . . . .                             | 33 |
| The Magnetic Field Polarization Ellipse . . . . .                  | 33 |
| The Spatial Gradient . . . . .                                     | 36 |
| FORWARD MODEL EXAMPLES . . . . .                                   | 38 |
| Half-Space Models: Influence of Dielectric Permittivity . . . . .  | 40 |
| Model 1: Resistive Half-Space . . . . .                            | 40 |
| Model 2: Conductive Half-Space . . . . .                           | 42 |
| Model 3: Effect of Varying Resistivity . . . . .                   | 45 |
| Two-Layer Models . . . . .   | 51 |
| Effect of Top Layer Thickness . . . . .                            | 51 |
| Model 4: Resistive, Low-K Top Layer . . . . .                      | 51 |
| Model 5: Conductive, High-K Top Layer . . . . .                    | 57 |
| Effect of Bottom Layer Electrical Parameters . . . . .             | 62 |
| Model 6: Resistive, Low-K Top Layer, Variable $\rho_2$ . . . . .   | 62 |
| Model 7: Conductive, High-K Top Layer, Variable $\rho_2$ . . . . . | 65 |
| Model 8: Resistive, Low-K Top Layer, Variable $K_2$ . . . . .      | 68 |
| Model 9: Conductive, High-K Top Layer, Variable $K_2$ . . . . .    | 68 |
| Three-Layer Models: Thin Layer Detection . . . . .                 | 76 |
| Models 10 Through 15: Effect of Middle Layer Thickness . . . . .   | 76 |
| Polarization Ellipse Measurements . . . . .                        | 76 |
| Spatial Gradient Measurements . . . . .                            | 81 |
| Effect of Middle Layer Electrical Parameters . . . . .             | 83 |
| Model 16: Variable $\rho_2$ . . . . .                              | 83 |
| Model 17: Variable $K_2$ . . . . .                                 | 86 |
| INSTRUMENTATION . . . . .  | 89 |
| System Description . . . . .                                       | 89 |
| Instrument Problems . . . . .                                      | 92 |
| Instrument Sensitivity . . . . .                                   | 95 |

|  |            |
|--|------------|
| Data Acquisition and Reduction . . . . .   | 96         |
| Polarization Ellipse and Spatial Gradient Calculation . . . . .                  | 98         |
| <b>FIELD SURVEY EXAMPLES . . . . .</b>   | <b>102</b> |
| Colorado School of Mines survey . . . . .  | 102        |
| Polarization Ellipse Measurements . . . . .                                      | 103        |
| Spatial Gradient Measurements . . . . .  | 106        |
| Iowa Survey . . . . .  | 108        |
| Polarization Ellipse Measurements . . . . .                                      | 110        |
| Spatial Gradient Measurements . . . . .  | 114        |
| Terrain Conductivity Measurements . . . . .                                      | 121        |
| Nevada Survey . . . . .  | 123        |
| Polarization Ellipse Measurements . . . . .                                      | 123        |
| <b>CONCLUSIONS AND RECOMMENDATIONS . . . . .</b>                                 | <b>127</b> |
| Summary of Method Feasibility . . . . .  | 128        |
| Sensitivity Comparison of Polarization Ellipse and Spatial<br>Gradient . . . . . | 129        |
| Half-Space Models: Determination of $\rho$ or $K$ . . . . .                      | 130        |
| Two-Layer Models: Determination of $h$ . . . . .                                 | 130        |
| Two-Layer Models: Determination of $\rho_2$ . . . . .                            | 131        |
| Two-Layer Models: Determination of $K_2$ . . . . .                               | 131        |
| Three-Layer Models: Determination of $h_2$ . . . . .                             | 132        |
| Three-Layer Models: Determination of $\rho_2$ . . . . .                          | 132        |
| Three-Layer Models: Determination of $K_2$ . . . . .                             | 132        |
| Recommendations For Future Work . . . . .  | 132        |
| Instrument . . . . .   | 133        |
| Computer Inversion Program . . . . .   | 133        |
| <b>REFERENCES . . . . .</b>  | <b>136</b> |

## LIST OF FIGURES

|   |    |
|---|----|
| Figure 1. Geometry of source loop and layered-earth model. . . . .  | 11 |
| Figure 2. Behavior of the skin depth for varying dielectric permittivity. . . . .   | 27 |
| Figure 3. Parameters of the magnetic field polarization ellipse. . . . .  | 34 |
| Figure 4. Loop geometry for spatial gradient (SPATGRAD) measurement. . . . .  | 37 |
| Figure 5. Calculated polarization ellipse tilt angle and ellipticity for a half-space with a large $\rho$ and a variable K (Model 1). . . . .   | 41 |
| Figure 6. Calculated spatial gradient amplitude and phase for a half-space with a large $\rho$ and a variable K (Model 1). . . . .  | 43 |
| Figure 7. Calculated polarization ellipse tilt angle and ellipticity for a half-space with a small $\rho$ and a variable K (Model 2). . . . .   | 44 |
| Figure 8. Calculated spatial gradient amplitude and phase for a half-space with a small $\rho$ and a variable K (Model 2). . . . .  | 46 |
| Figure 9. Calculated polarization ellipse tilt angle and ellipticity for a half-space with K = 10 and a variable $\rho$ (Model 3). . . . .  | 47 |
| Figure 10. A graph comparing K of a half-space to the frequency where the first ellipticity peak occurs. The symbols represent different $\rho$ values. . . . .                                     | 49 |
| Figure 11. Calculated spatial gradient amplitude and phase for a half-space with K = 10 and a variable $\rho$ (Model 3). . . . .  | 50 |
| Figure 12. Calculated polarization ellipse tilt angle and ellipticity using $r=2$ m for a two-layer model with a relatively high- $\rho$ , low-K top layer of variable thickness (Model 4). . . . . | 52 |

Figure 13. Calculated polarization ellipse tilt angle and ellipticity using  $r=4$  m for a two-layer model with a relatively high- $\rho$ , low-K top layer of variable thickness (Model 4). . . . . 53

Figure 14. Calculated spatial gradient amplitude and phase for a two-layer model with a relatively high- $\rho$ , low-K top layer of variable thickness,  $h < r$  (Model 4). . . . . 55

Figure 15. Calculated spatial gradient amplitude and phase for a two-layer model with a relatively high- $\rho$ , low-K top layer of variable thickness,  $h$  exceeds  $r$  (Model 4). . . . . 56

Figure 16. Calculated polarization ellipse tilt angle and ellipticity for a two-layer model with a relatively low- $\rho$ , high-K top layer of variable thickness,  $r = 2$  m (Model 5). . . . . 58

Figure 17. Calculated polarization ellipse tilt angle and ellipticity for a two-layer model with a relatively low- $\rho$ , high-K top layer of variable thickness,  $r = 4$  m (Model 5). . . . . 59

Figure 18. Calculated spatial gradient amplitude and phase for a two-layer model with a relatively low- $\rho$ , high-K top layer of variable thickness,  $h < r$  (Model 5). . . . . 60

Figure 19. Calculated spatial gradient amplitude and phase for a two-layer model with a relatively low- $\rho$ , high-K top layer of variable thickness,  $h$  exceeds  $r$  (Model 5). . . . . 61

Figure 20. Calculated polarization ellipse tilt angle and ellipticity for a two-layer model with a relatively high- $\rho$ , low-K top layer and a variable  $\rho_2$ ,  $h=1$  m (Model 6). . . . . 63

Figure 21. Calculated spatial gradient amplitude and phase for a two-layer model with a relatively high- $\rho$ , low-K top layer and a variable  $\rho_2$ ,  $h=1$  m (Model 6). . . . . 64

Figure 22. Calculated polarization ellipse tilt angle and ellipticity for a two-layer model with a relatively high- $\rho$ , low-K top layer and a variable  $\rho_2$ ,  $h=2$  m (Model 6). . . . . 66

Figure 23. Calculated polarization ellipse tilt angle and ellipticity for a two-layer model with a relatively low- $\rho$ , high-K top layer and a variable  $\rho_2$ ,  $h=1$  m (Model 7). . . . . 67

Figure 24. Calculated spatial gradient amplitude and phase for a two-layer model with a relatively low- $\rho$ , high-K top layer and a variable  $\rho_2$ ,  $h=1$  m (Model 7). . . . . 69

Figure 25. Calculated spatial gradient amplitude and phase for a two-layer model with a relatively low- $\rho$ , high-K top layer and a variable  $\rho_2$ ,  $h=2$  m (Model 7). . . . . 70

Figure 26. Calculated polarization ellipse tilt angle and ellipticity for a two-layer model with a relatively high- $\rho$ , low-K top layer and a variable  $K_2$ ,  $h=1$  m (Model 8). . . . . 71

Figure 27. Calculated polarization ellipse tilt angle and ellipticity for a two-layer model with a relatively high- $\rho$ , low-K top layer and a variable  $K_2$ ,  $h=2$  m (Model 8). . . . . 72

Figure 28. Calculated spatial gradient amplitude and phase for a two-layer model with a relatively low- $\rho$ , high-K top layer and a variable  $K_2$ ,  $h=1$  m (Model 9). . . . . 73

Figure 29. Calculated spatial gradient amplitude and phase for a two-layer model with a relatively low- $\rho$ , high-K top layer and a variable  $K_2$ ,  $h=2$  m (Model 9). . . . . 74

Figure 30. Calculated polarization ellipse tilt angle and ellipticity anomalies caused by adding a thin resistive layer to a half-space to make a three-layer model. Displacement currents are neglected (Model 10). . . . . 77

Figure 31. Calculated polarization ellipse tilt angle and ellipticity anomalies caused by adding a thin resistive layer to a half-space to make a three-layer model. Displacement currents are included (Model 11). . . . . 79

Figure 32. A summary of the maximum anomalous response of the polarization ellipse tilt angle and ellipticity for Models 10 through 15. . . . . 80

Figure 33. Calculated spatial gradient amplitude and phase anomalies caused by adding a thin dielectric layer to a half-space to make a three-layer model (Model 15). . . . . 82

Figure 34. Calculated polarization ellipse tilt angle and ellipticity for a three-layer model with a variable  $\rho_2$  (Model 16). . . . . 84

Figure 35. Calculated spatial gradient amplitude and phase for a three-layer model with a variable  $\rho_2$  (Model 16). . . . . 85

Figure 36. Calculated polarization ellipse tilt angle and ellipticity for a three-layer model with a variable  $K_2$  (Model 17). . . . . 87

Figure 37. Calculated spatial gradient amplitude and phase for a three-layer model with a variable  $K_2$  (Model 17). . . . . 88

Figure 38. Block diagram of high-frequency sounder. . . . . 90

Figure 39. Illustration of the components of the total  $H_z$  field. . . . . 93

Figure 40. Sample printout of observed sounder data. . . . . 97

Figure 41. Behavior of exponent correction term for varying  $r$ -spacing of the farther loop set. . . . . 101

Figure 42. A three-layer inverse solution for polarization ellipse data recorded near Golden, Colorado, using two  $r$  spacings. The symbols are observed data, the solid lines are calculated data. . . . . 104

Figure 43. The three-layer model for the inverse solution shown in Figure 42. The numbers in parentheses are parameter resolution errors. . . . . 105

Figure 44. A three-layer inverse solution of SPATGRAD data recorded near Golden, Colorado. (a) Observed data (symbols) and calculated data (solid lines). (b) Inversion model. The numbers in parentheses are parameter resolution errors. . . . . 107

Figure 45. Location map and survey grid for polarization ellipse and SPATGRAD measurements recorded near Cedar Rapids, Iowa. . . . . 109

Figure 46. Two-layer inverse solution of polarization ellipse data recorded at

station 100NE on line 00 of the Iowa survey grid, using  $r = 1, 2,$  and 4 m. The symbols are observed data, and the solid lines are calculated data. . . . . 111

Figure 47. Two-layer inverse solution of polarization ellipse data recorded at station 360NE on line 00 of the Iowa survey grid, using  $r = 1, 2,$  and 4 m. The symbols are observed data, and the solid lines are calculated data. . . . . 112

Figure 48. Comparison of a shallow geologic cross-section from monitor well data, and a geoelectric cross-section from inversions of sounder data along line 00 of the Iowa survey grid. (a) Geologic section. (b) Geoelectric section. . . . . 113

Figure 49. Three-layer inverse solutions of SPATGRAD amplitude data recorded at station (a) 100NE and (b) 90NE on line 00 of the Iowa survey grid. The symbols are observed data, and the solid lines are calculated data. . . 115

Figure 50. Three-layer inverse solutions of SPATGRAD amplitude data recorded at station (a) 80NE and (b) 70NE on line 00 of the Iowa survey grid. The symbols are observed data, and the solid lines are calculated data. . . . . 116

Figure 51. Comparison of a shallow geologic cross-section from monitor well data, and a geoelectric cross-section from inversions of SPATGRAD data on line 00 of the Iowa survey grid. (a) Geologic section. (b) Geoelectric section. . . . . 118

Figure 52. Geoelectric sections from inversions of SPATGRAD data on (a) line 10NW and (b) line 10SE of the Iowa survey grid. . . . . 120

Figure 53. Comparison of (a) a geologic cross-section from monitor well data, and (b) a geoelectric cross-section from inversions of terrain conductivity data on line 00 of the Iowa survey grid. The geologic layers at depths < 4 m are combined into one. . . . . 122

Figure 54. A geoelectric cross-section from inversions of polarization ellipse data recorded at Henderson, Nevada, using  $r$  spacings of 2 and 4 m. . . . 124

Figure 55. Geoelectric resistivity sections from inversions of (a) borehole induction logs, and (b) terrain conductivity data recorded at Henderson, Nevada. Adapted from *Weber and Flatman* (1986). . . . . 126

**LIST OF TABLES**

Table 1: Typical resistivity and relative dielectric permittivity for some earth materials in the frequency range 1 to 100 MHz. . . . . 9

Table 2: Summary of forward model parameters. . . . . 39

## LIST OF SYMBOLS

|  |  |
|--|--|
| $d$                                    | Transmitter coil height above the earth (m)                    |
| $h, h_1, h_2, h_3$                     | Layer thickness (m or cm)                                      |
| $k$                                    | Complex wave number  |
| kHz                                    | Frequency in kilohertz ( $10^3$ Hz)                            |
| $m$                                    | Primary field decay exponent                                   |
| MHz                                    | Frequency in Megahertz ( $10^6$ Hz)                            |
| $r$                                    | Coil separation (m)  |
| $z$                                    | Receiver coil height above the earth                           |
| $\alpha$                               | Polarization ellipse tilt angle                                |
| $\delta$                               | Skin depth (m) or electric charge density                      |
| $\varepsilon$                          | Polarization ellipse ellipticity                               |
| $\epsilon$                             | Dielectric permittivity (F/m)                                  |
| $\epsilon_0$                           | Free-space dielectric permittivity, $8.854 \cdot 10^{-12}$ F/m |
| K                                      | Relative dielectric permittivity ( $\epsilon/\epsilon_0$ )     |
| $\mu$                                  | Magnetic permeability (H/m)                                    |
| $\mu_0$                                | Free-space magnetic permeability, $4\pi \cdot 10^{-7}$ H/m     |
| $\xi$                                  | Decay exponent correction factor                               |
| $\rho, \rho_1, \rho_2, \rho_3$         | Layer resistivity ( $\Omega \cdot m$ )                         |
| $\sigma, \sigma_1, \sigma_2, \sigma_3$ | Layer conductivity (S/m)                                       |
| $\omega$                               | Angular frequency  |
| *                                      | Variable or unresolvable parameter                             |

## ACKNOWLEDGMENTS

I would like to thank the U.S. Geologic Survey for providing employment and facilities for the high-frequency sounder development. In particular, I would like to thank Walt Anderson for his computer programming expertise and patience with requests to provide "just one more type of field quantity" in the programs; Tom Grover for his electrical engineering expertise, field assistance, and patience with requests for "just one more instrument modification"; and Vic Labson for his supervision, advice, and patience with requests for "just one more extension of the student appointment".

I would also like to thank the members of my committee at Colorado School of Mines: Alex Kaufman, Ron Knoshaug, Dick Hutchinson, and John Hogan, as well as my advisor Cathy Skokan for her support and patience with requests for "just one more semester".

Finally, I must thank Robin, who used her leverage both as my wife and as my martial arts sensei to gently prod me towards the completion of this project.

## INTRODUCTION

Electromagnetic (EM) sounding and profiling are widely used for mapping the shallow subsurface, and for monitoring processes within it. Knowledge of shallow subsurface properties is important to agriculture, ground water, waste disposal, archaeology, and soil engineering; this knowledge is also important for interpretation of deep EM soundings. The upper few meters containing the soil zone, capillary fringe, and water table are often of primary interest. Surface geoelectrical methods are used to characterize soil and rock types because electrical properties of the earth are often sensitive to clay and fluid content, soil and rock type, grain size, texture and weathering, and presence of pollutants. Geoelectrical methods are used for horizontal profiling to map lateral variations in electrical properties, and for vertical sounding to map variations with depth.

This study describes a new high-frequency EM instrument designed for shallow mapping, and new computer programs for modeling and interpretation of high-frequency EM measurements. The electromagnetic field equations used in the computer programs are developed in detail. Forward models are used to demonstrate the influence of dielectric properties on layered-earth measurements, and to evaluate the effectiveness of high-frequency sounding for achieving some typical goals in shallow mapping applications. The instrument design considerations and operational procedures are

discussed, and the inversion program is used to interpret field data collected at three survey sites with the prototype EM system; where possible, the results are compared with surveys using other geophysical methods. Finally, the limitations of the prototype instrument and inversion schemes are discussed, and a number of improvements are suggested.

### Limitations of Existing EM Methods

Several EM tools widely used for shallow mapping are in-situ probes, ground-penetrating radar, time-domain EM, and frequency-domain terrain conductivity. Each has limitations, either site-specific or inherent in the instrument design. Reviews of several current instruments can be found in *Epp et al.* (1988) and *Nabighian* (1991).

### In-Situ Probes

A variety of devices can be placed directly in the earth for in-situ measurement of electrical properties to a depth of 1 or 2 m. Most of these probes are based on the behavior of transmission lines (*Hayes*, 1982; *Topp et al.*, 1982), plate capacitors (*Wobschall*, 1978), or waveguides (*Birchak et al.*, 1974). In-situ measurements are by nature an invasive method, requiring excavation or drilling for insertion of the probe; this is costly and also highly undesirable when surveying a hazardous waste site. The measurements are affected by air gaps between the probe and the soil, by soil texture, and by physical disturbance of the soil during insertion.

### Ground-Penetrating Radar

Ground-penetrating radar (GPR) is very useful for sounding and profiling in resistive environments. The method has excellent vertical and lateral resolution, and a depth range from a few centimeters to tens of meters (*Ulriksen, 1982; Davis and Annan, 1989; Beres and Haeni, 1991*). However, the depth range for a GPR instrument is limited in a low-resistivity material. The presence of conductive pore fluids, or a few weight percent of clay, may reduce the depth range to less than 1 m (*Olhoeft, 1986*).

### Time-Domain EM

Transient EM soundings observed on the earth's surface are limited by a minimum depth of investigation, above which only the integrated conductance of the overlying section can be resolved. The minimum depth is determined by earth resistivity, duration of the transmitter turn-off ramp, and the earliest sample time of the instrument; low resistivity, short turn-off ramp, and early first-sample times yield a shallower minimum depth of investigation. The lowest resistivity for most materials found near the surface is in the range of 1 to 100  $\Omega\cdot\text{m}$ , and many instruments have a first-sample time of 50  $\mu\text{s}$ ; in this case, the minimum depth of investigation is about 10 to 100 m (*Spies, 1989*). Instruments designed specifically for shallow sounding have a turn-off ramp time of about 1  $\mu\text{s}$ , and a first-sample time of 6  $\mu\text{s}$ ; in this case, a minimum depth of about 5 m is possible in low-resistivity materials (*Hoekstra and Blohm, 1990*). *McNeill (1993)* notes that a minimum depth of about 3 m is possible

using a physically small transmitter loop and a closely-spaced receiver coil. Thus, even under good conditions, existing transient EM instruments cannot be used for detailed investigation of the first 3 to 5 m of the earth.

### Terrain Conductivity

Terrain conductivity instruments operate at low induction numbers (LIN) by using low frequencies and relatively short coil spacings (*McNeill, 1980; Frischknecht et al., 1991*). They are very effective for mapping lateral variations in conductivity, and are used successfully for many types of groundwater and pollution studies (*Greenhouse and Slaine, 1983; Weber et al., 1984; McNeill, 1990*). However, as sounding tools, terrain conductivity instruments are effective only for a restricted class of EM problems. EM soundings can be made by varying the frequency, or by varying the configuration and spacing of the transmitter and receiver. Existing terrain conductivity instruments use fixed frequencies, so that soundings are made using a limited selection of spacings and coil configurations. The resulting number of data points (usually 6 or 8) is sufficient only for rudimentary interpretation of vertical conductivity variations.

### High Frequency Sounding

Frequency-domain EM soundings can obtain much more information when frequency is varied along with coil spacing and configuration. Wide-band instruments used for relatively deep sounding typically utilize 1 to 3 decades within the frequency

range 0.05 Hz to 60 kHz. However, a suitable frequency range for shallow sounding is much higher, e.g., 100 kHz to 50 MHz. Thus, one requirement for effective shallow sounding is a wide-band, high-frequency instrument.

At low frequencies and for most earth materials, dielectric effects are negligible compared to electrical resistivity, and most computer programs for EM modeling and interpretation do not include dielectric permittivity. However, at high frequencies or in very resistive terrain, displacement currents in the earth are important. Therefore, a second requirement for effective shallow sounding is forward and inverse computer programs which include displacement currents as well as conduction currents.

The introduction of an additional parameter such as dielectric permittivity complicates interpretation of EM data. The reward, however, is the additional information obtained about the properties of the subsurface. This information is especially valuable for hazardous waste applications, because certain pollutants may have a negligible effect on observed values of resistivity, but a large effect on observed dielectric permittivity (*Olhoeft, 1986*). For applications where determination of soil moisture content is desired, dielectric permittivity information can be a more reliable measure than resistivity information, because resistivity is affected by variations in the chemical properties of soils, while dielectric permittivity is more affected by bulk water content (*Selig and Mansukhani, 1975; Schmugge et al., 1980*).

### Previous Studies

The influence of displacement currents is routinely considered for methods such as high-frequency borehole EM (e.g., *Poley et al.*, 1978; *Kuth and Neubauer*, 1988), and radar (e.g., *Davis and Annan*, 1989; *Beres and Haeni*, 1991). However, there are very few similar studies for other EM methods. *Katsube* (1974, 1975) investigates the accuracy of standard skin depth calculations at high frequencies, and presents a modified empirical skin depth formula. *Sinha* (1977a) and *Lytle et al.* (1976) investigate the effect of displacement currents on airborne wavelilt measurements. *Sinha* shows a graphical means for obtaining resistivity and dielectric permittivity; *Lytle et al.* develop a means for solving equivalence problems by using oscillatory behavior of the wavelilt at high frequencies to resolve layer thickness. *Bitterlich and Kellner* (1970) show a method for determining the resistivity and dielectric permittivity of a homogeneous earth from underground measurements. *Fraser et al.* (1990) analyze the distortion of airborne slingram measurements and the interpretation errors which result from neglect of displacement currents. They conclude that effective error reduction is possible only if displacement currents are directly included in EM calculations. A common conclusion from these papers, either stated or apparent in the data, is that displacement currents become significant when their magnitude exceeds about 5 percent of conduction currents; this occurs at frequencies around 50 kHz to 100 kHz for many earth materials.

A few authors specifically develop general field equations for loop-loop EM systems. *Wait* (1954) develops a closed-form solution for horizontal loops on the surface

of a half-space; in a later paper, *Fuller and Wait* (1972), present an approximate solution for a vertical magnetic dipole over layers with electrical properties that vary exponentially with depth. *Wait* (1982) develops equations for the vertical magnetic dipole above a multi-layer earth; *Ward and Hohmann* (1987) develop similar equations for a loop with finite dimensions. *Morrison et al.* (1969) develop equations which they use to compute the time-domain fields of a horizontal loop on or above a layered earth; *Ryu et al.* (1970) extend this work to field computations in the frequency domain. *Ward and Dey* (1971) study a vertical-loop source mounted on a lunar rover for soundings on the moon. *Sinha* (1977b) considers permafrost studies, and presents dipole equations for five widely-used loop configurations.

### Electrical Properties of Earth Materials

The electrical properties of materials are usually characterized by three parameters: electrical conductivity ( $\sigma$ ), dielectric permittivity ( $\epsilon$ ), and magnetic permeability ( $\mu$ ). Electrical resistivity ( $\rho$ ) is often used in place of conductivity, where  $\rho = 1/\sigma$ . In the absence of magnetic minerals such as magnetite, the magnetic permeability of earth materials is effectively equal to the free space value,  $\mu_0 = 4\pi \cdot 10^{-7}$  H/m. The resistivity of shallow earth materials varies over a large range, typically from  $1 \Omega \cdot \text{m}$  to  $10^4 \Omega \cdot \text{m}$ , with some values possibly as large as  $10^7$  or  $10^9 \Omega \cdot \text{m}$  for very dry materials. The dielectric permittivity is usually expressed as a relative value  $K$ , normalized by the permittivity of free space:  $K = \epsilon/\epsilon_0$ , where  $\epsilon_0 = 8.854 \cdot 10^{-12}$  F/m. The

high-frequency relative permittivity of most earth materials varies between 1, the value for air, and 81, the value for fresh water. Table 1 lists typical  $\rho$  and K values for some earth materials commonly encountered in shallow investigations.

#### Neglect of Frequency Dependence

The electrical parameters of all earth materials show some degree of frequency dependence, and may have both real and imaginary parts. In particular, K for many materials has a value at high frequencies (e.g., 100 MHz) that may be several orders of magnitude smaller than the static (frequency = 0) value. The frequency dependence and complex nature of K and  $\rho$  can be described by power-law or Cole-Cole models (*Keller, 1987; Knight and Nur, 1987; Taherian et al., 1990*). Although frequency-dependent effects may be significant over the frequency range of 100 kHz to 50 MHz, this study considers only the simple case where K and  $\rho$  are assumed real and constant at all frequencies. This assumption is perhaps unrealistic; however, given the present "untouched" state of this high-frequency sounding method, it is desirable to examine a simplified model before considering the complications of a frequency-dependent model.

Table 1: Typical resistivity and relative dielectric permittivity for some earth materials in the frequency range 1 to 100 MHz. Data are from *Epp et al. (1988)*, *Davis and Annan (1989)*, and *Ulriksen (1982)*. Pore fluid is fresh water.

| Material          | $\rho$ ( $\Omega \cdot m$ ) | K       |
|-------------------|-----------------------------|---------|
| Sand (dry)        | $10^3 - 10^7$               | 3 - 6   |
| Sand (saturated)  | $10^2 - 10^4$               | 20 - 30 |
| Silts             | $10^2 - 10^3$               | 5 - 30  |
| Shales            | $10 - 10^3$                 | 5 - 15  |
| Clays (saturated) | 1 - 10                      | 5 - 40  |
| Humid soil        | 50 - 100                    | 30      |
| Cultivated soil   | 200                         | 15      |
| Rocky soil        | 1000                        | 7       |
| Dry sandy soil    | 7100                        | 3       |
| Wet sandy soil    | 150                         | 25      |
| Dry loamy soil    | 9100                        | 3       |
| Wet loamy soil    | 50                          | 19      |
| Dry clayey soil   | 3700                        | 2       |
| Wet clayey soil   | 20                          | 15      |
| Sandstone (wet)   | 25                          | 6       |
| Limestone (dry)   | $10^9$                      | 7       |
| Limestone (wet)   | 40                          | 4 - 8   |
| Basalt (wet)      | 100                         | 8       |
| Granite           | $10^3 - 10^5$               | 4 - 6   |
| Fresh Water       | $30 - 10^4$                 | 81      |
| Permafrost        | $10^2 - 10^5$               | 4 - 8   |
| Dry snow          | $10^5 - 10^6$               | 1       |
| Ice               | $10^3 - 10^5$               | 3 - 4   |
| Air               | $\approx$ infinite          | 1       |

## THEORY

The problem under consideration is the calculation of the electromagnetic response of a layered earth where electrical properties vary in the vertical direction. Solutions of Maxwell's equations are well-documented for the case where displacement currents are neglected (the quasi-static assumption) and loop dimensions are assumed very small with respect to loop separation (the dipole approximation); e.g., *Kaufman and Keller* (1983) provide an excellent detailed description of the EM boundary-value problem and the methods for its solution. However, for the high frequencies and relatively small separations used by the proposed sounding method, the solution of the boundary-value problem must account for displacement currents and finite loop dimensions.

The geometry of the desired model is shown in Figure 1. A horizontal source loop is located at the origin of a cylindrical coordinate system with the positive  $z$  axis directed downwards. The loop has a radius  $a$  and carries a current  $I$  which oscillates as  $e^{i\omega t}$ . The earth consists of homogeneous, isotropic horizontal layers with the top of the first layer at a distance  $d$  below the loop. Each layer is characterized by its thickness  $h$  (m), electrical conductivity  $\sigma$  (S/m), magnetic permeability  $\mu$  (H/m), and dielectric permittivity  $\epsilon$  (F/m). The electrical parameters in the air are those of free space:  $\sigma_0=0$  S/m,  $\mu_0=4\pi \cdot 10^{-7}$  H/m, and  $\epsilon_0=8.854 \cdot 10^{-12}$  F/m. The magnetic permeability of all layers is assumed equal to the free-space value.

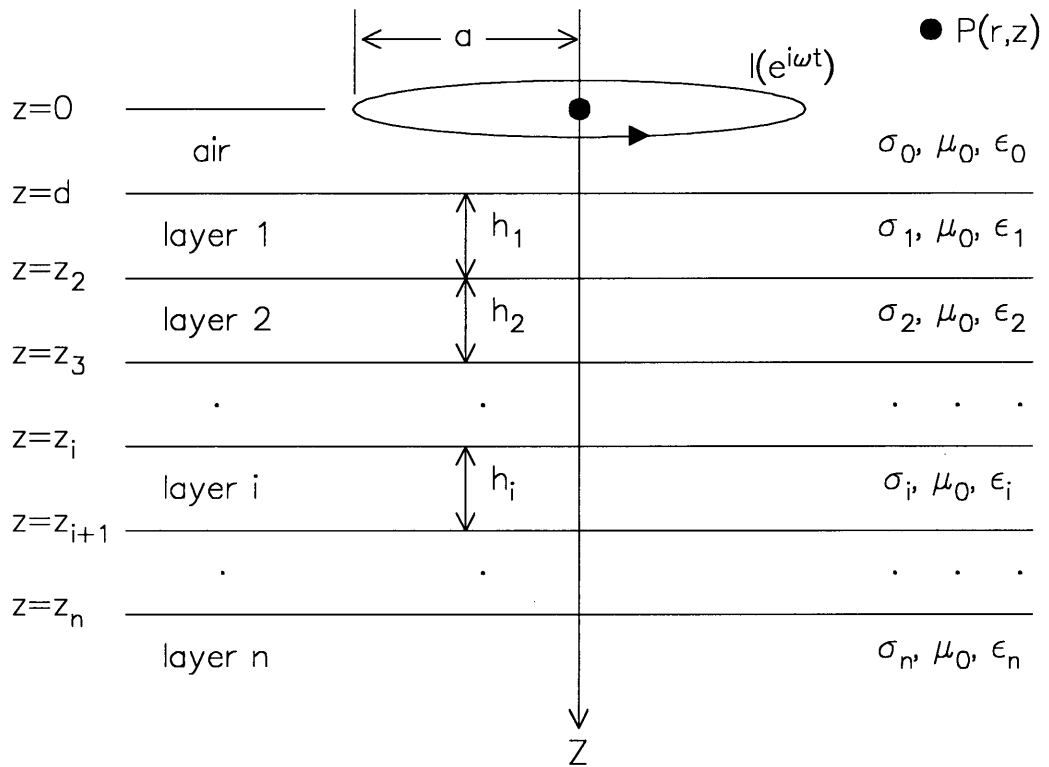


Figure 1. Geometry of source loop and layered-earth model.

The goal is to calculate the electromagnetic fields at an observation point  $P(r,z)$ .

The fields are solutions of Maxwell's equations:

$$\nabla \times \mathbf{E} = -\mu \frac{\partial \mathbf{H}}{\partial t}, \quad \nabla \cdot \epsilon \mathbf{E} = \delta,$$

$$\nabla \times \mathbf{H} = \sigma \mathbf{E} + \epsilon \frac{\partial \mathbf{E}}{\partial t}, \quad \nabla \cdot \mathbf{H} = 0.$$

where  $\mathbf{E}$  and  $\mathbf{H}$  are the electric and magnetic fields, and  $\delta$  is electric charge density. The fields oscillate as  $e^{i\omega t}$ , with the same frequency as the source current. For the given model geometry, the source current and hence the electric field have only a single component in the  $\theta$  direction, forming horizontal circles centered on the  $z$  axis. The magnetic field has components in the  $r$  and  $z$  directions. Since the electric field lines do not intersect boundaries between layers, no electric charges will appear ( $\delta=0$ ). With these conditions, Maxwell's equations can be written as (*Kaufman and Keller, 1983*):

$$\nabla \times \mathbf{E} = -i\mu\omega\mathbf{H}, \quad (1)$$

$$\nabla \times \mathbf{H} = (\sigma + i\omega\epsilon)\mathbf{E}, \quad (2)$$

$$\nabla \cdot \mathbf{E} = 0, \quad (3)$$

$$\nabla \cdot \mathbf{H} = 0. \quad (4)$$

To separate the equations into partial differential equations of a single variable, a potential function is introduced from which the fields can be derived. A magnetic-type vector potential (*Ward and Hohmann, 1987*):

$$\mathbf{E} = -i\mu\omega\nabla\times\mathbf{F} , \quad (5)$$

automatically satisfies equation [3] since the divergence of curl is always zero. Given the geometry of the  $\mathbf{E}$  field,  $\mathbf{F}$  needs only a single component in the  $z$  direction. Substituting equation [5] into equation [2]:

$$\nabla\times\mathbf{H} = (-i\sigma\mu\omega + \omega^2\mu\epsilon)\nabla\times\mathbf{F} .$$

This relation means that  $\mathbf{H}$  and  $\mathbf{F}$  can differ only by some gradient:

$$\mathbf{H} = (-i\sigma\mu\omega + \omega^2\mu\epsilon)\mathbf{F} - \nabla U , \quad (6)$$

where  $U$  is an arbitrary scalar potential. Substituting equation [6] into equation [1]:

$$-i\mu\omega\nabla\times(\nabla\times\mathbf{F}) = -i\mu\omega(-i\sigma\mu\omega + \omega^2\mu\epsilon)\mathbf{F} + \nabla U .$$

Or, simplifying:

$$\nabla^2\mathbf{F} - \nabla(\nabla\cdot\mathbf{F}) = -(-i\sigma\mu\omega + \omega^2\mu\epsilon)\mathbf{F} + \nabla U . \quad (7)$$

Up to this point, the relation of  $\mathbf{F}$  to the  $\mathbf{E}$  and  $\mathbf{H}$  fields is defined only through the curl operator. To completely determine the relation, the divergence of  $\mathbf{F}$  must also

be defined. Since the scalar potential  $U$  is completely arbitrary, a "gauge condition" can be used to select a relation between  $U$  and  $F$  which specifies the divergence for a given class of fields. For fields caused by electric current, the appropriate condition is the "Lorentz gauge" (*Javid and Brown, 1963*):

$$U = -\nabla \cdot F . \quad (8)$$

This yields the equation for  $F$  in source-free regions:

$$\nabla^2 F + k^2 F = 0 , \quad (9)$$

where  $k = (-i\sigma\mu\omega + \omega^2\mu\epsilon)^{1/2}$ . Equation [9] is commonly referred to as the homogeneous Helmholtz equation. In the region containing the source loop (i.e., the air above the surface), the right side of equation [9] is replaced with the source current to obtain the inhomogeneous Helmholtz equation:

$$\nabla^2 F + k^2 F = j_s . \quad (10)$$

Using equations [5], [6], and [8], the electromagnetic fields are written in terms of  $F$ :

$$E = -i\omega\mu\nabla \times F ,$$

$$H = k^2 F - \nabla(\nabla \cdot F) .$$

In cylindrical coordinates, the individual field components are:

$$E_{\theta} = i\mu\omega \frac{\partial F}{\partial r}, \quad (11)$$

$$H_r = \frac{\partial^2 F}{\partial r \partial z}, \quad H_z = k^2 F + \frac{\partial^2 F}{\partial z^2}. \quad (12)$$

### Solving For The Vector Potential

The vector potential  $F$  has two parts representing the contribution of the primary (source) field in air and the contribution from secondary currents induced in the earth layers:

$$F = F_p + F_s, \quad (13)$$

where  $F_p$  is the primary potential and  $F_s$  is the secondary potential.

### The Primary Field Potential

The primary potential  $F_p$  is the particular solution of equation [10]. If the source loop is considered as a wire filament having infinitesimal cross-sectional area, the source current can be expressed using Dirac delta functions:

$$\nabla^2 F_p + k^2 F_p = I \delta(r-a) \delta(z) . \quad (14)$$

The solution of the inhomogeneous Helmholtz equation has the form of a Green's function (*Ward and Hohmann, 1987*):

$$F_p = A \frac{e^{-ik_0 R}}{R} = \int_0^\infty A(\lambda) \frac{\lambda}{u_0} J_0(\lambda r) e^{\pm u_0 z} d\lambda , \quad (15)$$

where

$$u_0 = (\lambda^2 - k_0^2)^{1/2} , \quad R = (r^2 + z^2)^{1/2} , \quad k_0 = (-i\sigma_0 \mu_0 \omega + \omega^2 \mu_0 \epsilon_0)^{1/2} ,$$

and  $J_0(\lambda r)$  is the zero-order Bessel function of the first kind. The sign of the exponent is chosen based on the sign of  $z$ , to force decay of the exponent as  $z$  increases. The coefficient  $A(\lambda)$  is evaluated by applying boundary conditions to the magnetic field in the plane of the source loop ( $z=0$ ). The first condition is continuity of the normal component, written in the form:

$$\lim_{z \rightarrow 0} [H_z(z^+) - H_z(z^-)] = 0 . \quad (16)$$

The notation  $z^+$ ,  $z^-$ , denotes approaching the  $z=0$  plane from the positive and negative side respectively. The second condition is the behavior of the tangential component. The source current can be treated as a surface current which exists only along the circle

with radius  $a$ . For this case, instead of being continuous across the plane of the loop, the tangential component has a discontinuity equal to the surface current (*Wait*, 1982):

$$\lim_{z \rightarrow 0} [H_r(z^+) - H_r(z^-)] = j_s . \quad (17)$$

The  $H_z$  and  $H_r$  components are obtained from equation [12] and the right side of equation [15]. By differentiating while using the proper sign on the exponent, and then setting  $z=0$ , condition [16] shows that  $A(\lambda)$  is equal in magnitude and sign on either side of the  $z=0$  plane:

$$A^+(\lambda) = A^-(\lambda) .$$

Knowing this, condition [17] becomes:

$$2 \int_0^{\infty} A(\lambda) \lambda^2 J_1(\lambda r) d\lambda = j_s . \quad (18)$$

The final step in evaluating  $A(\lambda)$  is to express the source current  $j_s$  in spectral form. First, define an appropriate Hankel transform pair (*Wait*, 1982):

$$j_s(r) = \int_0^{\infty} S(\lambda) \lambda J_1(\lambda r) d\lambda , \quad (19)$$

$$S(\lambda) = \int_0^{\infty} j_s(r) r J_1(\lambda r) dr . \quad (20)$$

Now, insert the Dirac delta expression for  $j_s$  (right side of equation [14]) into equation [20]. The delta functions reduce equation [20] to:

$$S(\lambda) = I a J_1(\lambda a) ,$$

so that equation [19] can be written as:

$$j_s = \int_0^{\infty} [I a J_1(\lambda a)] \lambda J_1(\lambda r) d\lambda .$$

This is the desired spectral representation of the source current. Boundary condition [18] now becomes:

$$2 \int_0^{\infty} A(\lambda) \lambda^2 J_1(\lambda r) d\lambda = \int_0^{\infty} [I a J_1(\lambda a)] \lambda J_1(\lambda r) d\lambda .$$

Since the integrands are spectral representations of functions, equality of the integrals means equality of the integrands (i.e., if 2 functions are equal, then the spectra of their

transforms are also equal). Therefore, the integral signs can be dropped, and the coefficient  $A(\lambda)$  is:

$$A(\lambda) = \frac{Ia J_1(\lambda a)}{2\lambda} . \quad (21)$$

Inserting equation [21] into the right side of equation [15] yields the desired primary potential:

$$F_p = \frac{Ia}{2} \int_0^{\infty} J_1(\lambda a) J_0(\lambda r) \frac{e^{-u_0|z|}}{u_0} d\lambda . \quad (22)$$

### The Secondary Field Potential

The complementary solution of equation [9] (the homogeneous Helmholtz equation) is obtained by separation of variables (*Kaufman and Keller, 1983*). For cylindrical coordinates and axial symmetry, the solution is a product of exponential functions of the  $z$  coordinate and Bessel functions of the  $r$  coordinate:

$$F_s = \int_0^{\infty} [B(\lambda)e^{-uz} + C(\lambda)e^{+uz}] [J_0(\lambda r) + Y_0(\lambda r)] d\lambda . \quad (23)$$

The Bessel function of the second kind,  $Y_0(\lambda r)$ , is discarded since it is infinite when  $r = 0$ . The unknown coefficients are evaluated by first forming the expression for the total vector potential, and then applying boundary conditions.

### The Total Vector Potential

In any given layer, the vector potential for the total field is the sum of the primary and secondary potentials (equation [13]). In the air layer defined by  $z \leq d$  the total potential is:

$$F_0 = F_p + \int_0^{\infty} C_0(\lambda) e^{u_0 z} J_0(\lambda r) d\lambda \quad (z \leq d) .$$

The subscript on  $F_0$ ,  $C_0$ , and  $u_0$  is the layer index number. The term from equation [23] which contains a negative exponent is discarded since it becomes infinite as  $z$  approaches negative infinity. Using equation [22], the total potential becomes:

$$F_0 = \frac{Ia}{2} \int_0^{\infty} \left( J_1(\lambda a) \frac{e^{-u_0 z}}{u_0} + C_0(\lambda) e^{u_0 z} \right) J_0(\lambda r) d\lambda \quad (z \leq d) . \quad (24)$$

In layers with finite thickness, the layer boundaries are defined by  $z = z_i$  and  $z = z_{i+1}$ , and the total potential is:

$$F_i = \frac{Ia}{2} \int_0^{\infty} (B_i(\lambda)e^{-u_i z} + C_i(\lambda)e^{u_i z}) J_0(\lambda r) d\lambda \quad (z_i \leq z \leq z_{i+1}), \quad (25)$$

where

$$u_i = (\lambda^2 - k_i^2)^{1/2}, \quad k_i = (-i\sigma_i \mu_i \omega + \omega^2 \mu_i \epsilon_i)^{1/2}.$$

Here, both positive and negative exponents are allowed, since  $z$  is bounded and finite. In the bottom layer, defined by  $z \geq z_n$ , the positive exponent is discarded since  $z$  extends to positive infinity:

$$F_n = \frac{Ia}{2} \int_0^{\infty} B_n(\lambda) e^{-u_n z} J_0(\lambda r) d\lambda \quad (z \geq z_n). \quad (26)$$

### Boundary Conditions and the Electromagnetic Field Equations

The unknown coefficients  $B(\lambda)$  and  $C(\lambda)$  are evaluated by applying boundary conditions at the interfaces between layers. The continuity conditions on  $E_\theta$  and  $H_r$  are sufficient for this case. Using the relations from equation [12], the continuity conditions at any interface defined by  $z=z_i$  are:

$$\frac{\partial F_{i-1}}{\partial r} = \frac{\partial F_i}{\partial r}, \quad \frac{\partial^2 F_{i-1}}{\partial r \partial z} = \frac{\partial^2 F_i}{\partial r \partial z} \quad (z = z_i) .$$

Since these conditions must hold for all values of  $r$ , the  $r$ -dependence can be removed by integration:

$$F_{i-1} = F_i, \quad \frac{\partial F_{i-1}}{\partial z} = \frac{\partial F_i}{\partial z} \quad (z = z_i) . \quad (27)$$

For any number of layers, applying the conditions of equation [27] at each interface provides a system of simultaneous equations sufficient to solve for all unknown coefficients. As an example, consider the simple case of a homogenous half-space. Applying the conditions to equations [24] and [26] at the earth's surface ( $z=d$ ):

$$\left( J_1(\lambda a) \frac{e^{-u_0 d}}{u_0} + C_0(\lambda) e^{u_0 d} \right) = B_1(\lambda) e^{-u_1 d} ,$$

$$\left( -u_0 J_1(\lambda a) e^{-u_0 d} + u_0 C_0(\lambda) e^{u_0 d} \right) = -u_1 B_1(\lambda) e^{-u_1 d} .$$

The integral signs are dropped because, as in equation [21], equality of integrals means equality of integrands. Since measurements are taken only above the earth's surface (not underground), it is necessary only to solve for  $C_0(\lambda)$ :

$$C_0(\lambda) = \left( \frac{u_0 - u_1}{u_0 + u_1} \right) \frac{J_1(\lambda a) e^{-2u_0 d}}{u_0} .$$

The complete potential function for the fields above a half-space is then:

$$F_0 = \frac{Ia}{2} \int_0^{\infty} \frac{1}{u_0} \left[ e^{-u_0 z} + \left( \frac{u_0 - u_1}{u_0 + u_1} \right) e^{u_0(z-2d)} \right] J_1(\lambda a) J_0(\lambda r) d\lambda . \quad (28)$$

The term in large parentheses is a reflection coefficient for fields with a horizontal  $E$  field (*Ward and Hohmann, 1987*). The potential for fields above a multiple-layer earth model is obtained by using a general reflection coefficient in equation [28]:

$$F_0 = \frac{Ia}{2} \int_0^{\infty} \frac{1}{u_0} \left[ e^{-u_0 z} + R_{TE} e^{u_0(z-2d)} \right] J_1(\lambda a) J_0(\lambda r) d\lambda , \quad (29)$$

where

$$R_{TE} = \left( \frac{Y_0 - \hat{Y}_1}{Y_0 + \hat{Y}_1} \right) . \quad (30)$$

The coefficient  $R_{TE}$  is a recursive function of layer admittance evaluated by starting at the bottom ( $n$ th) layer and iterating upwards to the surface:

$$Y_0 = \frac{u_0}{i\omega\mu_0}, \quad Y_i = \frac{u_i}{i\omega\mu_i},$$

$$\hat{Y}_1 = Y_1 \frac{\hat{Y}_2 + Y_1 \tanh(u_1 h_1)}{Y_1 + \hat{Y}_2 \tanh(u_1 h_1)}, \dots, \hat{Y}_i = Y_i \frac{\hat{Y}_{i+1} + Y_i \tanh(u_i h_i)}{Y_i + \hat{Y}_{i+1} \tanh(u_i h_i)}, \dots, \hat{Y}_n = Y_n.$$

Finally, the electromagnetic fields above the earth are obtained from equation [29] and equation [12]:

$$E_\theta = \frac{-i\mu\omega Ia}{2} \int_0^\infty \frac{\lambda}{u_0} [e^{-u_0 z} + R_{TE} e^{u_0(z-2d)}] J_1(\lambda a) J_1(\lambda r) d\lambda, \quad (31)$$

$$H_\rho = \frac{Ia}{2} \int_0^\infty \lambda [e^{-u_0 z} + R_{TE} e^{u_0(z-2d)}] J_1(\lambda a) J_1(\lambda r) d\lambda, \quad (32)$$

$$H_z = \frac{Ia}{2} \int_0^\infty \frac{\lambda^2}{u_0} [e^{-u_0 z} + R_{TE} e^{u_0(z-2d)}] J_1(\lambda a) J_0(\lambda r) d\lambda. \quad (33)$$

### Skin Depth

A significant difference between the general form of the field equations and the quasi-static form is the manner in which the electromagnetic fields decay inside the earth. The fields decay with depth as an exponential,  $e^{-\beta z}$ , where  $\beta$  is an attenuation factor with units of inverse meters (*Ward and Hohmann, 1987*):

$$\beta = \left\{ \frac{\omega^2 \mu \epsilon}{2} \left[ \left( 1 + \frac{\sigma^2}{\epsilon^2 \omega^2} \right)^{1/2} - 1 \right] \right\}^{1/2} . \quad (34)$$

The "skin depth",  $\delta$ , is defined as the depth at which a field's amplitude is reduced by a factor of  $1/e$ :

$$\delta = \frac{1}{\beta} . \quad (35)$$

The contribution of conduction currents in equation [34] is characterized by  $\sigma$ , and the contribution of displacement currents is characterized by  $\epsilon\omega$ . When displacement currents are negligible, equation [34] is readily simplified and the skin depth reduces to the quasi-static approximation:

$$\delta = \left( \frac{2}{\sigma \mu \omega} \right)^{1/2} \quad (\sigma \gg \epsilon \omega) . \quad (36)$$

Conversely, when conduction currents are negligible, equation [34] can be simplified by using a truncated binomial series:

$$(1 + x)^{1/2} \approx 1 + \frac{x}{2} \quad (|x| \ll 1) ,$$

to obtain a high-frequency asymptote for  $\delta$ :

$$\delta = \frac{2}{\sigma} \left( \frac{\epsilon}{\mu} \right)^{1/2} \quad (\omega \epsilon \gg \sigma) . \quad (37)$$

In the quasi-static approximation (equation [36]), the skin depth decreases continuously as  $\omega$  increases, while the high-frequency skin depth (equation [37]) is a constant which depends only on the electrical parameters of the earth. In the general field equations, the behavior of the skin depth is thus characterized by three regions:

- 1) A low-frequency region where displacement currents are negligible and the skin depth is an inverse function of conductivity and frequency, described by equation [36].
- 2) A transition region where both displacement currents and conduction currents are significant, and the skin depth is a function of conductivity, dielectric permittivity, and frequency, described by equations [34] and [35].
- 3) A high-frequency region where displacement currents dominate, and the skin depth is a function only of conductivity and dielectric permittivity, described by equation [37].

The three regions of behavior are illustrated by Figure 2, which shows skin depths calculated using equation [34], for two conductivities and a range of relative dielectric permittivities. At the low frequencies the skin depth curves steadily decrease with increasing frequency; over the middle frequencies they flatten, and the skin depth

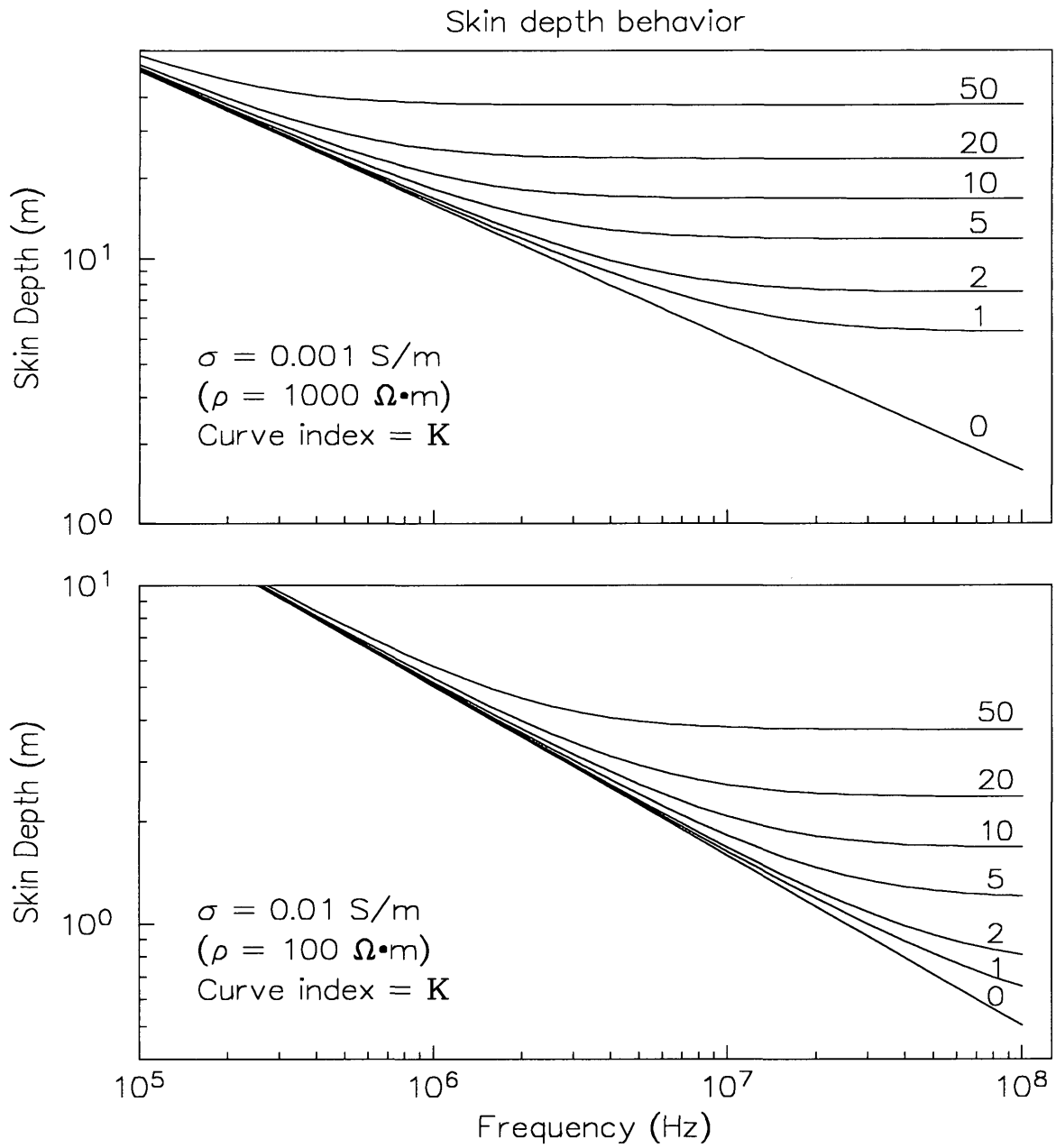


Figure 2. Behavior of the skin depth for varying dielectric permittivity.

becomes constant at high frequencies. Increasing the value of  $\sigma$ , or decreasing the value of  $K$ , shifts the transition region to higher frequencies. The curve for  $K=0$  exhibits quasi-static behavior for all frequencies.

### Computer Modeling Programs

The EM field calculations in this paper are based on a modification of equations [31], [32], and [33], which makes them suitable for numerical integration by a computer. The modified forms are valid for all frequencies and electrical parameter ranges, provided that the loop radius  $a$  is much smaller than the free-space wavelength.

### Modification of the Field Equations

*Ryu et. al* (1970) develop a numerically tractable form of the field equations for the special case where the receiver loop is on the earth's surface. Setting  $z=d$ , the exponential terms in the square brackets of equations [31], [32], and [33] become:

$$e^{-u_0 d}(1+R_{TE}) = e^{-u_0 d} \left( 1 + \frac{Y_0 - \hat{Y}_1}{Y_0 + \hat{Y}_1} \right) = e^{-u_0 d} \left( \frac{2Y_0}{Y_0 + \hat{Y}_1} \right) = e^{-u_0 d} \left( \frac{2\hat{Z}_1}{Z_0 + \hat{Z}_1} \right).$$

where impedance  $Z_i$  is defined as the reciprocal of  $Y_i$ .

Noting the difficulty of numerically integrating the Bessel functions when both transmitter and receiver are near the earth's surface, *Ryu et. al* introduce an additional term to insure convergence of the integral, using the limit relation:

$$\lim_{\lambda \rightarrow \infty} \frac{e^{-u_0 d}}{u_0} \left( \frac{\hat{Z}_1}{Z_0 + \hat{Z}_1} \right) = \frac{e^{-\lambda d}}{2\lambda}.$$

Adding and subtracting this term in the integral causes the integrand to vanish as  $\lambda$  increases. For example, the electric field is rewritten as:

$$E_{\theta} = -i\mu\omega Ia \left\{ \int_0^{\infty} \left[ \frac{e^{-u_0 d} \left( \frac{\hat{Z}_1}{Z_0 + \hat{Z}_1} \right) \lambda - \frac{e^{-\lambda d}}{2}}{u_0} \right] J_1(\lambda a) J_1(\lambda r) d\lambda \right. \\ \left. + \int_0^{\infty} \frac{e^{-\lambda d}}{2} J_1(\lambda a) J_1(\lambda r) d\lambda \right\}.$$

The second integral reduces to a finite form, and the electric field equation for a receiver on the earth's surface becomes:

$$E_{\theta} = -i\omega\mu a I(\omega) \left\{ \int_0^{\infty} \left[ \frac{e^{-u_0 d} \left( \frac{\hat{Z}_1}{Z_0 + \hat{Z}_1} \right) \lambda - \frac{e^{-\lambda d}}{2}}{u_0} \right] J_1(\lambda a) J_1(\lambda r) d\lambda \right. \\ \left. + \frac{ar}{2\pi} \int_{-1}^1 \text{Real} \left[ \frac{(1-x^2)^{1/2}}{(d^2 + 2iadx - a^2x^2 + r^2)^{3/2}} \right] dx \right\}. \quad (38)$$

Similarly, the magnetic field components are:

$$\begin{aligned}
 H_r = aI(\omega) & \left\{ \int_0^\infty \left[ e^{-u_0 d} \left( \frac{\hat{Z}_1}{Z_0 + \hat{Z}_1} \right) - \frac{e^{-\lambda d}}{2} \right] J_1(\lambda a) J_1(\lambda r) \lambda d\lambda \right. \\
 & \left. + \frac{3ar}{2\pi} \int_{-1}^1 \operatorname{Real} \left[ \frac{(1-x^2)^{1/2} (d+iax)}{(d^2 + 2iadx - a^2x^2 + r^2)^{5/2}} \right] dx \right\}, \quad (39)
 \end{aligned}$$

and

$$\begin{aligned}
 H_z = aI(\omega) & \left\{ \int_0^\infty \left[ \frac{e^{-u_0 d}}{u_0} \left( \frac{\hat{Z}_1}{Z_0 + \hat{Z}_1} \right) \lambda - \frac{e^{-\lambda d}}{2} \right] J_1(\lambda a) J_0(\lambda r) \lambda d\lambda \right. \\
 & + \frac{a}{\pi} \int_{-1}^1 \operatorname{Real} \left[ \frac{(1-x^2)^{1/2}}{(d^2 + 2iadx - a^2x^2 + r^2)^{3/2}} \right] dx \\
 & \left. - \frac{3ar^2}{2\pi} \int_{-1}^1 \operatorname{Real} \left[ \frac{(1-x^2)^{1/2}}{(d^2 + 2iadx - a^2x^2 + r^2)^{5/2}} \right] dx \right\}. \quad (40)
 \end{aligned}$$

### Forward and Inverse Programs

The computer modeling programs include the modified general field equations [38], [39], and [40] in existing forward and inverse programs that use hybrid numerical integration and nonlinear least-squares algorithms (*Dennis et al.*, 1981; *Anderson*, 1982, 1984, 1989). Double-precision accuracy of the numerical integration is verified by comparison with *Wait's* (1954) closed-form solution for a half-space model. The forward models presented in the next chapter were calculated using the forward program, and the inversion models presented in the survey examples chapter were calculated using the inversion program.

### Inclusion of the Air Layer

The structure of equations [38], [39], and [40] requires special treatment for the types of earth models studied here. The equations are set up for the case where the observation point is directly on the earth's surface ( $z=0$ ), and the source loop is placed at a distance  $d$  above the surface. However, in the real world, a vertical ( $H_r$ ) receiver loop cannot be placed with its center at the earth's surface, unless the bottom half of the loop is buried in the earth. In reality, the source and receiver loops are placed with their centers at a distance of 0.26 m above the earth; this distance represents the loop radius (0.15 m) plus the thickness of the loop housings and instrument supports (0.11 m).

Therefore, for this particular study, the real-world air layer between the loops and the surface is treated as the "top" layer of the earth, and the source and receiver are

placed directly on the surface of this layer by setting  $d=0$  in the equations. The top layer is assigned a conductivity and a dielectric permittivity equal to those of air, and a thickness equal to the real-world loop height of 0.26 m.

### EM Field Parameters Measured

The electromagnetic field quantities presented here are based upon ratios of the  $H_r$  and  $H_z$  fields. The main reasons for choosing this type of measurement are instrument limitations described in the instrumentation chapter. The field quantities selected for measurement are the polarization ellipse of the total magnetic field and the ratio of the radial magnetic field to the spatial gradient of the total vertical magnetic field. The "total" field refers to the combined field of the source loop and the field induced in the earth.

#### The Magnetic Field Polarization Ellipse

The components of the magnetic field generally have different amplitudes and phases. In this case, the total field vector is polarized, and traces an ellipse in space as shown in Figure 3. The vertical and radial magnetic fields are defined as:

$$H_z e^{i\phi_z}, \quad H_r e^{i\phi_r}, \quad \Delta\phi = \phi_z - \phi_r,$$

where  $H_{z,r}$  and  $\phi_{z,r}$  are respectively the amplitude and the phase. The two parameters which characterize the polarization ellipse are its tilt angle  $\alpha$  and ellipticity  $\epsilon$ . The tilt

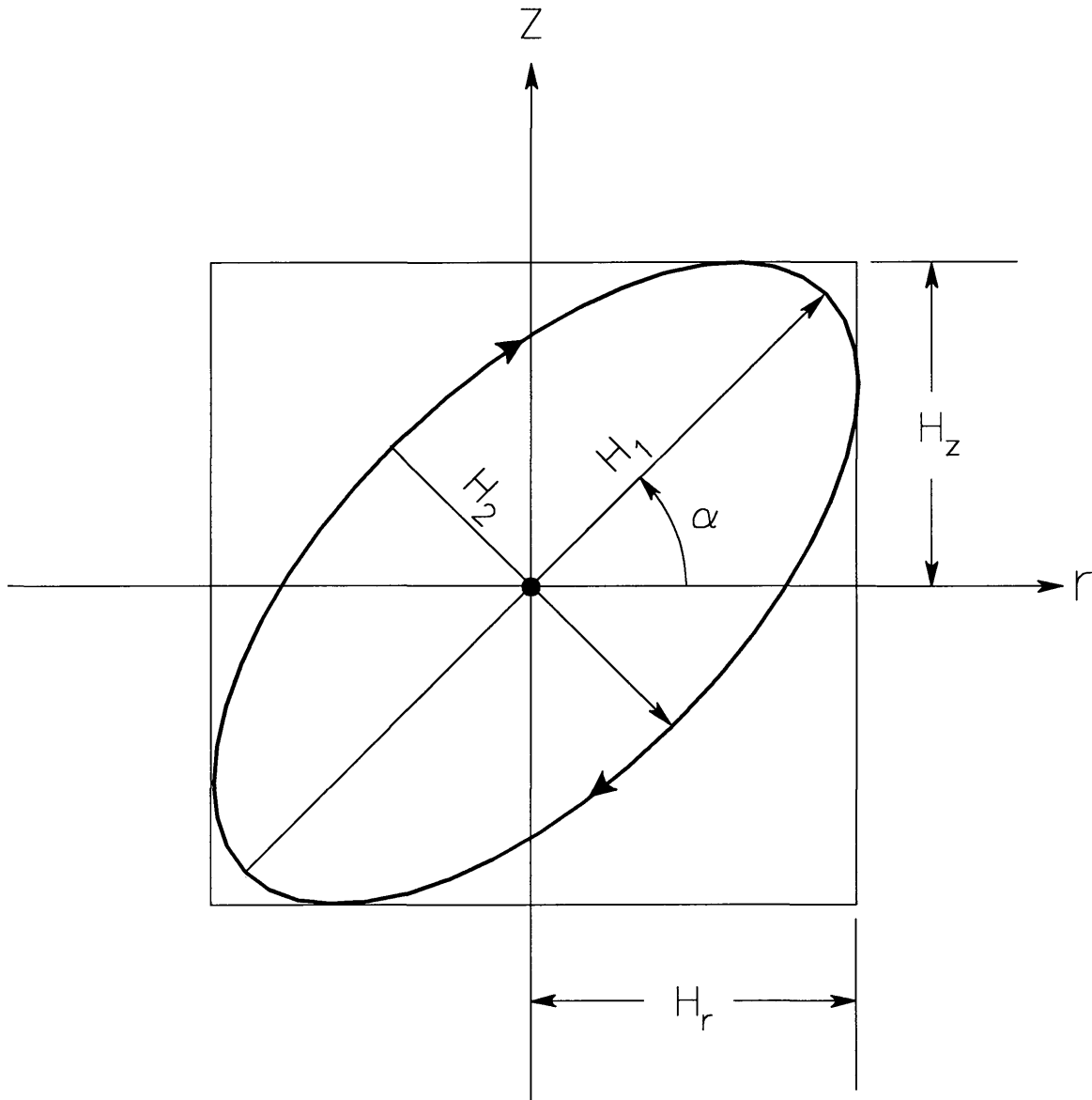


Figure 3. Parameters of the magnetic field polarization ellipse.

angle is defined as the inclination of the major axis above the horizontal (*Smith and Ward, 1974*):

$$\alpha = \frac{1}{2} \tan^{-1} \left( \pm \frac{2H_r H_z \cos \Delta \phi}{H_r^2 - H_z^2} \right). \quad (41)$$

The ellipticity is defined as the ratio of the minor to the major axis (*Frischknecht et al., 1991*):

$$\epsilon = \frac{H_2}{H_1} = \frac{\frac{H_z}{H_r} \sin \phi}{\left( \frac{H_z}{H_r} \right)^2 \sin^2 \alpha + 2 \frac{H_z}{H_r} \sin \alpha \cos \alpha \cos \phi + \cos^2 \alpha}. \quad (42)$$

An alternate formula for ellipticity is:

$$\epsilon = \tan \left[ \frac{1}{2} \sin^{-1} \left( \frac{2H_r H_z \sin \Delta \phi}{H_r^2 + H_z^2} \right) \right]. \quad (43)$$

### The Spatial Gradient

A spatial gradient was chosen for the purpose of combining measurements using multiple, short  $r$  spacings into a single quantity. The magnetic field components are computed for 2 different spacings,  $r$  and  $r-\Delta r$ , as shown in Figure 4. The primary (free-space) field has a different amplitude for each spacing; in order to remove this influence, normalized components are computed (i.e., the field components at each spacing are normalized by the primary field amplitude at that spacing). The spatial gradient quantity is defined as the ratio of the  $H_r$  field at the closer spacing to the gradient of the  $H_z$  field:

$$\text{Spatial Gradient} = \frac{H_{r1}}{\left( \frac{H_{z2} - H_{z1}}{\Delta r} \right)}. \quad (44)$$

Since the field components are complex numbers, the spatial gradient can be characterized by its amplitude and phase.

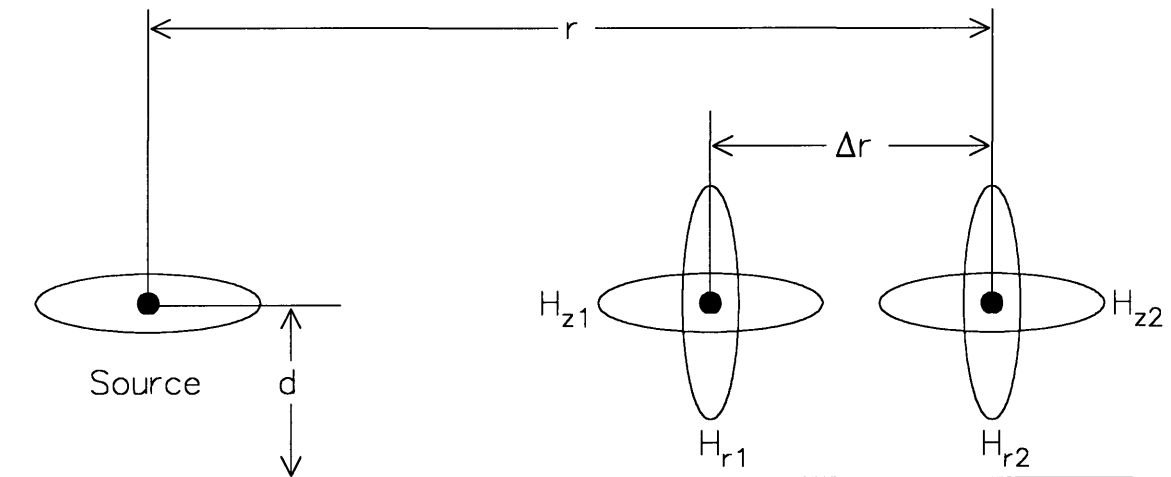


Figure 4. Loop geometry for spatial gradient (SPATGRAD) measurement.

## FORWARD MODEL EXAMPLES

This chapter illustrates the influence of displacement currents on EM field observations, and provides information for evaluating the effectiveness of high-frequency sounding for some typical survey goals of shallow mapping applications, such as measuring the electrical parameters of a half-space, mapping top layer thickness and electrical parameters of a two-layer model, and detecting a thin buried layer. Although a fairly large amount of data are presented here, they provide only a limited overview of high-frequency sounding, given the scope of possible earth models. The relevant observations and conclusions drawn from the models are discussed and summarized in the conclusions and recommendations chapter.

The computer forward modeling program is used to compute the tilt angle and ellipticity of the polarization ellipse as defined by equations [41] and [42], and the amplitude and phase of the spatial gradient of the total magnetic field as defined by equation [44]. The layer parameters are thickness ( $h$ ), resistivity ( $\rho$ ), and relative dielectric permittivity ( $K$ ). Table 2 summarizes the parameters of each model. All of the models use a horizontal-loop source; both the source and the receiver loops have a radius of 0.15 m and centers 0.26 m above the earth. The polarization ellipse calculations use  $r$  spacings of 2 or 4 m; the spatial gradient calculations all use  $r = 2$  m, and  $\Delta r = 0.5$  m.

Table 2: Summary of forward model parameters. Resistivity ( $\rho$ ) =  $\Omega \cdot m$ , relative dielectric permittivity ( $K$ ) = dimensionless, layer thickness ( $h$ ) = m. Variable parameter value indicated by (\*).

| Model # | $\rho_1$ | $\rho_2$ | $\rho_3$ | $K_1$ | $K_2$ | $K_3$ | $h_1$ | $h_2$ | Figures     |
|---------|----------|----------|----------|-------|-------|-------|-------|-------|-------------|
| 1       | 2000     | -        | -        | (*)   | -     | -     | -     | -     | 5,6         |
| 2       | 50       | -        | -        | (*)   | -     | -     | -     | -     | 7,8         |
| 3       | (*)      | -        | -        | 10    | -     | -     | -     | -     | 9,11        |
| 4       | 200      | 50       | -        | 5     | 20    | -     | (*)   | -     | 12,13,14,15 |
| 5       | 50       | 200      | -        | 20    | 5     | -     | (*)   | -     | 16,17,18,19 |
| 6       | 200      | (*)      | -        | 5     | 20    | -     | 1,2   | -     | 20,21,22    |
| 7       | 50       | (*)      | -        | 20    | 5     | -     | 1,2   | -     | 21,22,23    |
| 8       | 200      | 50       | -        | 5     | (*)   | -     | 1,2   | -     | 26,27       |
| 9       | 50       | 200      | -        | 20    | (*)   | -     | 1,2   | -     | 28,29       |
| 10      | 100      | 200      | 100      | 0     | 0     | 0     | 1     | (*)   | 30,32       |
| 11      | 100      | 200      | 100      | 10    | 10    | 10    | 1     | (*)   | 31,32       |
| 12      | 100      | 50       | 100      | 0     | 0     | 0     | 1     | (*)   | 32          |
| 13      | 100      | 50       | 100      | 10    | 10    | 10    | 1     | (*)   | 32          |
| 14      | 100      | 100      | 100      | 20    | 10    | 20    | 1     | (*)   | 32          |
| 15      | 100      | 100      | 100      | 10    | 20    | 10    | 1     | (*)   | 32,33       |
| 16      | 100      | (*)      | 100      | 10    | 10    | 10    | 1     | 0.2   | 34,35       |
| 17      | 100      | 100      | 100      | 10    | (*)   | 10    | 1     | 0.2   | 36,37       |

The present instrument is capable of measurement only in the frequency range 300 kHz to 30 MHz. The model data are calculated over a wider frequency range, to an upper frequency of 50 MHz and a low frequency as small as 10 kHz for certain models. For purposes of comparing the model calculations with the actual resolving power of the instrument, it is noted that the instrument sensitivity for the given  $r$  spacings is sufficient to detect changes of about 2 degrees in the tilt angle of the polarization ellipse or the phase of the spatial gradient, and 0.02 change in polarization ellipse ellipticity or spatial gradient amplitude.

#### Half-Space Models: Influence of Dielectric Permittivity

A simple homogeneous half-space model serves to demonstrate the effect of displacement currents on EM field observations. Models 1 and 2 (see Table 2) use high and low  $\rho$  values and a variable  $K$  to illustrate two "limiting" cases for the relative magnitude of conduction currents. Model 3 illustrates a different effect on curve shape when  $K$  is fixed and  $\rho$  varies.

#### Model 1: Resistive Half-Space

The polarization ellipse parameters shown in Figure 5 are for a half-space with a relatively large  $\rho$  of 2000  $\Omega\cdot\text{m}$ , and  $K$  varying from 0 to 30 (Model 1). This model could represent dry earth media; although  $K$  as large as 30 is unlikely. For a large  $\rho$ , even a simple change of  $K$  from 0 (quasi-static) to 1 (free-space value) has a significant

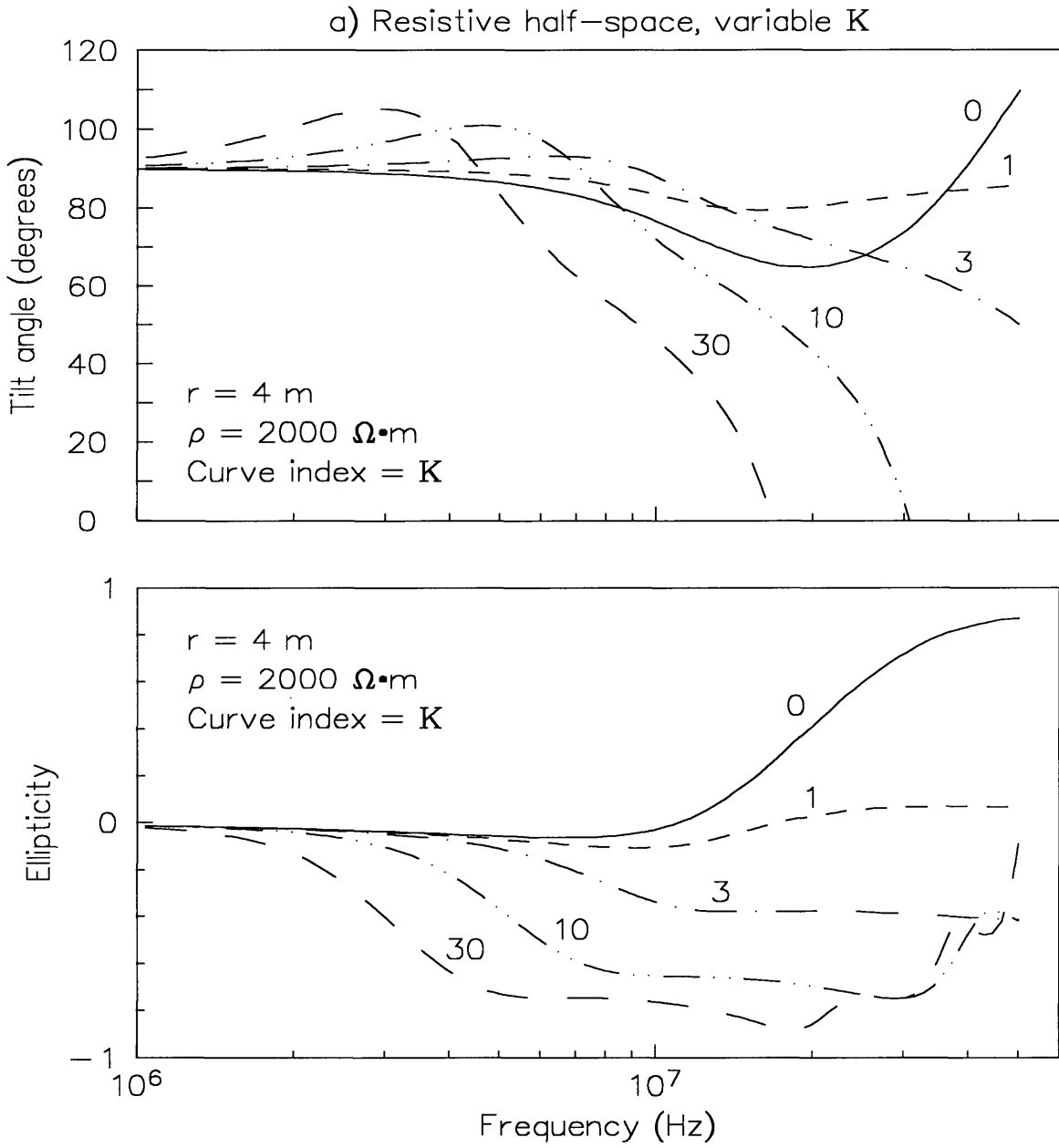


Figure 5. Calculated polarization ellipse tilt angle and ellipticity for a half-space with a large  $\rho$  and a variable  $K$  (Model 1).

effect on curve shape at frequencies above 6 MHz. When  $K$  increases to 30, the change in curve shape begins to show at 1 MHz. The shape of the tilt angle curves is similar to computed tilt data presented by *Ryu et al.* (1970).

The curve shape of the spatial gradient response for the same model (Figure 6) is more sensitive to  $K$ , in that the change in shape is noticeable at frequencies around 1 MHz for  $K = 1$ , and at frequencies as low as 100 kHz for the amplitude curves when  $K = 30$ . The curves for  $K = 0$  and 1 show some numerical noise at a few discrete frequencies.

### Model 2: Conductive Half-Space

A half-space with a relatively small  $\rho$  of 50  $\Omega\cdot\text{m}$  (Model 2) is representative of a variety of wet earth media. The effect of varying  $K$  is evident in the polarization ellipse parameters shown in Figure 7, although the curves for  $K \leq 10$  are virtually indistinguishable from the  $K = 0$  curve, and are not shown. An interesting feature of this model is the appearance of oscillatory peaks in both the tilt and the ellipticity curves at frequencies above 10 MHz for  $K = 20$  and 40. The frequency at which the first peaks appear is inversely proportional to  $K$ . These are not artifacts of the computer plotting method or quadrant shifts imposed by computer angular conventions. Similar complicated shapes are seen in examples from *Ward and Dey* (1971), and in real-world data presented in the field survey examples chapter of this study.

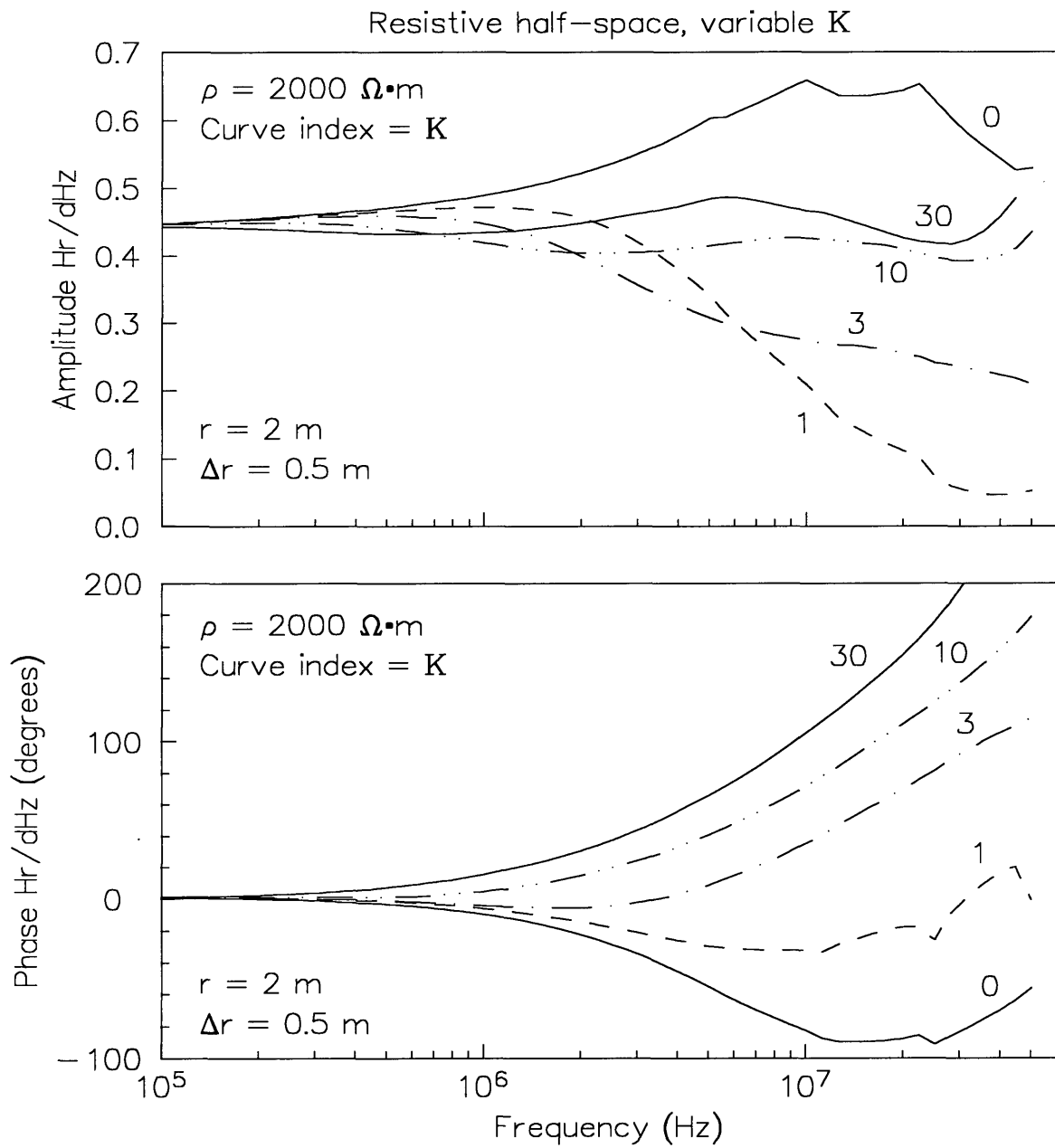


Figure 6. Calculated spatial gradient amplitude and phase for a half-space with a large  $\rho$  and a variable K (Model 1).

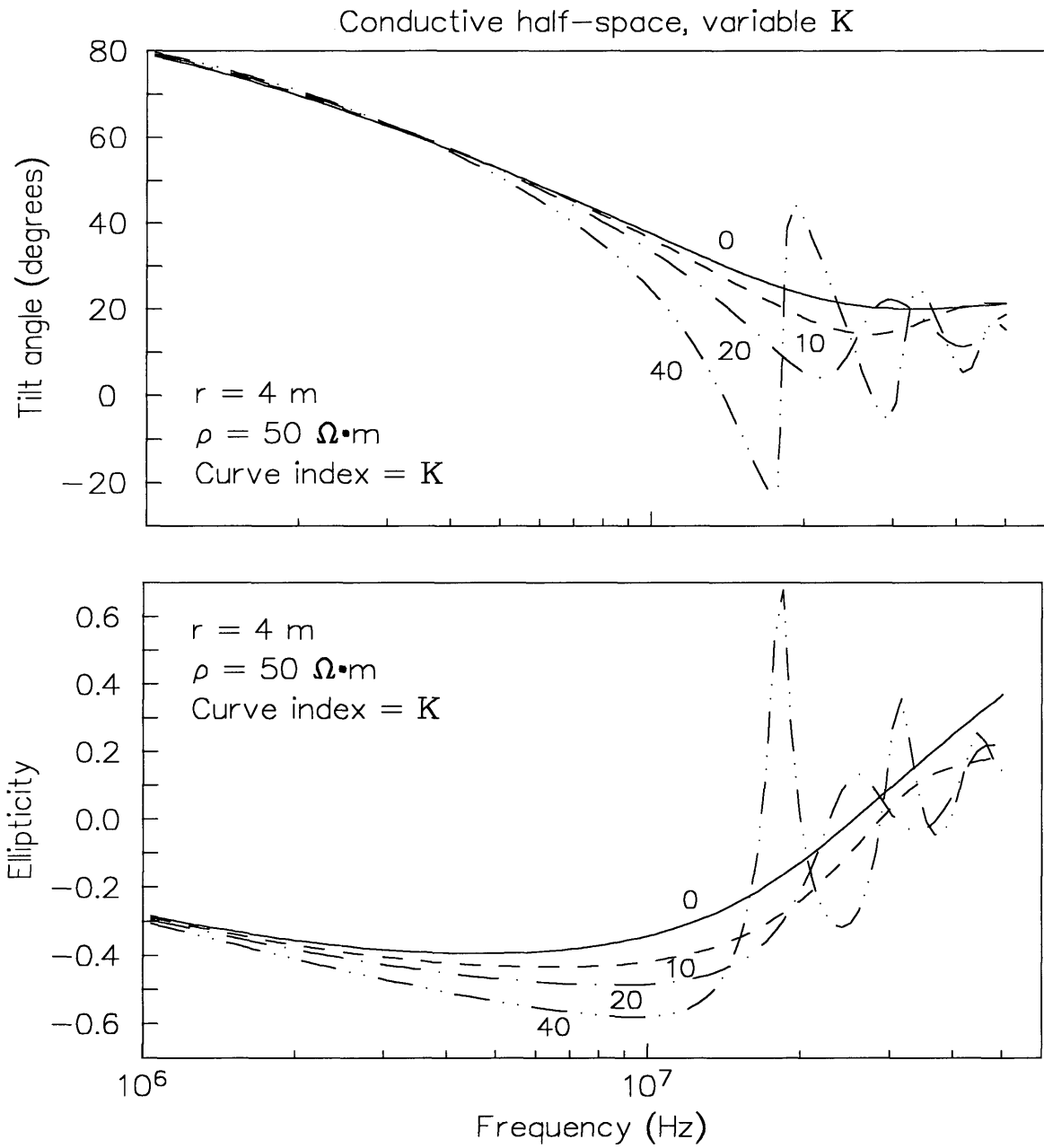


Figure 7. Calculated polarization ellipse tilt angle and ellipticity for a half-space with a small  $\rho$  and a variable K (Model 2).

The amplitude of the spatial gradient data (Figure 8) for this model is more sensitive to small  $K$  values than the polarization ellipse data. Unlike the polarization ellipse, the amplitude curves are well-separated above 10 MHz for  $K$  values between 0 and 10. The phase curves are similar to the polarization ellipse curves, i.e., they are nearly indistinguishable for  $K < 10$ . The spatial gradient curves for this model do not show oscillatory behavior.

### Model 3: Effect of Varying Resistivity

It was noted in Figure 7 that oscillatory peaks in the curves appear at a frequency which is inversely proportional to  $K$ . The effect of  $\rho$  on the peaks is shown in the polarization ellipse data of Figure 9. Model 3 uses  $K = 10$  and  $\rho$  varying from 50 to 1000  $\Omega \cdot \text{m}$ . The resistivity strongly influences the shape and size of the peaks but has little effect on the frequency where they occur, especially in the ellipticity curves. The first ellipticity peak is near 40 MHz, and vanishes for  $\rho < 50$ . The size and sharpness of the peak reaches a maximum as  $\rho$  approaches 200, then diminishes for larger  $\rho$ . The tilt oscillations become larger and more complicated as  $\rho$  increases; those curves which run off the bottom of the plot are truncated to avoid clutter from oscillations superimposed on 180-degree shifts.

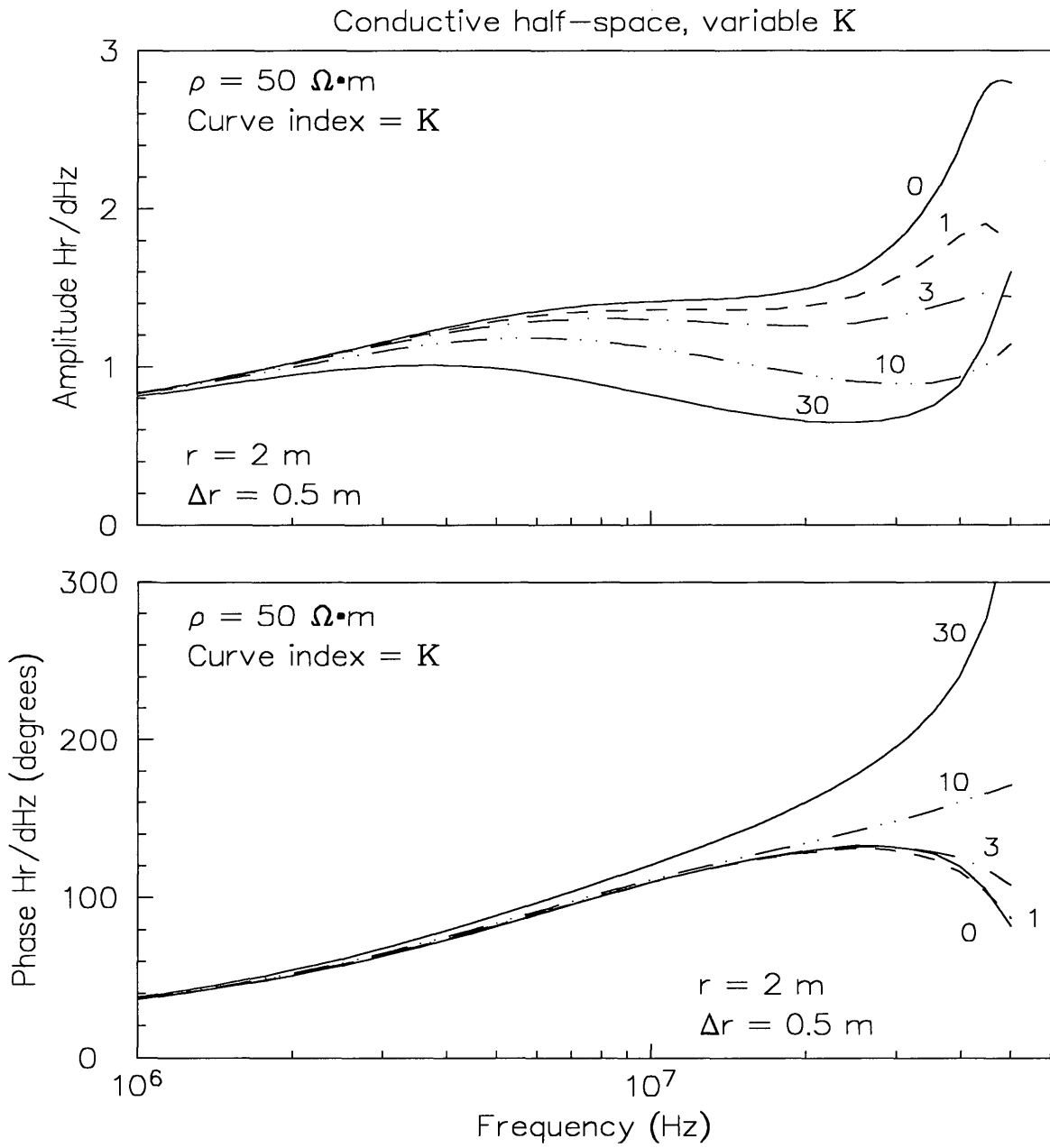


Figure 8. Calculated spatial gradient amplitude and phase for a half-space with a small  $\rho$  and a variable K (Model 2).

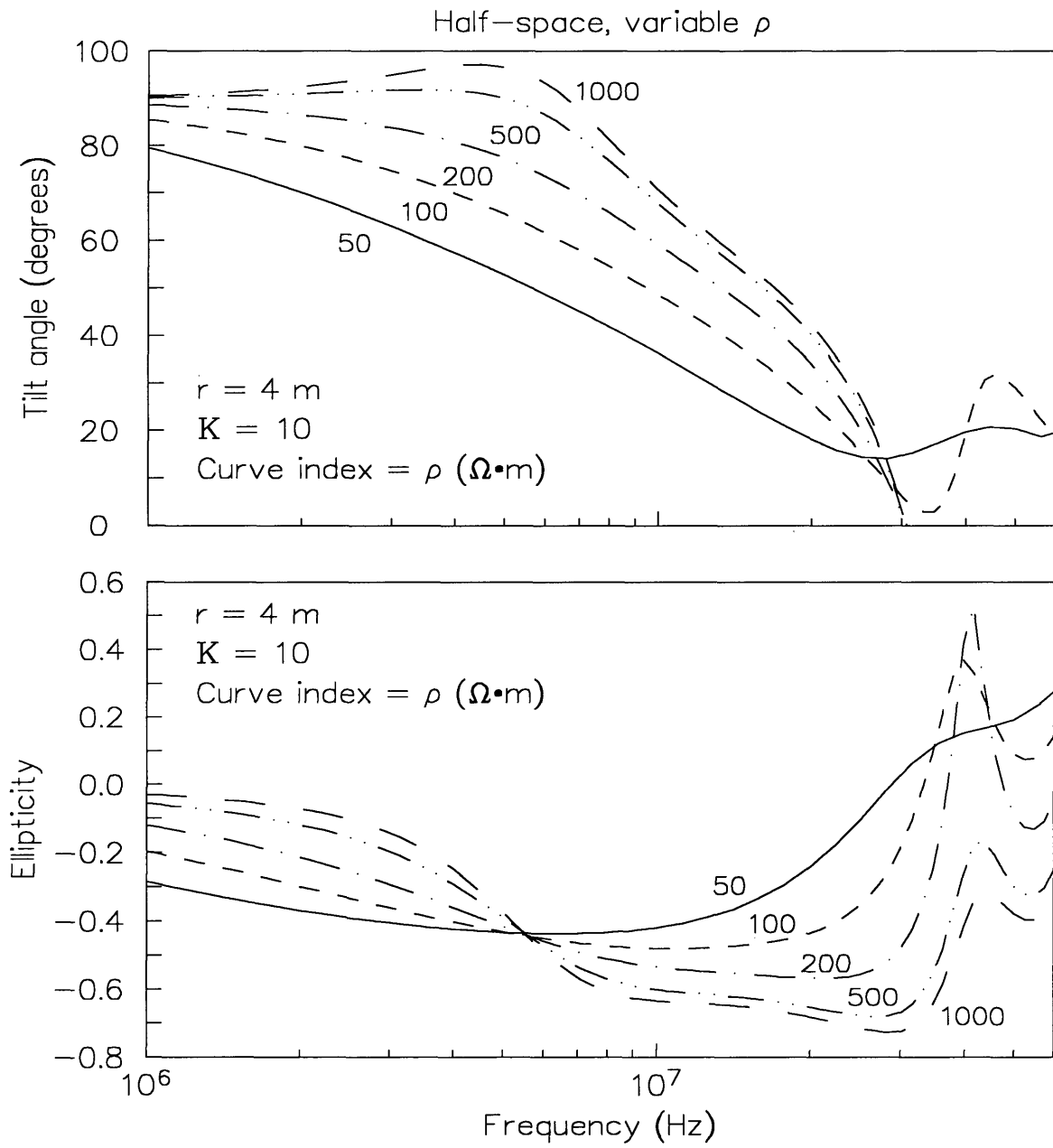


Figure 9. Calculated polarization ellipse tilt angle and ellipticity for a half-space with  $K = 10$  and a variable  $\rho$  (Model 3).

Figure 10 compares  $K$  to the frequency where the first ellipticity peak appears, for various  $\rho$  values. The curves are approximately linear on a logarithmic scale, with a slope and intercept that are fairly insensitive to  $\rho$ . For a homogeneous half-space, an approximate value for  $K$  could be obtained directly from the frequency at an identifiable ellipticity peak. However, the present instrument could not be used for direct estimation if  $K$  is less than about 20, since the highest operating frequency is 30 MHz.

The effect of  $\rho$  on the spatial gradient (Figure 11) is mainly to attenuate the amplitude and decrease the phase as  $\rho$  increases. The phase curves become insensitive to  $\rho$  as the frequency exceeds 20 MHz, while the amplitude curves are strongly affected over the full computed range.

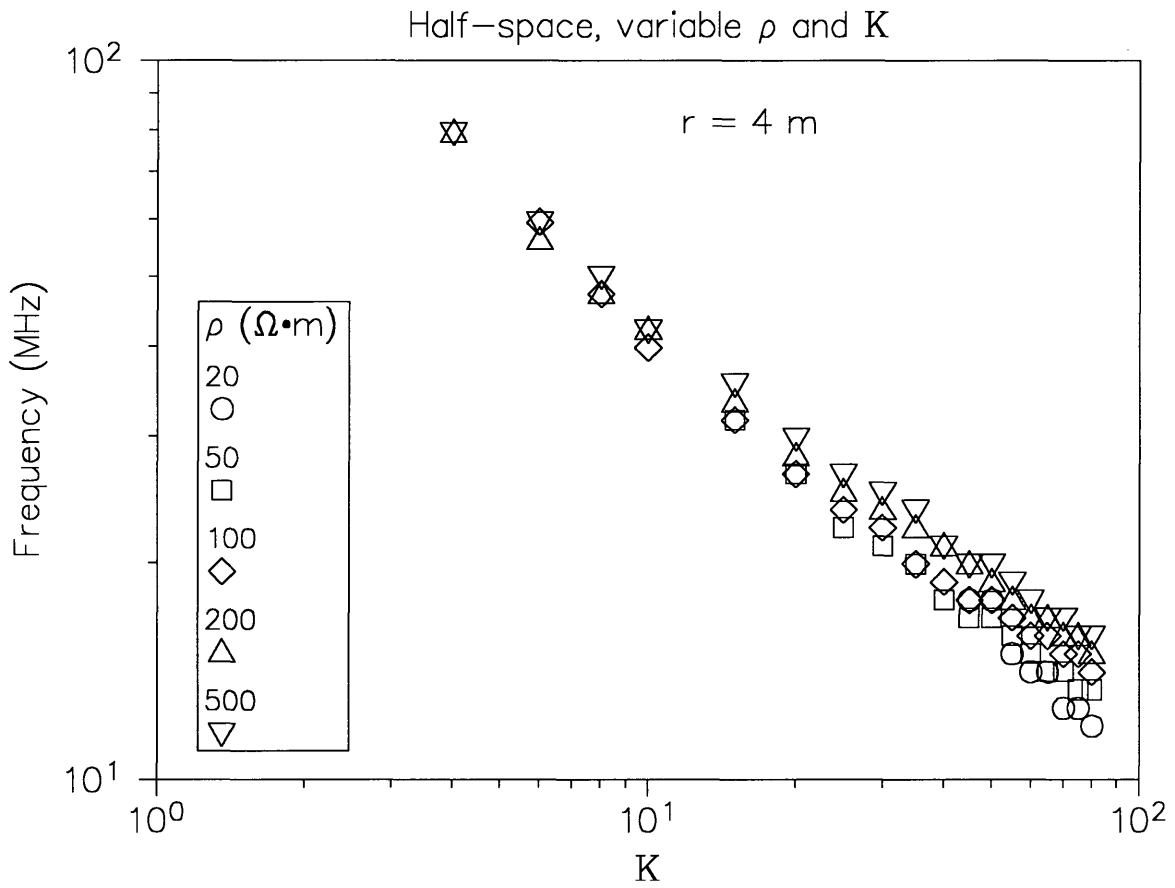


Figure 10. A graph comparing K of a half-space to the frequency where the first ellipticity peak occurs. The symbols represent different  $\rho$  values.

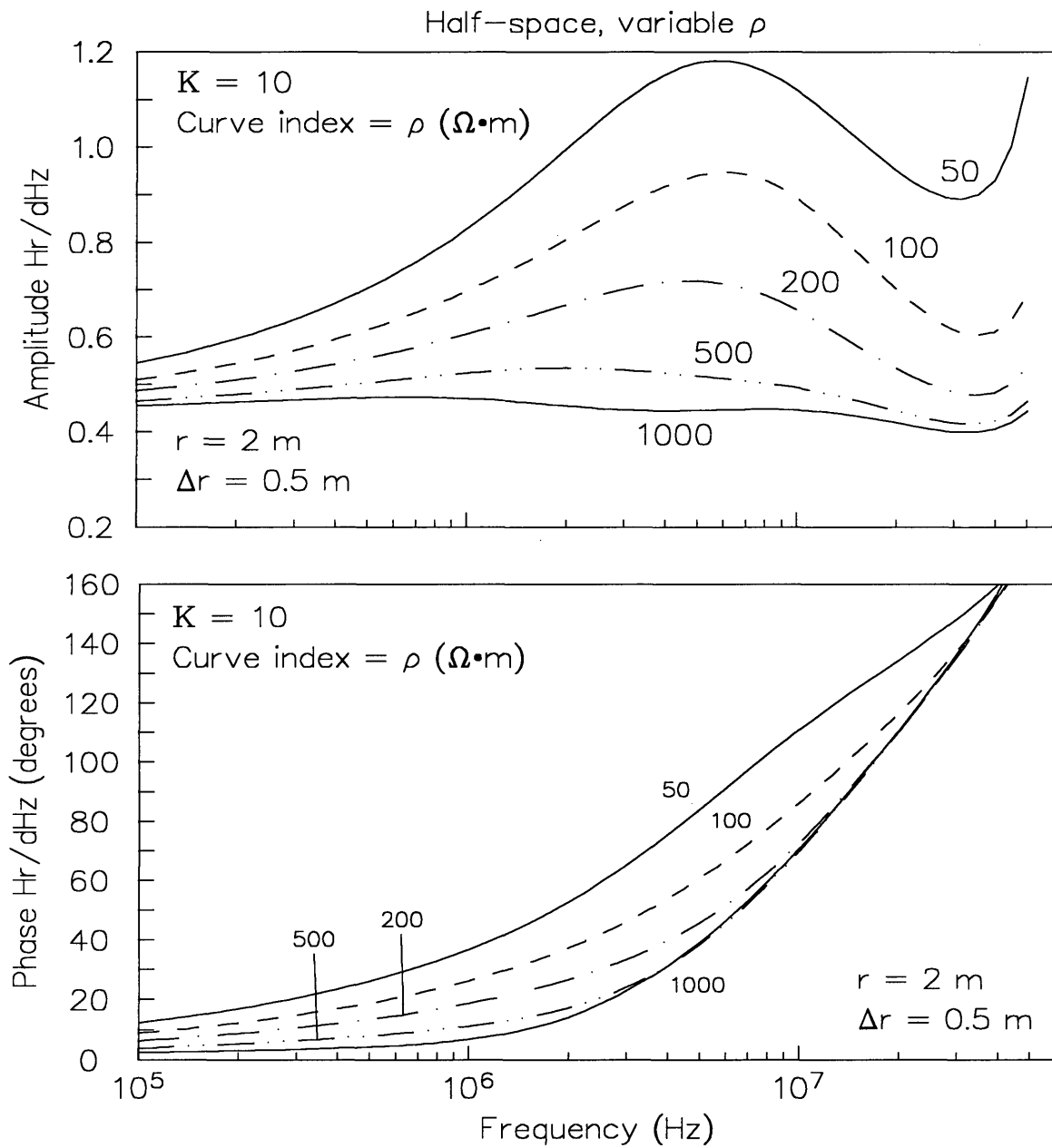


Figure 11. Calculated spatial gradient amplitude and phase for a half-space with  $K = 10$  and a variable  $\rho$  (Model 3).

### Two-Layer Models

This section investigates the sensitivity of high-frequency measurements to variations of certain parameters of a two-layer earth, in particular the top layer thickness  $h$ , and the electrical parameters of the basement,  $\rho_2$  and  $K_2$ .

#### Effect of Top Layer Thickness

Models 4 and 5 (see Table 2) investigate the ability to detect variations in the thickness of the top layer of a two-layer earth. Model 4 has a relatively resistive, low-dielectric layer overlying a relatively conductive, high-dielectric basement; the layer boundary might represent a water table, or the boundary between a soil layer and a wet clay basement. Model 5 uses the same parameters but has the layers reversed; the top layer is relatively conductive and has a high  $K$ , and the basement is resistive and has a low  $K$ . Here, the layers might represent a surface clay, or the penetration of a wetting front into dry soil.

Model 4: Resistive, Low-K Top Layer. Polarization ellipse measurements for Model 4 are calculated for  $r$  spacings of 2 m (Figure 12) and 4 m (Figure 13). In both cases, the tilt angle and ellipticity are sensitive to variation of  $h$  when  $h$  is less than the  $r$  spacing, and insensitive to variations when  $h$  exceeds the  $r$  spacing. In Figure 12, the curves are well-separated for  $h \leq 2$  m, but nearly indistinguishable for  $h > 2$  m. The same  $r$ -dependence is seen in Figure 13, where the curves are well-separated for  $h \leq 4$

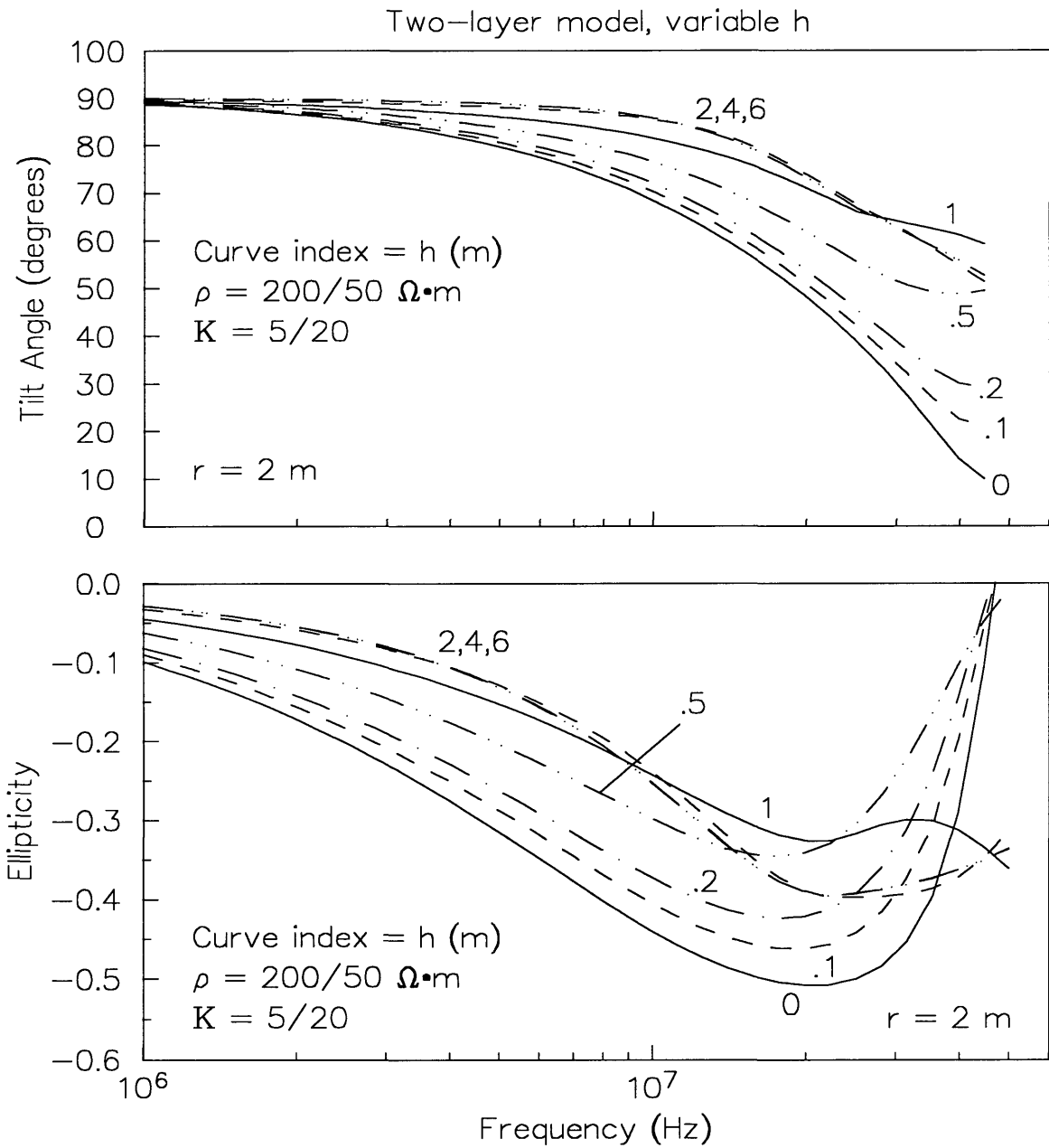


Figure 12. Calculated polarization ellipse tilt angle and ellipticity using  $r=2$  m for a two-layer model with a relatively high- $\rho$ , low- $K$  top layer of variable thickness (Model 4).

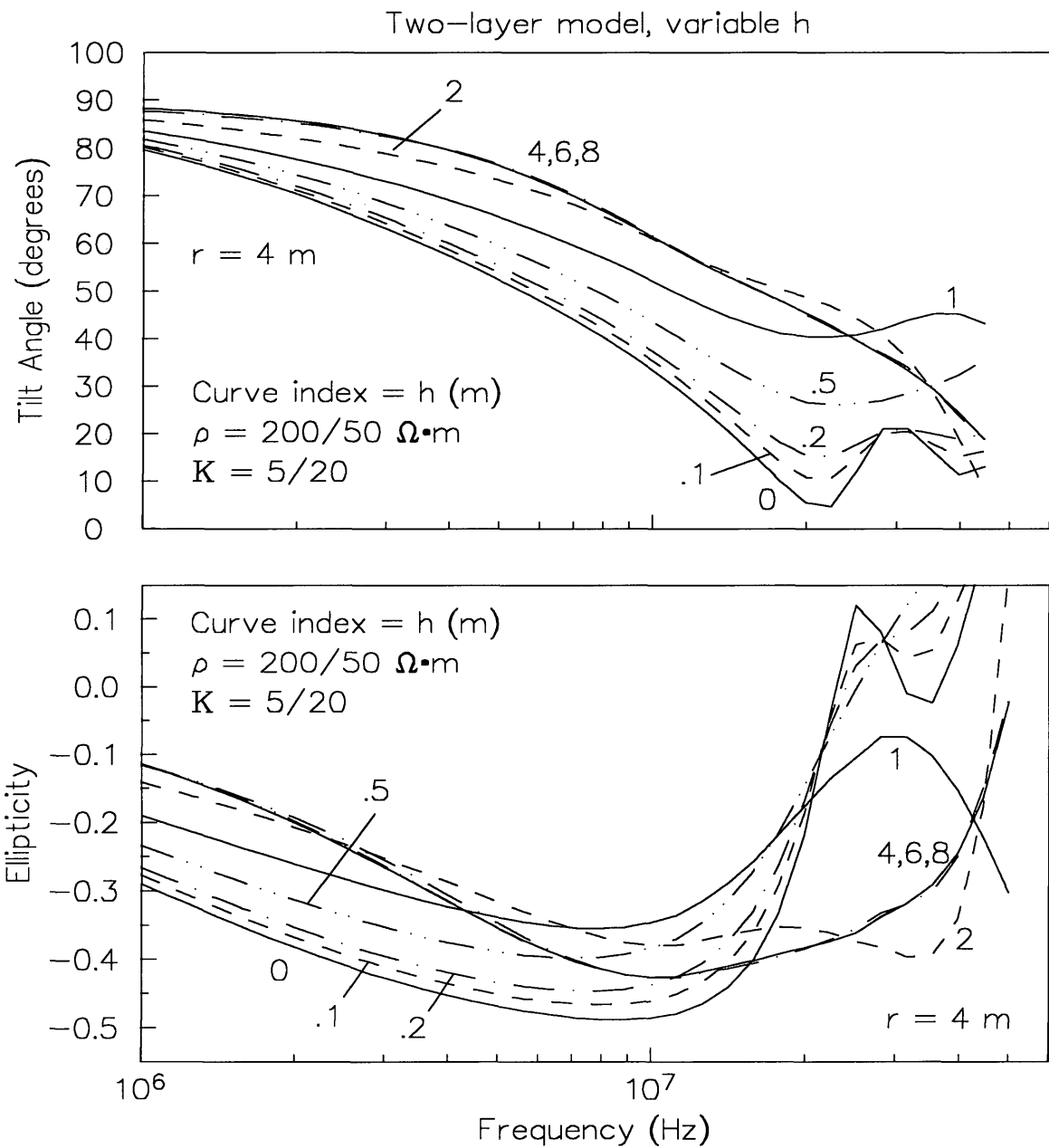


Figure 13. Calculated polarization ellipse tilt angle and ellipticity using  $r=4$  m for a two-layer model with a relatively high- $\rho$ , low-K top layer of variable thickness (Model 4).

m, and indistinguishable for  $h > 4$  m. In both figures, the general effect of increasing  $h$  is to shift both the tilt angle and the ellipticity curves upwards. The ellipticity curves abruptly change shape at frequencies above 10 MHz when  $h$  exceeds  $0.5r$ , reflecting the loss of sensitivity to the lower portion of the top layer.

Spatial gradient measurements for Model 4 show a dramatic increase in depth of investigation relative to the polarization ellipse measurements. The calculated data for  $h$  values less than the  $r$  spacing of 2 m are shown in Figure 14; as with the polarization ellipse data, the curves are well separated. However, unlike the polarization ellipse data, the spatial gradient measurements remain sensitive to  $h$  when it exceeds  $r$ . Figure 15 shows data for  $h$  values up to 10 m; the amplitude curves for  $h = 6$  m and  $h = 10$  m remain well separated at the lower frequencies despite the fact that  $h$  is, respectively, three times and five times larger than  $r$ . The effect of increasing  $h$  is to shift the curves downwards until  $h = 1$  m (Figure 14); when  $h$  exceeds 1 m, the phase curves continue to shift downwards but the amplitude curves are shifted upwards (Figure 15). When  $h$  exceeds 0.5 m, the amplitude curves abruptly change of shape at frequencies above 10 MHz.

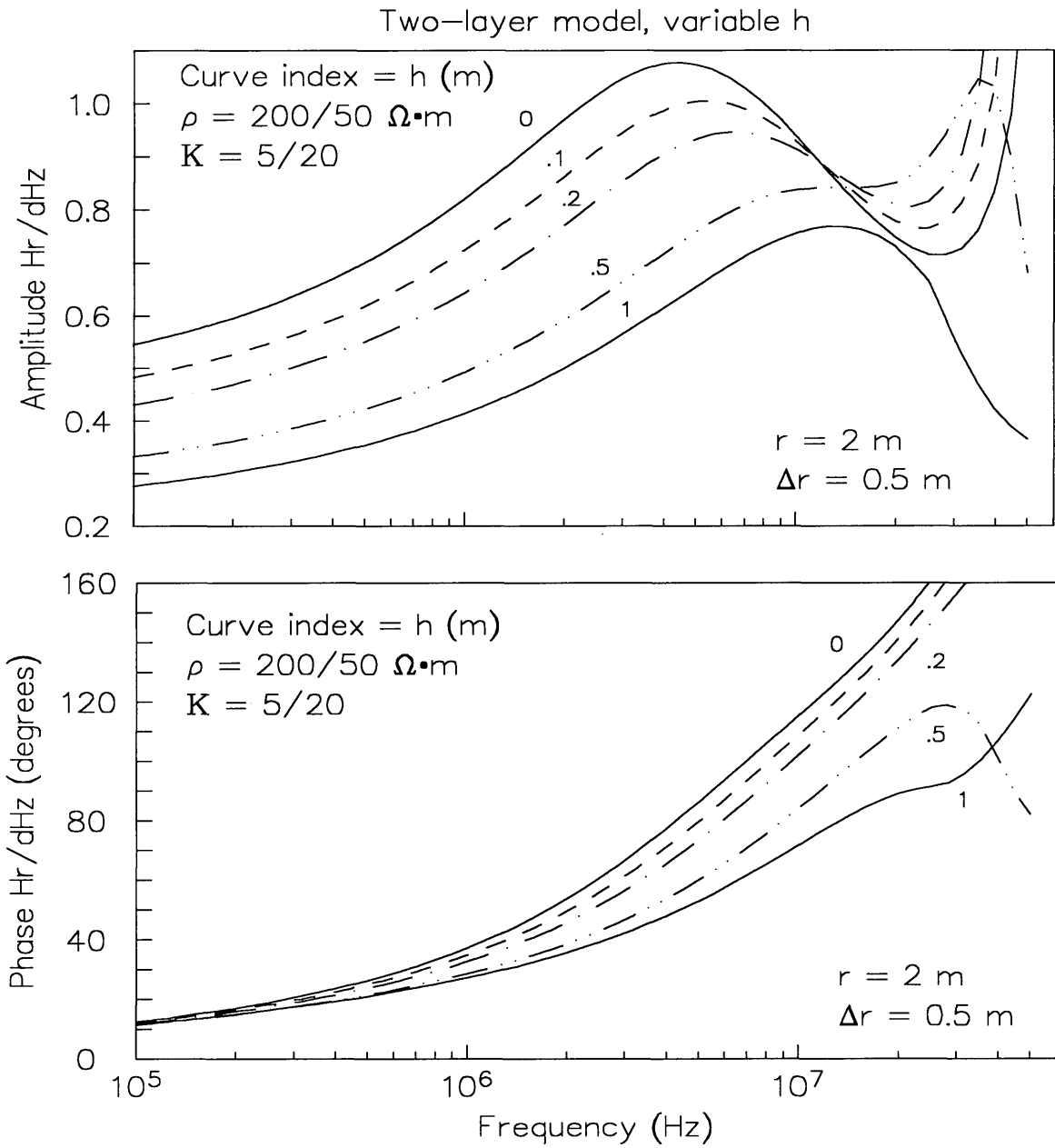


Figure 14. Calculated spatial gradient amplitude and phase for a two-layer model with a relatively high- $\rho$ , low- $K$  top layer of variable thickness,  $h < r$  (Model 4).

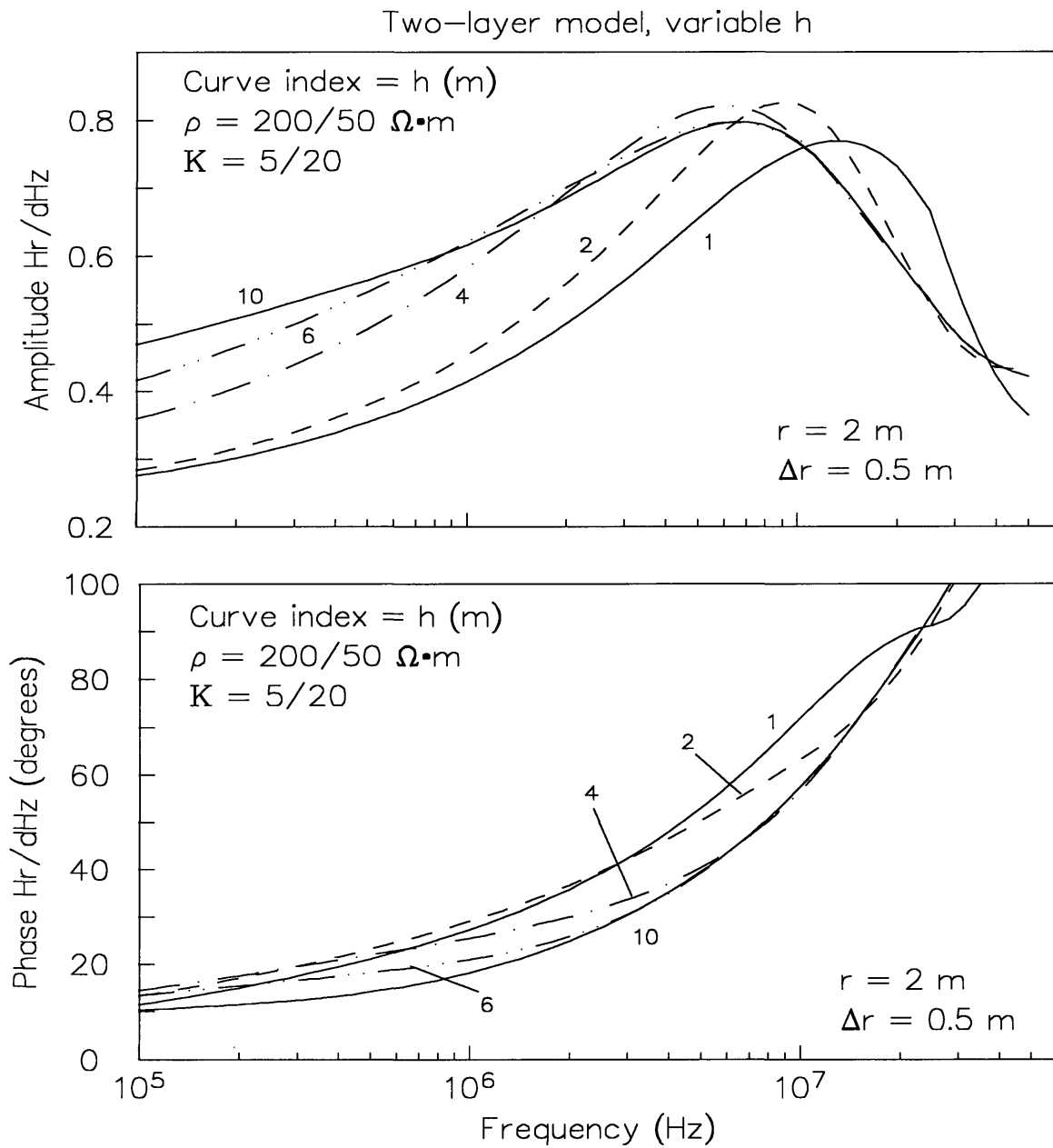


Figure 15. Calculated spatial gradient amplitude and phase for a two-layer model with a relatively high- $\rho$ , low- $K$  top layer of variable thickness,  $h$  exceeds  $r$  (Model 4).

Model 5: Conductive, High-K Top Layer. The calculated polarization ellipse data is shown for  $r$  spacings of 2 m (Figure 16) and 4 m (Figure 17). The sensitivity of the curves to  $h$  is similar to that for Model 4, in that the curve separation rapidly decreases when  $h$  exceeds  $0.5r$ . The general effect of increasing  $h$  is to shift the curves downwards, the opposite of the effect on Model 4. As with Model 4, at some value of  $h$  there is an abrupt change of curve shape at frequencies above 10 MHz. For Model 5 the change manifests when  $h = 0.25r$ , a smaller value than for Model 4. This is to be expected since the skin depth in the top layer is smaller for Model 5 than for Model 4, therefore a smaller  $h$  is sufficient to reach the point where the model begins to behave as a half-space.

The influence of a diminished skin depth is apparent in the calculated spatial gradient data. As with Model 4, the curves are well-separated for  $h \leq 1$  m (Figure 18); however, for Model 5 the curves become indistinguishable when  $h$  exceeds 4 m (Figure 19), instead of remaining separated up to  $h = 10$  m as in Model 4. The effect of increasing  $h$  is the opposite of that in Model 4; the curves are shifted upwards until  $h$  reaches 0.5 m, then the amplitude curves are shifted downwards.

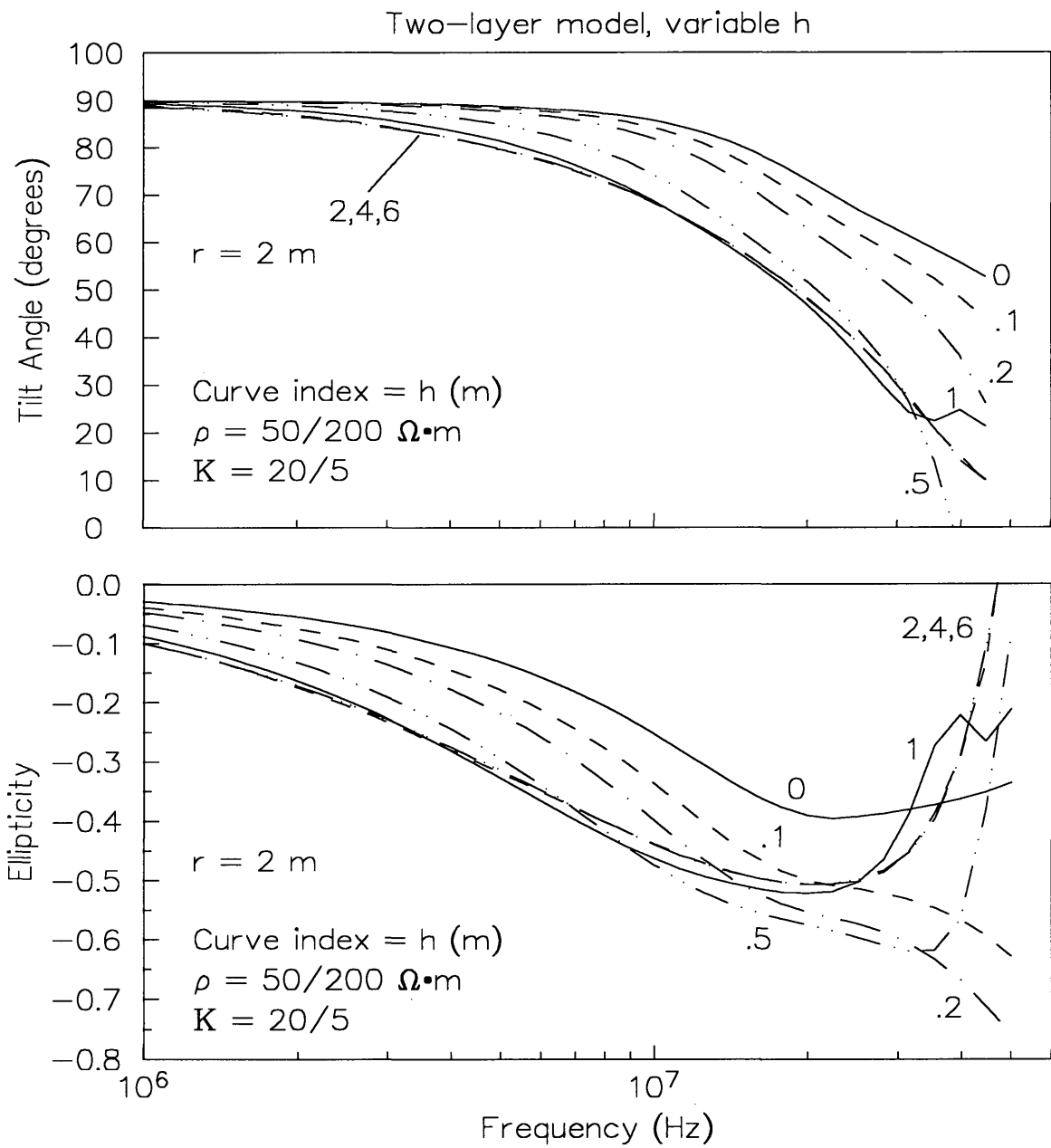


Figure 16. Calculated polarization ellipse tilt angle and ellipticity for a two-layer model with a relatively low- $\rho$ , high-K top layer of variable thickness,  $r = 2 \text{ m}$  (Model 5).

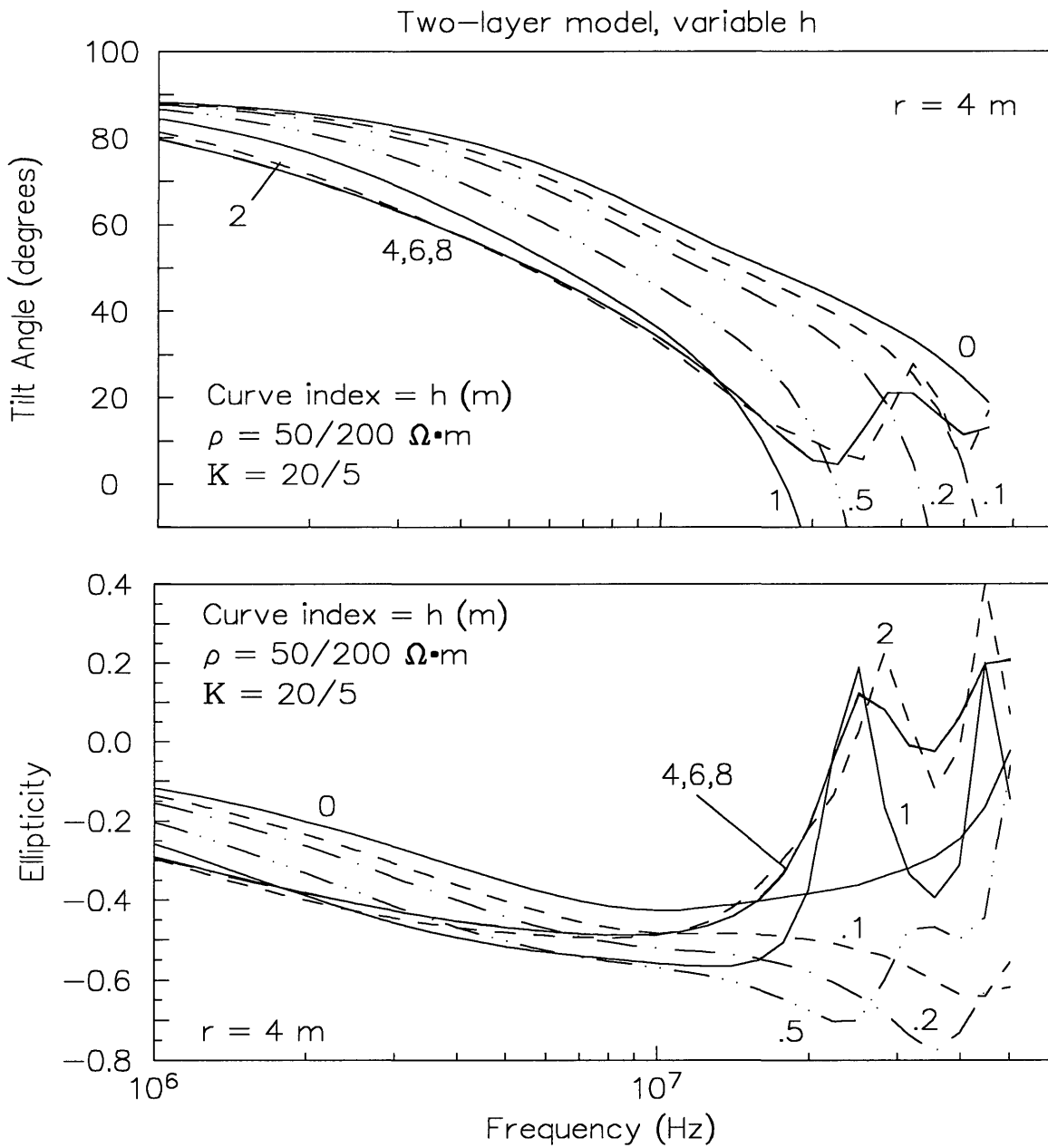


Figure 17. Calculated polarization ellipse tilt angle and ellipticity for a two-layer model with a relatively low- $\rho$ , high-K top layer of variable thickness,  $r = 4 \text{ m}$  (Model 5).

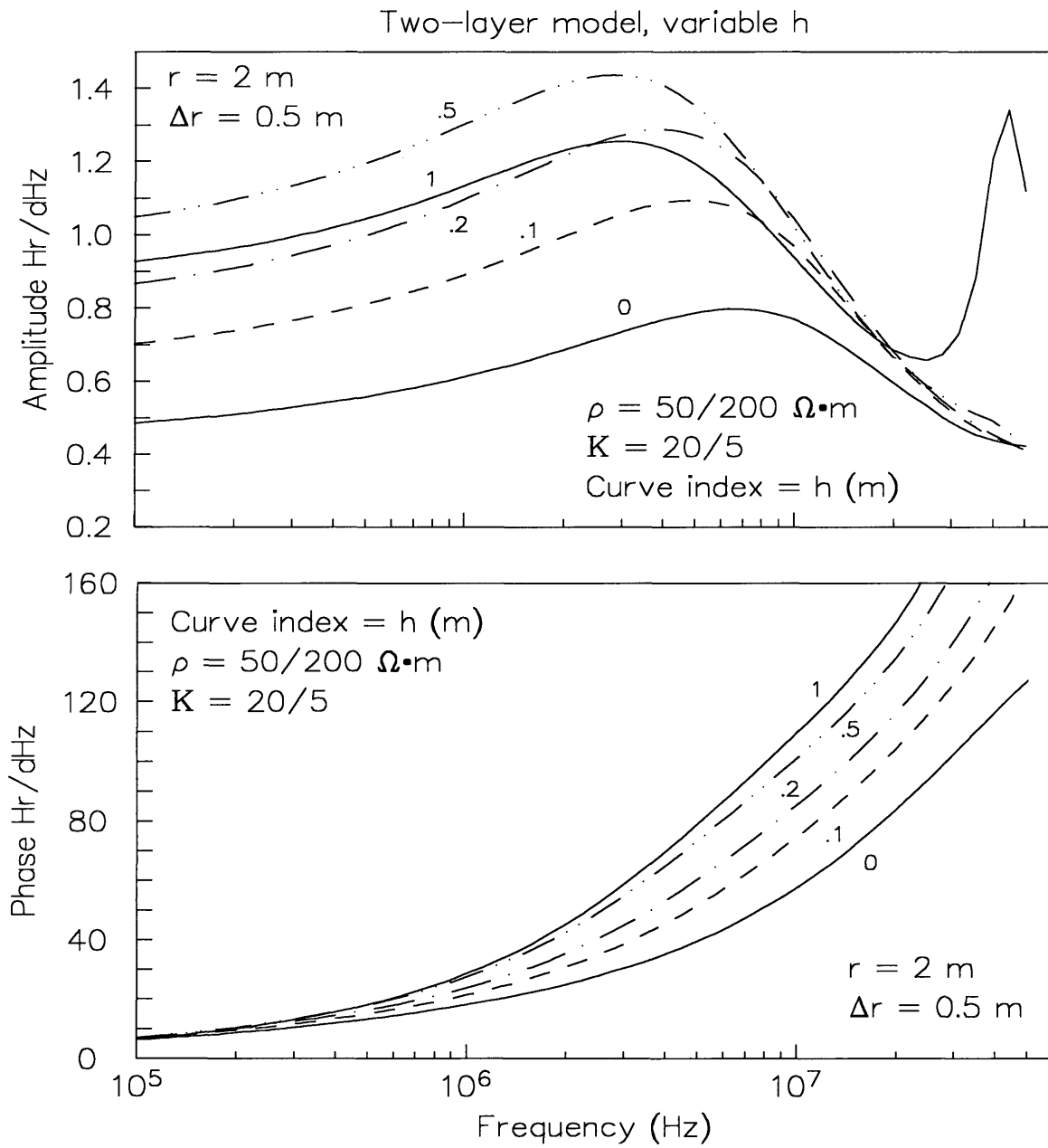


Figure 18. Calculated spatial gradient amplitude and phase for a two-layer model with a relatively low- $\rho$ , high- $K$  top layer of variable thickness,  $h < r$  (Model 5).

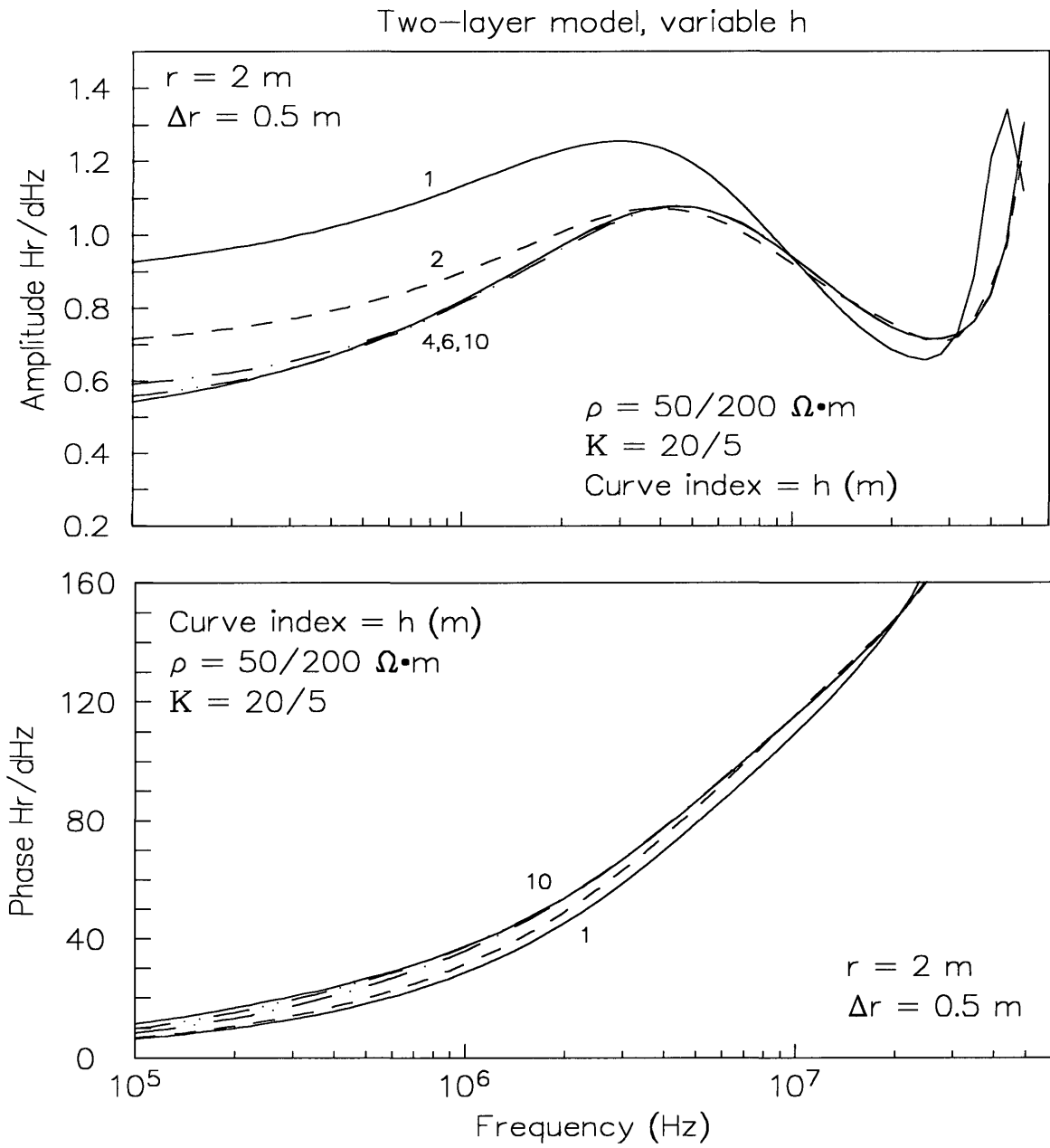


Figure 19. Calculated spatial gradient amplitude and phase for a two-layer model with a relatively low- $\rho$ , high-K top layer of variable thickness,  $h$  exceeds  $r$  (Model 5).

Summarizing Model 4 and Model 5, the polarization ellipse measurements are effective for resolving the top layer thickness only when  $h$  is less than the  $r$  spacing; as  $h$  exceeds  $0.5r$ , the two-layer model begins to behave as a half-space with the electrical parameters of the top layer. The spatial gradient measurements are effective for resolving thickness variations even when  $h$  is greater than  $r$  by a factor of two to five.

#### Effect of Bottom Layer Electrical Parameters

Models 6 through 9 (see Table 2) investigate the ability to detect variations of  $\rho_2$  or  $K_2$  in a two-layer earth. In each model, the top layer thickness  $h$  is fixed to either 1 m or 2 m, and the top layer electrical parameters are fixed to either  $\rho_1 = 200$  and  $K_1 = 5$ , or  $\rho_1 = 50$  and  $K_1 = 20$ . The parameters of the bottom layer are varied singly. The fixed parameter value is the complement of the top layer value, i.e., if  $\rho_1 = 200$ , then  $\rho_2 = 50$  and vice versa; if  $K_1 = 5$ , then  $K_2 = 20$ , etc.

Model 6: Resistive, Low-K Top Layer, Variable  $\rho_2$ . Calculated polarization ellipse data are shown in Figure 20; the spatial gradient data are shown in Figure 21. Note that  $h = 1$  m and therefore  $r = 4h$  for the polarization ellipse data, and  $r = 2h$  for the spatial gradient data. The polarization ellipse curves are most sensitive to  $\rho_2$  within a band of frequencies from about 100 kHz to 30 MHz, and the curve separations are largest for  $\rho_2 < \rho_1$ . The spatial gradient curves are most sensitive to  $\rho_2$  at frequencies below 3 MHz, and the curve separations are largest for  $\rho_2 > \rho_1$ .

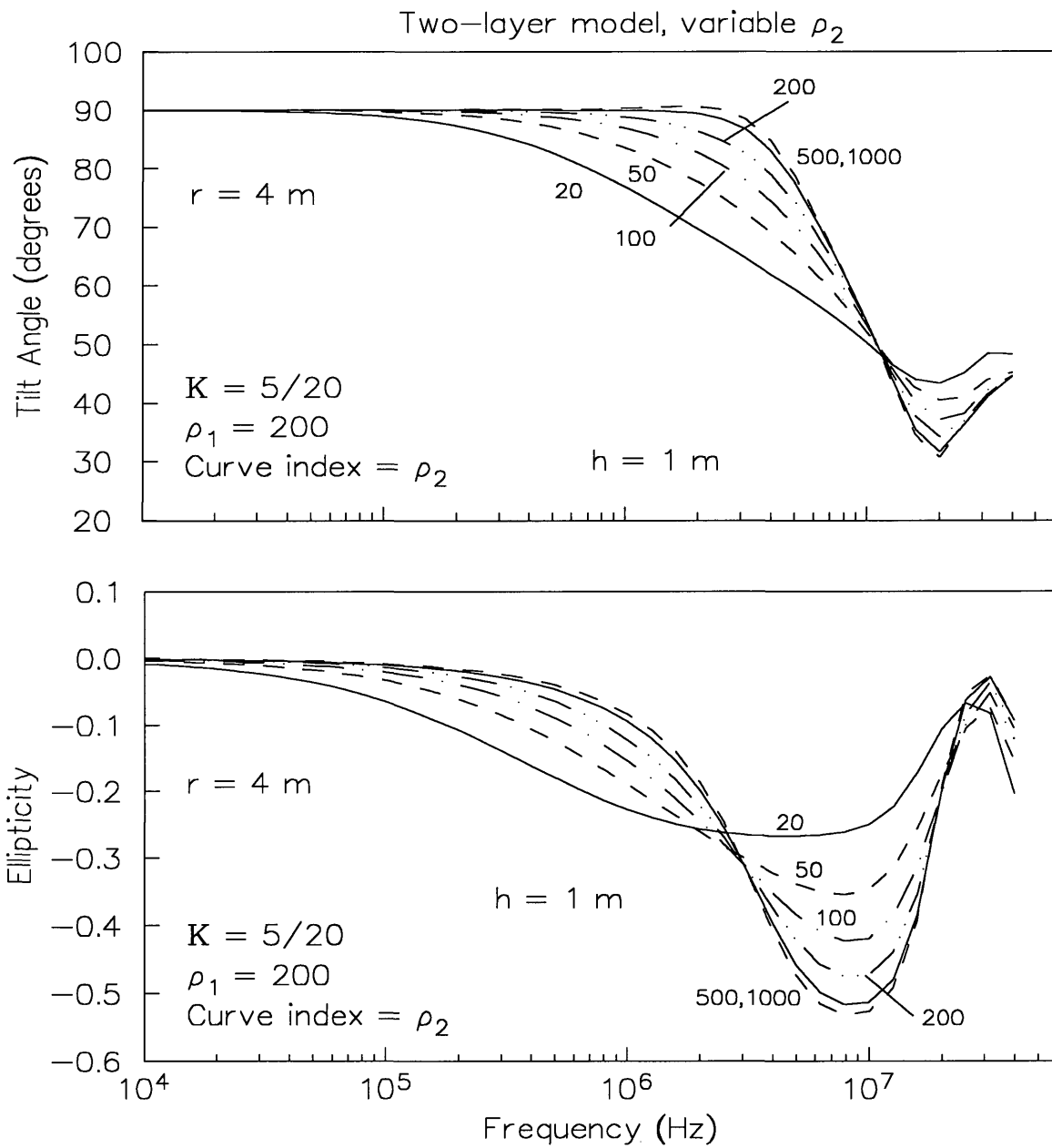


Figure 20. Calculated polarization ellipse tilt angle and ellipticity for a two-layer model with a relatively high- $\rho$ , low-K top layer and a variable  $\rho_2$ ,  $h=1$  m (Model 6).

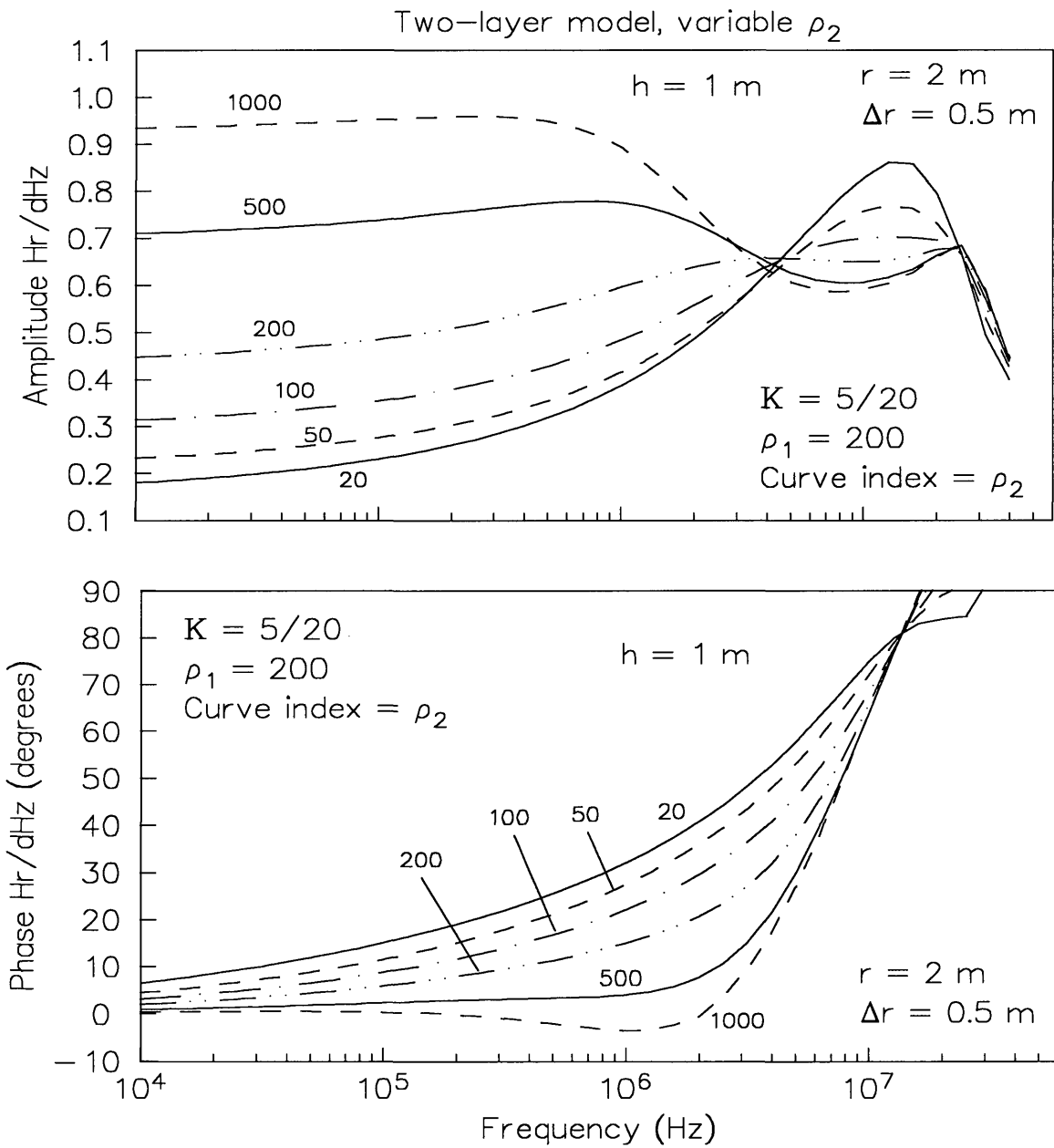


Figure 21. Calculated spatial gradient amplitude and phase for a two-layer model with a relatively high- $\rho$ , low-K top layer and a variable  $\rho_2$ ,  $h=1$  m (Model 6).

Overall, the spatial gradient data show the best ability to resolve  $\rho_2$ , despite the larger  $r$  spacing used for the polarization ellipse data. Although the polarization ellipse measurements have adequate resolution, especially near 3 MHz for the tilt angle and 10 MHz for the ellipticity, the curve separations for large  $\rho_2$  are very close to the resolution limit of the instrument. The spatial gradient curve separations below 3 MHz are at least two to three times larger than the instrument resolution limit for all values of  $\rho_2$ .

Additionally, the ability of polarization ellipse measurements to resolve  $\rho_2$  is substantially diminished if  $h$  is increased to 2 m. As seen in Figure 22, the largest curve separations for the tilt angle and the ellipticity are close to the resolution limit of the instrument. The spatial gradient curves for  $h = 2$  m are not shown, as they are virtually identical to those shown in Figure 21 for  $h = 1$  m. The only effect of the larger  $h$  is a 15% attenuation of the amplitude data; the spatial gradient curve separations for  $h = 2$  m are still at least twice the instrument resolution limit for all values of  $\rho_2$ .

Model 7: Conductive, High-K Top Layer, Variable  $\rho_2$ . In Figure 23, polarization ellipse data are calculated for  $\rho_1 = 50$  and  $h = 1$  m. When the top layer is relatively conductive, the curves are less sensitive to  $\rho_2$  than when the top layer is relatively resistive. The curve separations are much smaller than those for Model 6; for  $\rho_2 > 200$ , the separation of both the tilt angle and the ellipticity curves is less than the instrument resolution. Polarization ellipse data for  $h = 2$  m are not shown, since the curve separations are all less than the instrument resolution limit.

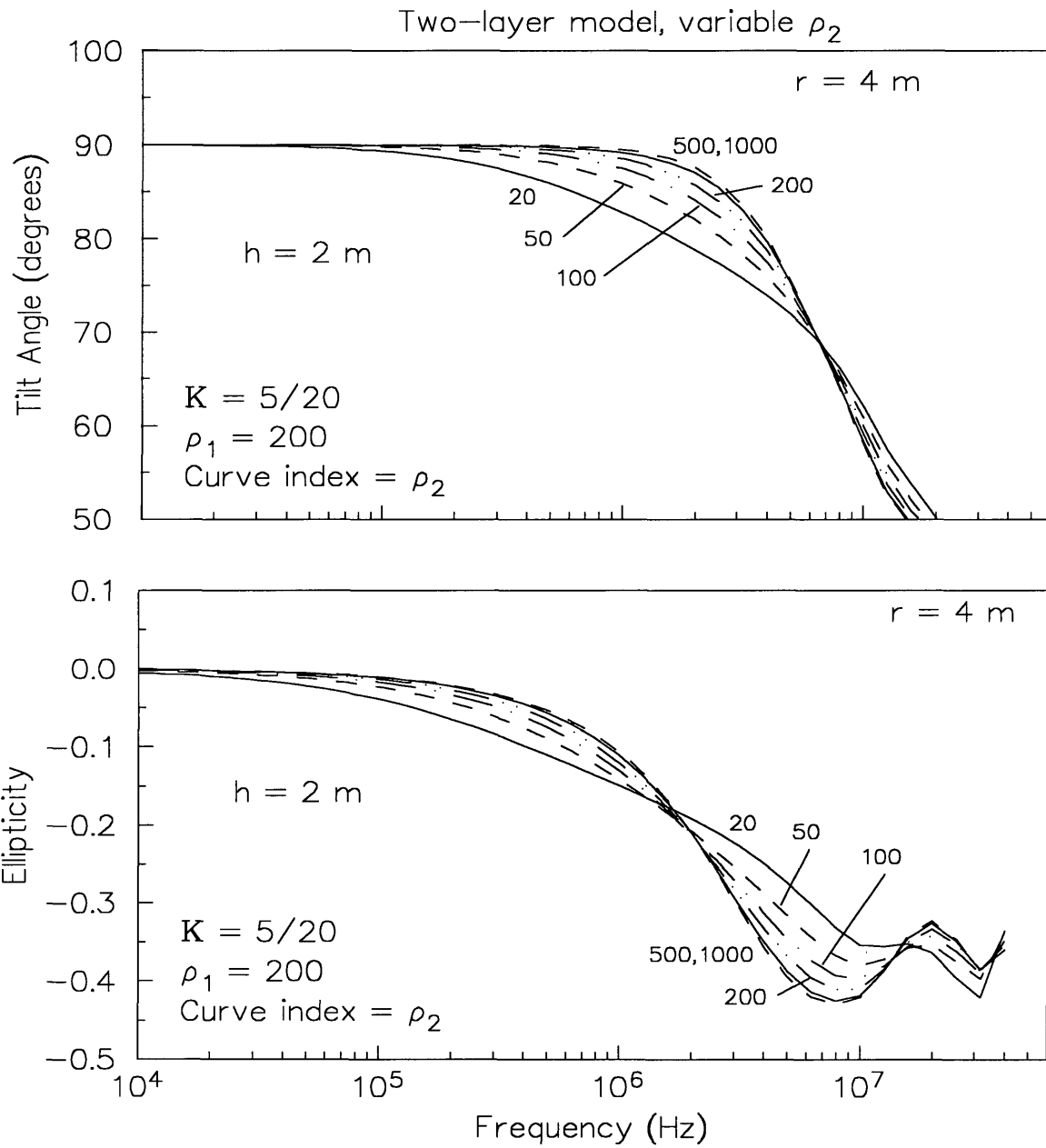


Figure 22. Calculated polarization ellipse tilt angle and ellipticity for a two-layer model with a relatively high- $\rho$ , low-K top layer and a variable  $\rho_2$ ,  $h=2$  m (Model 6).

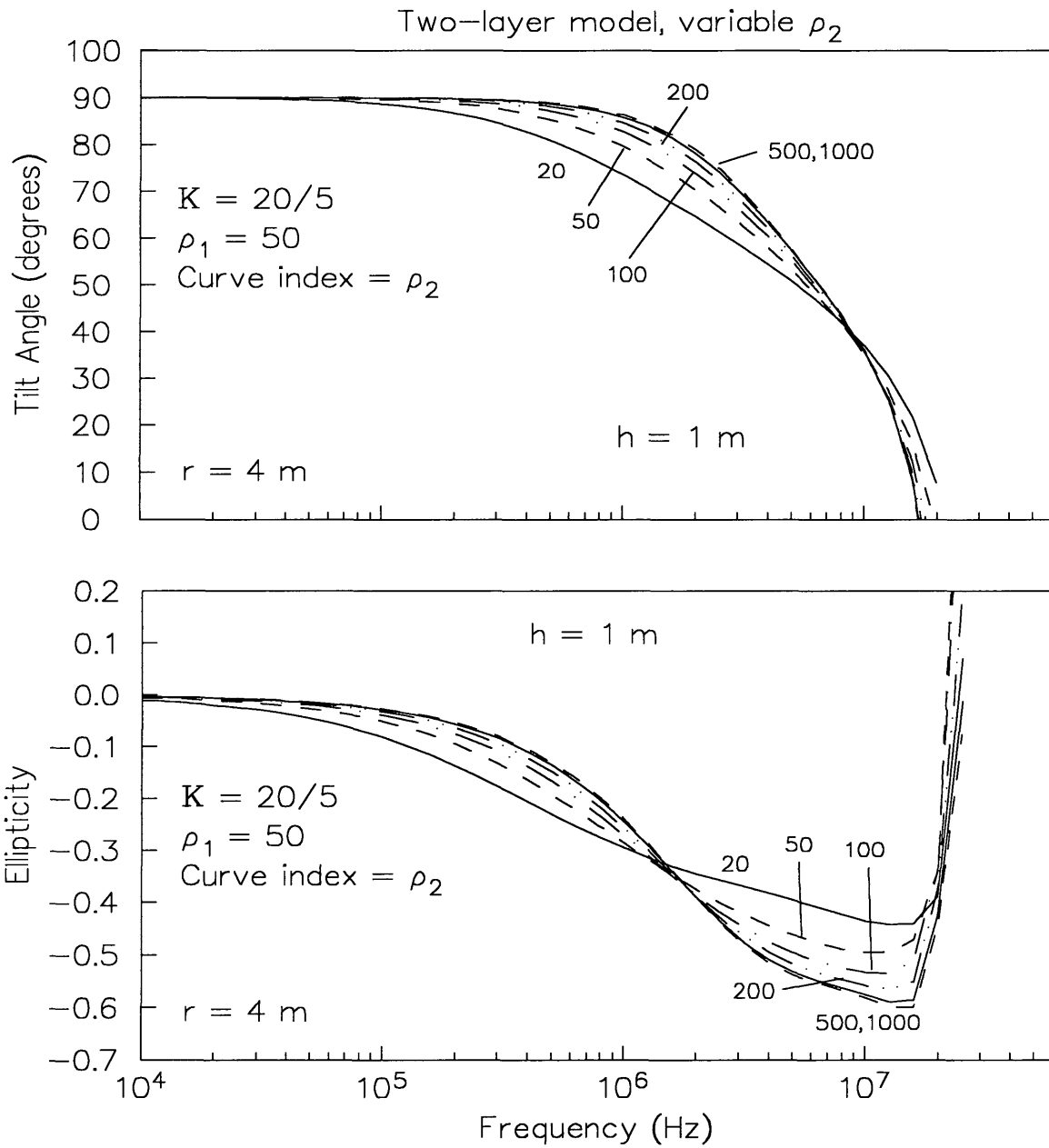


Figure 23. Calculated polarization ellipse tilt angle and ellipticity for a two-layer model with a relatively low- $\rho$ , high-K top layer and a variable  $\rho_2$ ,  $h=1 \text{ m}$  (Model 7).

The phase curves of the spatial gradient data in Figure 24 are also less sensitive to  $\rho_2$  than for Model 6. However, unlike the polarization ellipse data, the amplitude curves of the spatial gradient data are more sensitive to  $\rho_2$  than in Model 6. The amplitude sensitivity is reduced when  $h$  is increased to 2 m (Figure 25), but is still sufficient to resolve all the values of  $\rho_2$ .

Model 8: Resistive, Low-K Top Layer, Variable  $K_2$ . The spatial gradient data for Model 8 are virtually unaffected by changes in  $K_2$ , and are not shown. The polarization ellipse data for  $h = 1$  m are shown in Figure 26. The tilt angle curves become sensitive to  $K_2$  at frequencies above 3 MHz, while the ellipticity curves become sensitive to  $K_2$  above 1 MHz. The curve separations in the tilt data are about equal to the resolution limit of the instrument at frequencies near 20 MHz; the separation of the ellipticity curves is largest near 30 MHz, and is well within the instrument resolution limit for  $K_2 > 5$ . When  $h$  is increased to 2 m (Figure 27), the sensitivity to  $K_2$  effectively vanishes for both the tilt angle and the ellipticity data.

Model 9: Conductive, High-K Top Layer, Variable  $K_2$ . For this model, the polarization ellipse data, rather than the spatial gradient data, is unaffected by changes in  $K_2$ . Only the spatial gradient data are shown; in Figure 28,  $h = 1$  m, and in Figure 29,  $h = 2$  m. The phase curves cannot resolve  $K_2$ . However, the amplitude curves for  $h = 1$  m have a separation at frequencies near 3 MHz large enough to resolve  $K_2$ ,

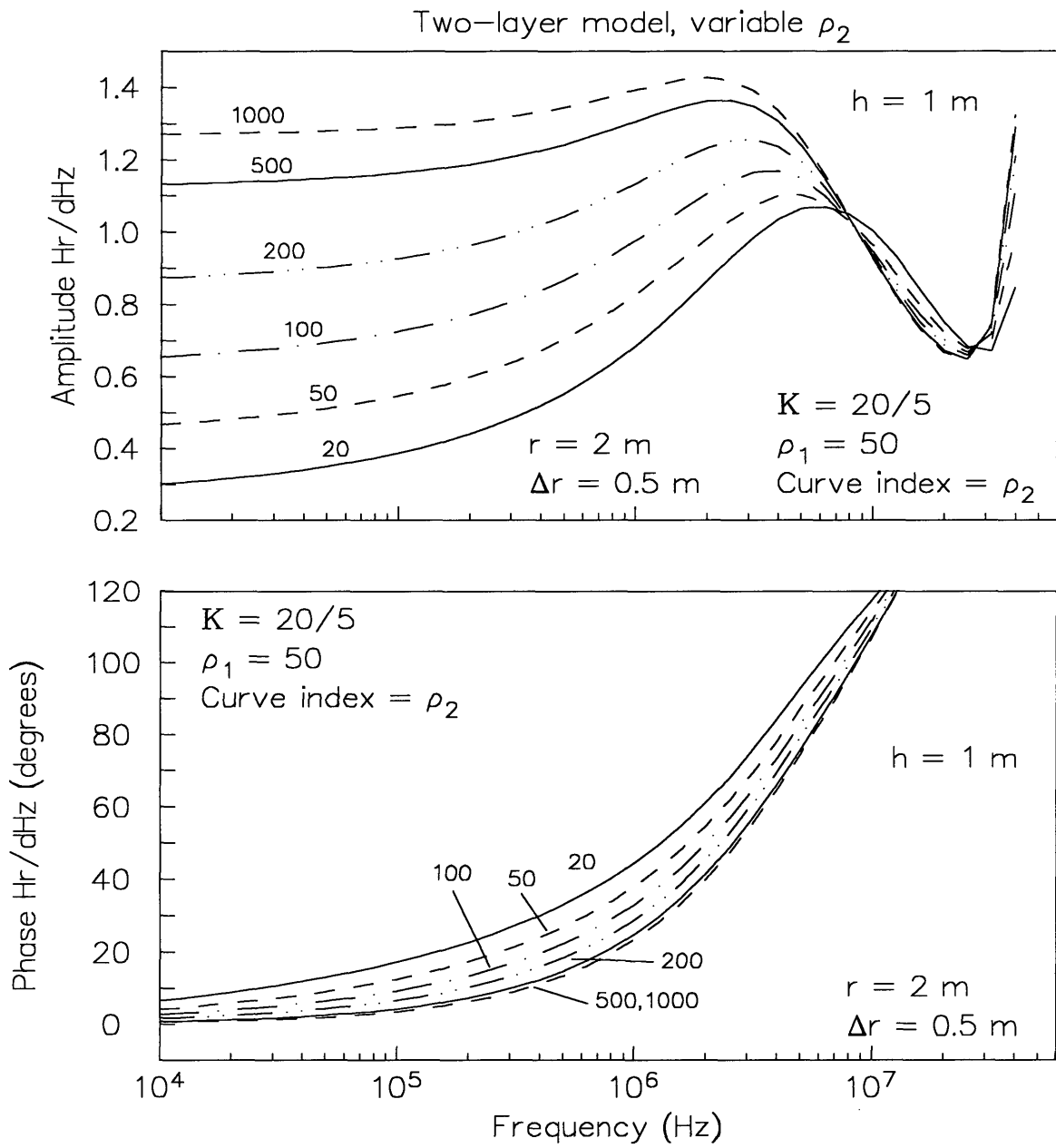


Figure 24. Calculated spatial gradient amplitude and phase for a two-layer model with a relatively low- $\rho$ , high-K top layer and a variable  $\rho_2$ ,  $h=1$  m (Model 7).

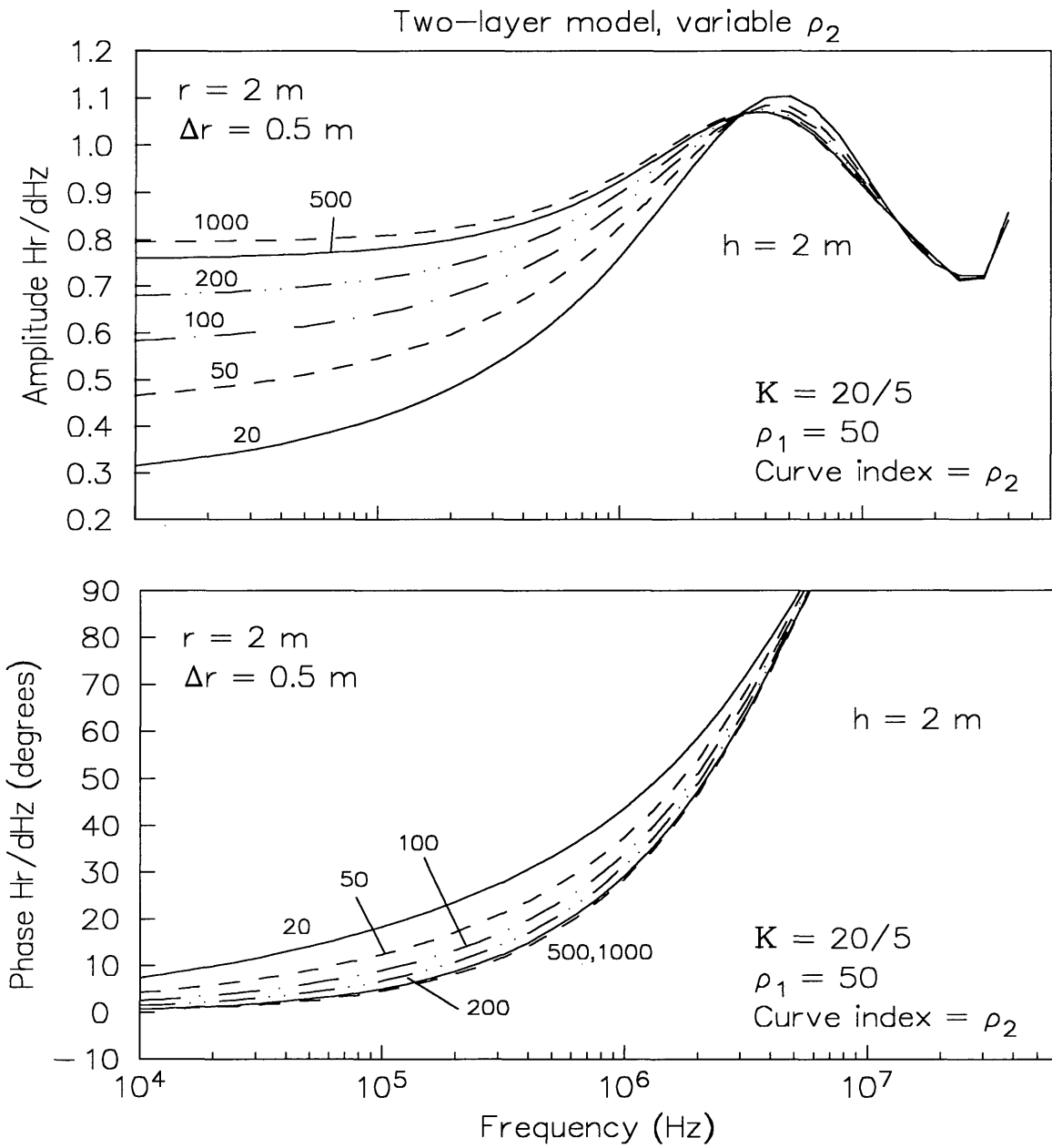


Figure 25. Calculated spatial gradient amplitude and phase for a two-layer model with a relatively low- $\rho$ , high-K top layer and a variable  $\rho_2$ ,  $h=2$  m (Model 7).

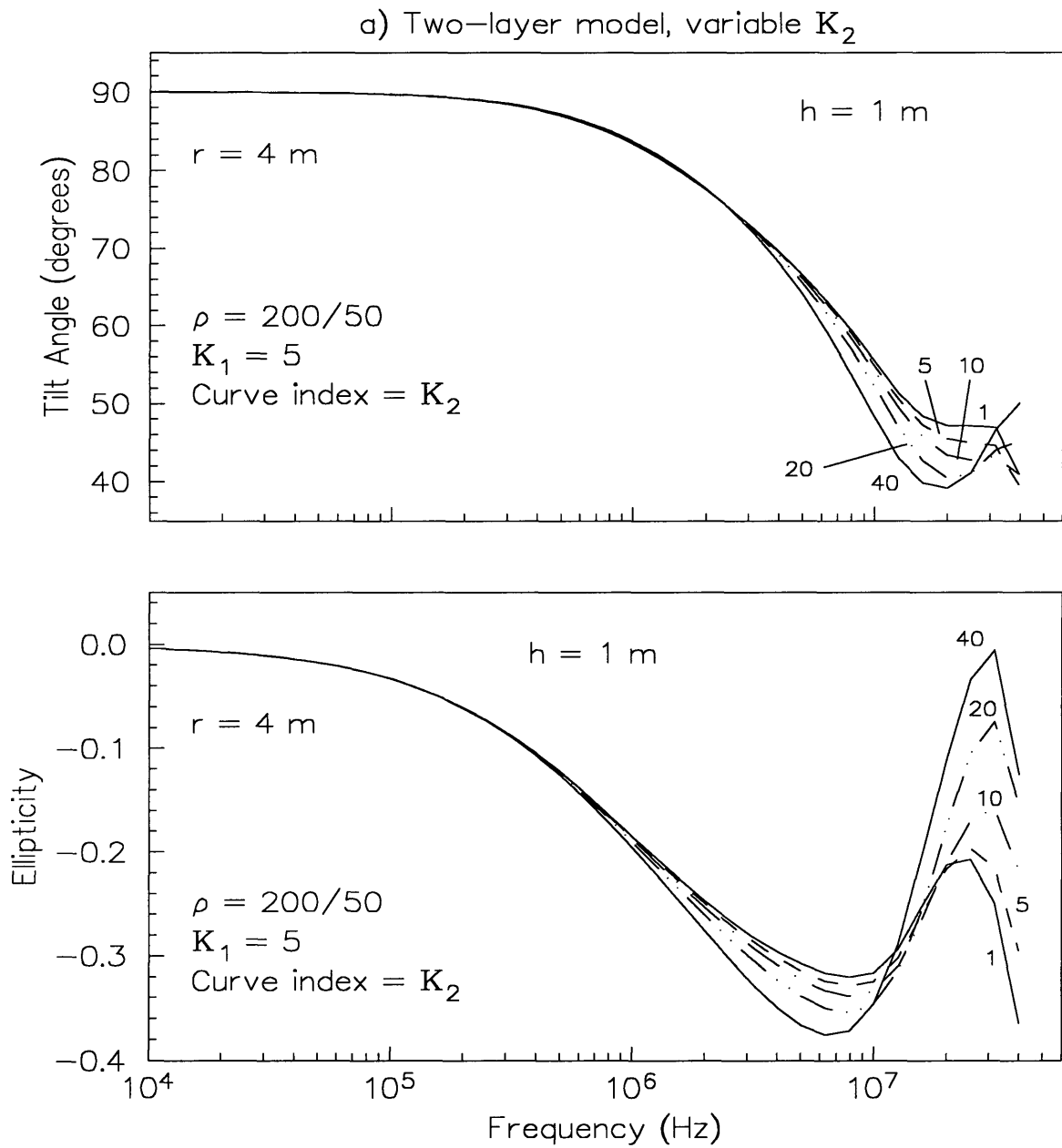


Figure 26. Calculated polarization ellipse tilt angle and ellipticity for a two-layer model with a relatively high- $\rho$ , low-K top layer and a variable  $K_2$ ,  $h=1$  m (Model 8).

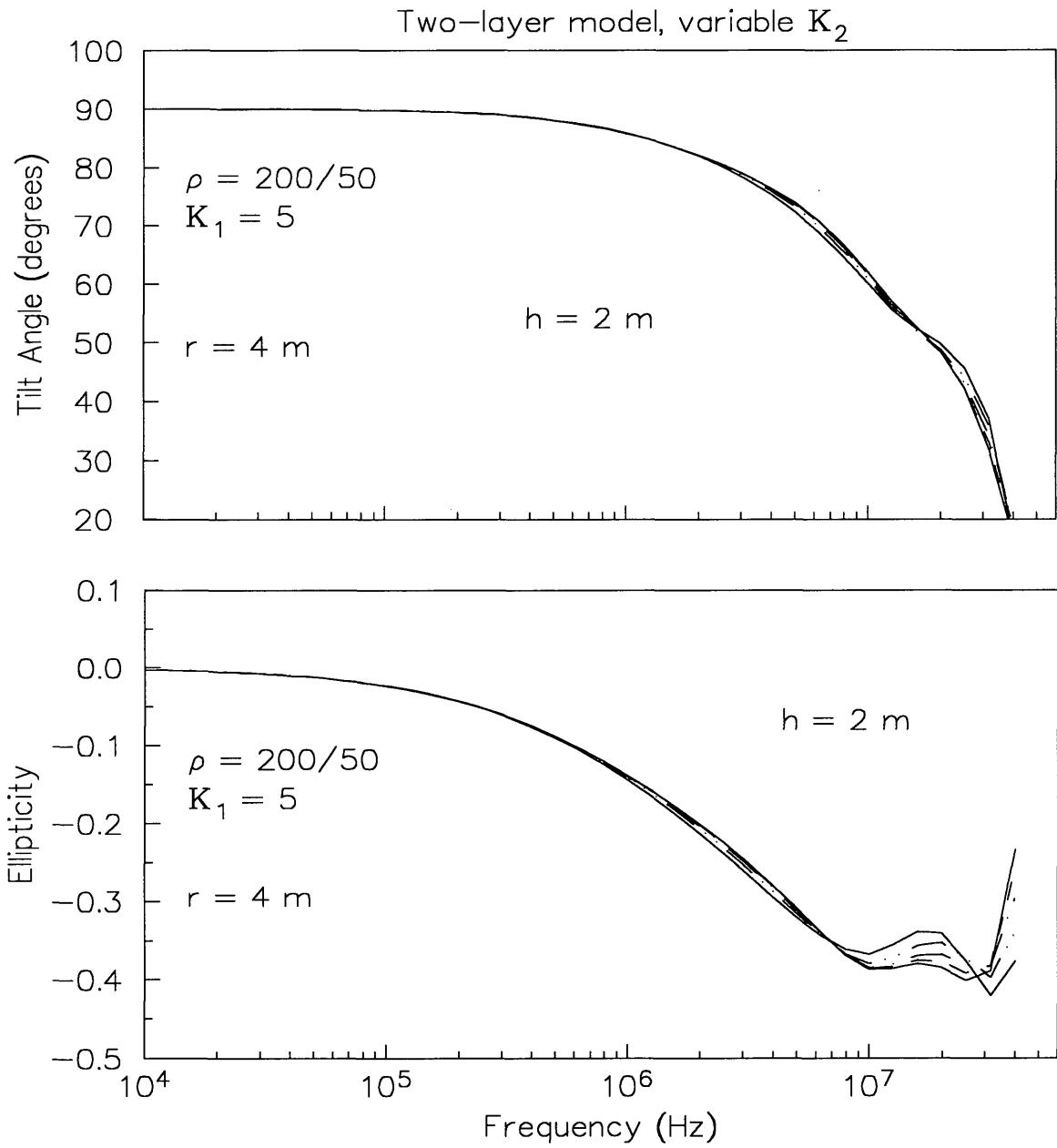


Figure 27. Calculated polarization ellipse tilt angle and ellipticity for a two-layer model with a relatively high- $\rho$ , low-K top layer and a variable  $K_2$ ,  $h=2$  m (Model 8).

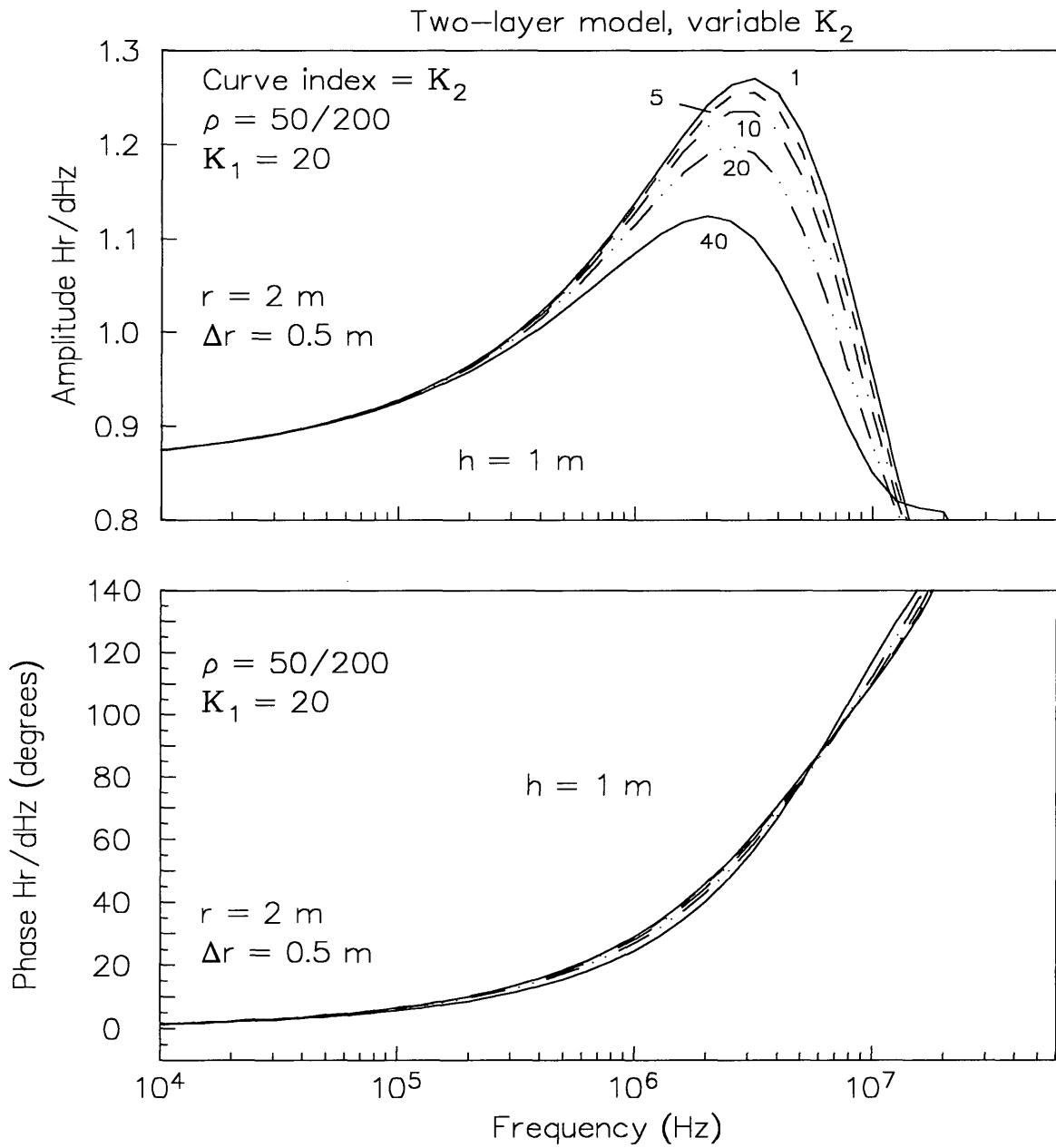


Figure 28. Calculated spatial gradient amplitude and phase for a two-layer model with a relatively low- $\rho$ , high-K top layer and a variable  $K_2$ ,  $h=1$  m (Model 9).

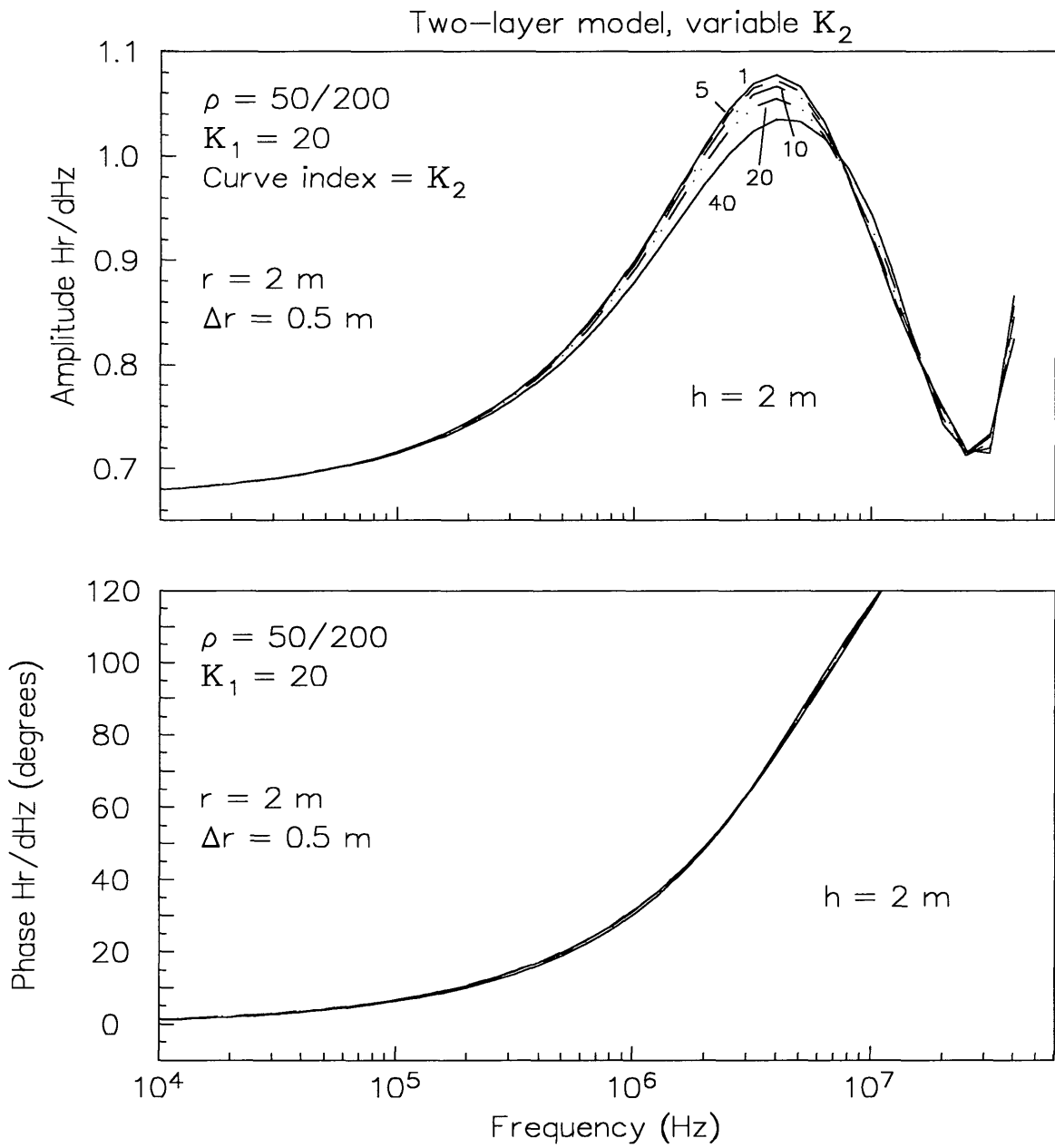


Figure 29. Calculated spatial gradient amplitude and phase for a two-layer model with a relatively low- $\rho$ , high- $K$  top layer and a variable  $K_2$ ,  $h=2 \text{ m}$  (Model 9).

especially values larger than 5. When  $h$  is increased to 2 m, the amplitude curve separations are barely large enough to resolve  $K_2 > 10$ .

### Three-Layer Models: Thin Layer Detection

The remaining models in this chapter examine the sensitivity of high-frequency measurements to the middle layer of a three-layer earth. In a real-world survey, this represents a goal such as detecting a thin layer of pollutant floating on the water table, or mapping a buried lens.

### Models 10 Through 15: Effect of Middle Layer Thickness

The physical and practical importance of dielectric properties is clearly illustrated by a series of models that demonstrate the ability of high-frequency sounding to resolve the thickness of a shallow thin layer. Six different types of three-layer model are used to examine the effects of resistivity contrasts and dielectric contrasts between layers. Because of the large number of parameter combinations, the model data are not presented as "raw" observed values. Instead, they are shown as the arithmetic difference between the response of a half-space and that of a three-layer model created by adding a thin buried layer; i.e., they show the anomalous response due to the presence of the thin layer. In this manner, the results of the six models can be summarized by comparing their maximum anomalous responses. Table 2 lists the three-layer model parameters; the half-space model parameters are equal to the  $\rho_1$  and  $K_1$  values, or the  $\rho_3$  and  $K_3$  values.

Polarization Ellipse Measurements. Consider a case where displacement currents are ignored, i.e.,  $K = 0$  for all media. Figure 30 shows the anomalous response of the

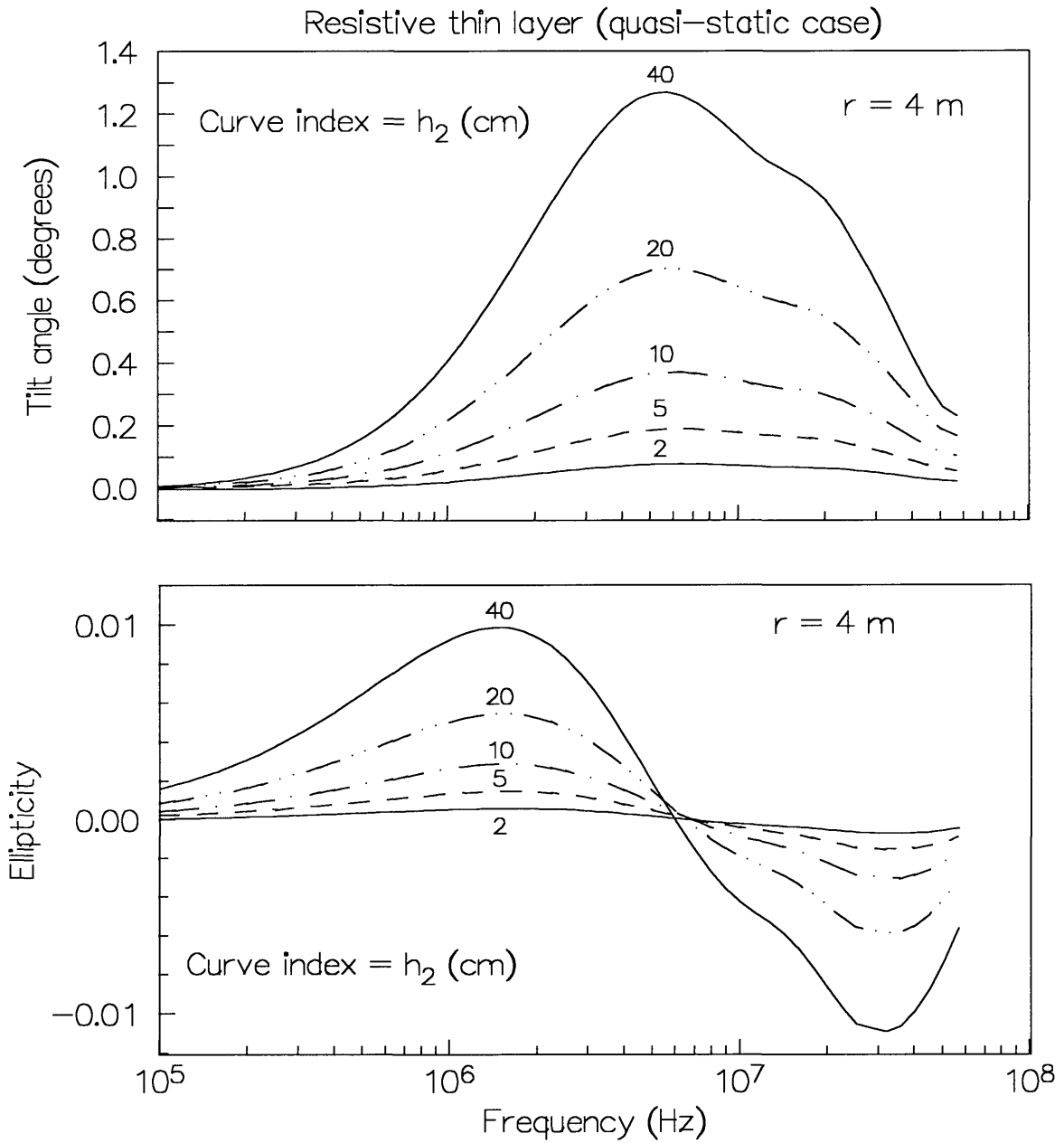


Figure 30. Calculated polarization ellipse tilt angle and ellipticity anomalies caused by adding a thin resistive layer to a half-space to make a three-layer model. Displacement currents are neglected (Model 10).

polarization ellipse for Model 10, where the thin layer  $\rho$  is twice that of the host material. The maximum tilt angle anomaly occurs at frequencies near 5 MHz and is about 1.3 degrees for  $h_2 = 40$  cm; the ellipticity anomaly has two maxima near 1.5 MHz and 30 MHz, with values less than 1.1 percent for  $h_2 = 40$  cm. Very accurate measurements would be required to detect the 40 cm layer; detection of thinner layers or resolution of small variations in  $h$  would be impossible with the present instrument.

Next, consider the case where displacement currents are included. Figure 31 shows the response for Model 11, where  $K = 10$  for all layers. The response for frequencies above 10 MHz is dramatically larger than that for Model 10. In Model 11, the maximum anomalies for  $h_2 = 2$  cm are comparable in size to those for  $h_2 = 40$  cm in Model 10, while the maximum anomalies for  $h_2 = 40$  cm in Model 11 are about 21 degrees of tilt and 29 percent of ellipticity. Even though there is no  $K$  contrast between layers, the presence of displacement currents makes the anomalous response large enough to detect layers only a few centimeters thick, or to resolve small changes in  $h$ .

In Figure 32, the absolute value of the maximum anomaly is plotted against  $h_2$  for Models 10 through 15. As discussed above, Models 10 and 11 show the effect of including displacement currents for the case of a resistive layer. Models 12 and 13 compare the effect of displacement currents for the case of a conductive layer. Again, regardless of  $h_2$ , the anomaly is virtually undetectable for quasi-static conditions (Model 12). However, the presence of displacement currents amplifies the anomaly by more than an order of magnitude (Model 13).

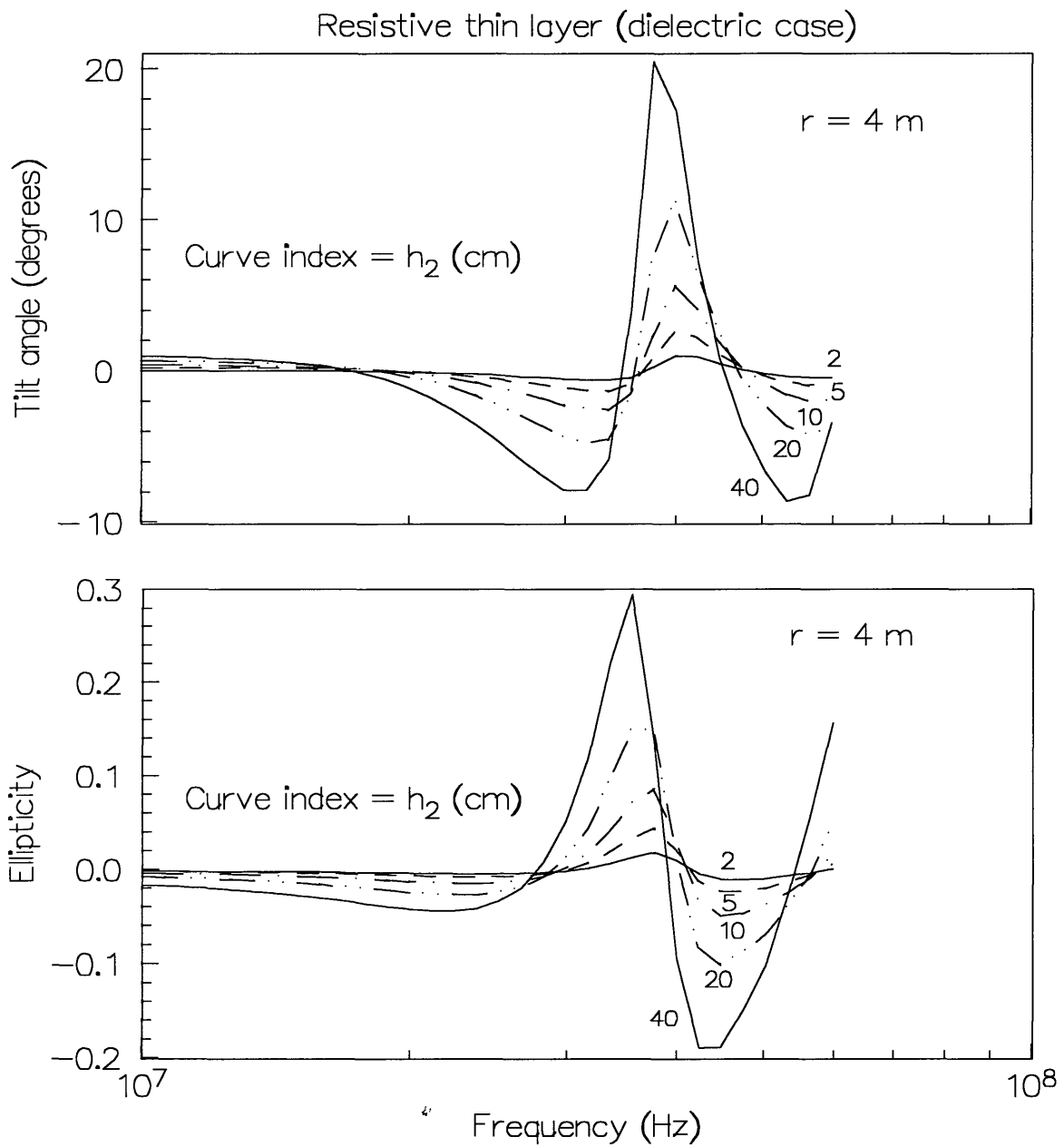


Figure 31. Calculated polarization ellipse tilt angle and ellipticity anomalies caused by adding a thin resistive layer to a half-space to make a three-layer model. Displacement currents are included (Model 11).

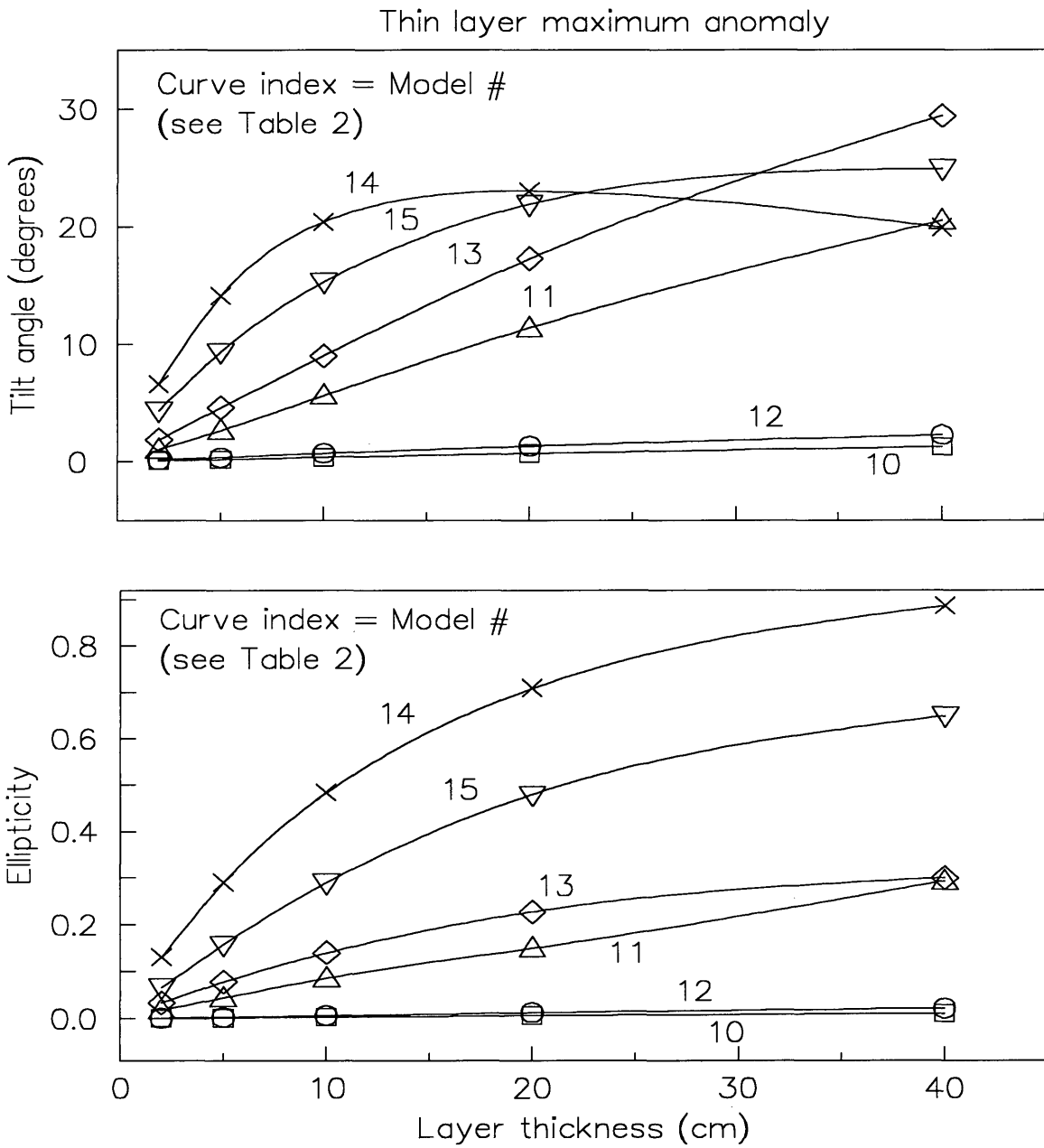


Figure 32. A summary of the maximum anomalous response of the polarization ellipse tilt angle and ellipticity for Models 10 through 15.

In models 10 through 13, there is only a  $\rho$  contrast between earth media. Models 14 and 15 show cases where there is only a K contrast. Even when  $h_2 = 2$  cm there is a substantial anomaly: 4.4 to 6.6 degrees of tilt and 6.6 to 13.1 percent ellipticity, respectively, for a layer with K higher (Model 14) or lower (Model 15) than that of the host. It must be noted that the maximum anomalies for these examples mostly occur at frequencies between 30 and 50 MHz, which is above the operating range of the present instrument. However, the anomalous responses within the instrument frequency range are for the most part still within the instrument resolution limit.

Spatial Gradient Measurements. For five of the six models, the sensitivity of the calculated spatial gradient data to  $h_2$  is not large enough for the instrument to resolve small changes. The largest anomalous response is for Model 15, as shown in Figure 33. The anomalous amplitude response is within the instrument resolution limit for  $h_2 > 5$  cm; The phase response is within limits for  $h_2 > 10$  cm.

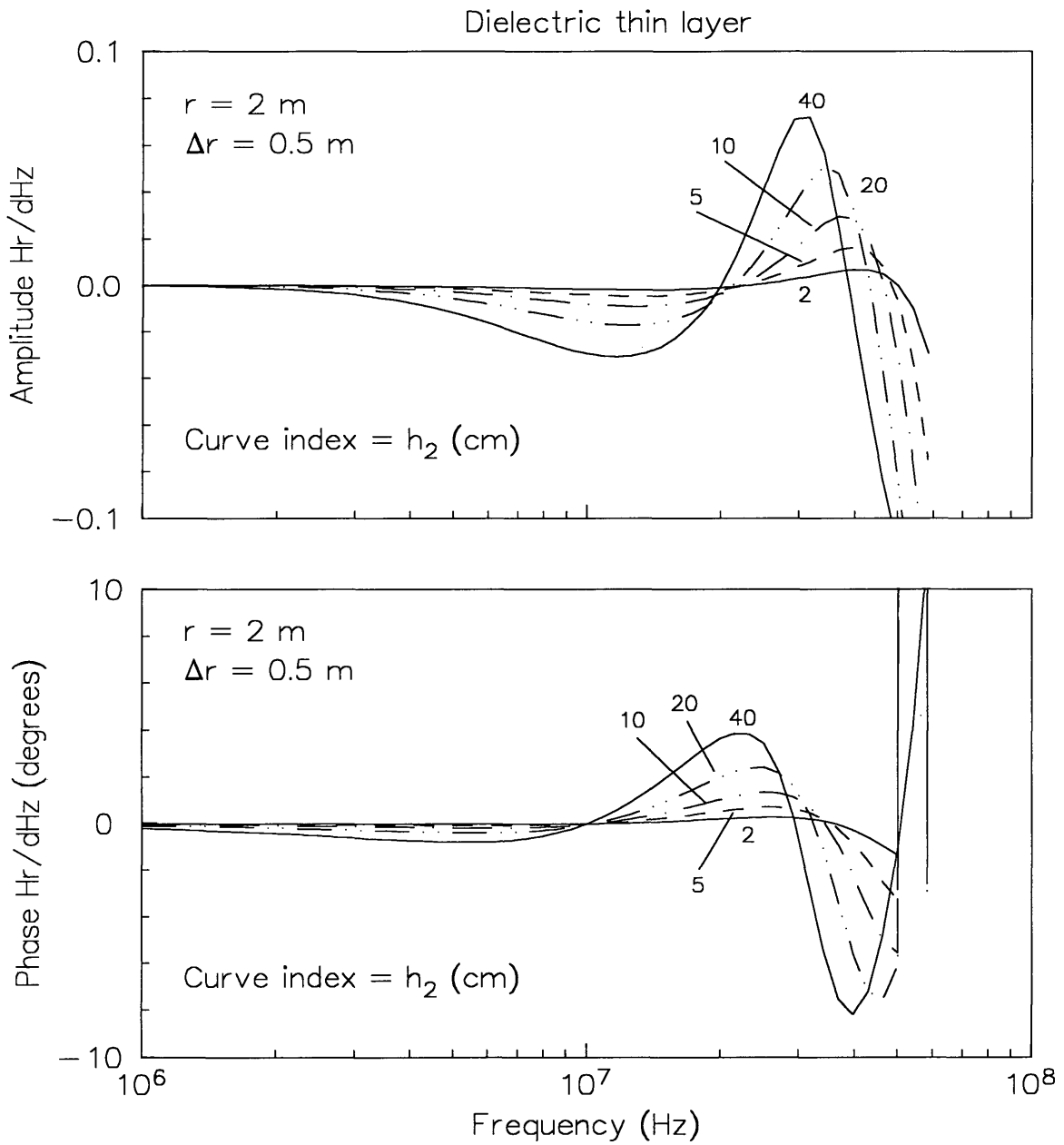


Figure 33. Calculated spatial gradient amplitude and phase anomalies caused by adding a thin dielectric layer to a half-space to make a three-layer model (Model 15).

### Effect of Middle Layer Electrical Parameters

The last two models of this chapter investigate the ability to determine variations of the electrical parameters of a thin shallow layer. The top layer of the models is 1 m thick, and the middle layer is assigned a fairly small thickness,  $h_2 = 20$  cm. The top and bottom layers have  $\rho = 100$  and  $K = 10$ . The electrical parameters of the middle layer are varied singly, with the non-varying parameter fixed to the value of the top and bottom layers. Thus, the parameter which is varied represents the only contrast between layers in the model.

Model 16: Variable  $\rho_2$ . Despite the small thickness of the middle layer, variations of its resistivity are resolvable to some degree, especially when it is less resistive than the host material. The calculated polarization ellipse data shown in Figure 34 is most sensitive to  $\rho_2$  at frequencies between 10 MHz and 30 MHz, where the effect of increasing  $\rho_2$  is to decrease both the ellipticity and the tilt angle. Within this range, the tilt angle and the ellipticity curve separations are within the instrument resolution limit for  $\rho_2 < 200$ , but are less than the limit for  $\rho_2 > 200$ .

The calculated spatial gradient data shown in Figure 35 is most sensitive for frequencies below 10 MHz, where the effect of increasing  $\rho_2$  is to increase the amplitude and decrease the phase. The amplitude curves have about the same degree of sensitivity as the polarization ellipse ellipticity; i.e., the curves are resolvable for  $\rho_2 < 200$ , but not for  $\rho_2 > 200$ . The phase data is virtually unaffected by changes in  $\rho_2$ .

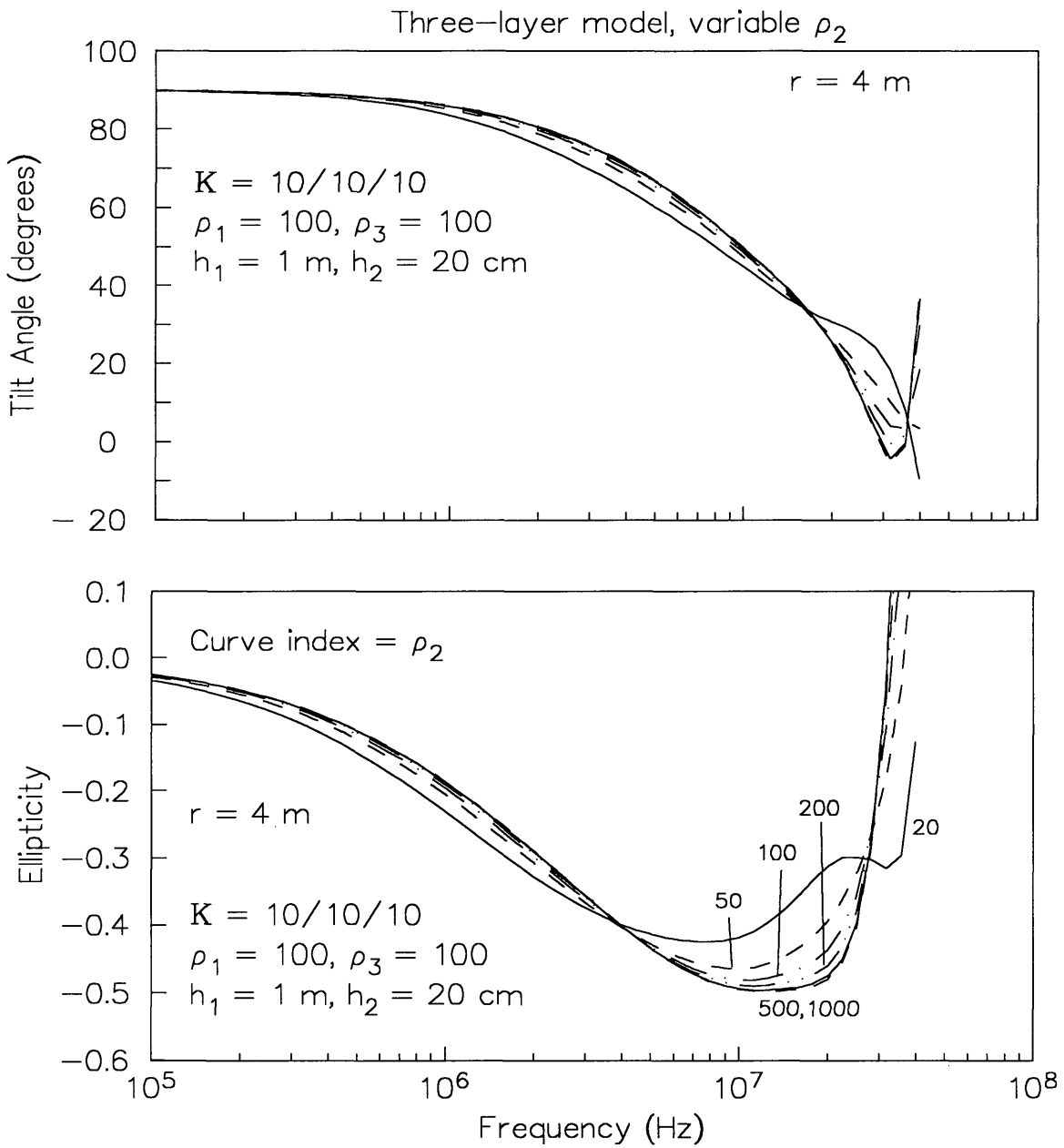


Figure 34. Calculated polarization ellipse tilt angle and ellipticity for a three-layer model with a variable  $\rho_2$  (Model 16).

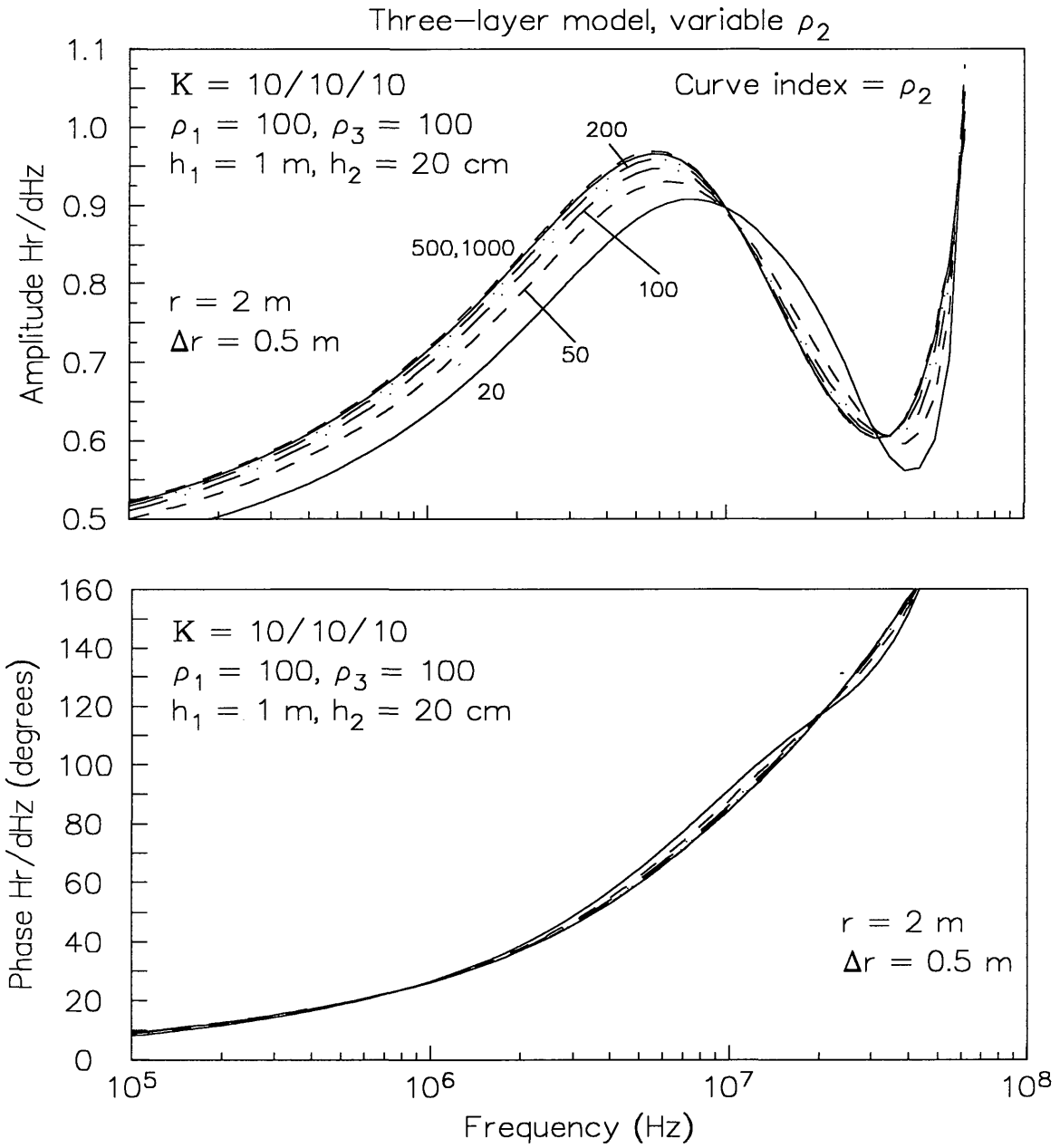


Figure 35. Calculated spatial gradient amplitude and phase for a three-layer model with a variable  $\rho_2$  (Model 16).

Model 17: Variable  $K_2$ . The polarization ellipse data is much more sensitive to variations of  $K_2$  than to the  $\rho_2$  variations of Model 16. In Figure 36, the tilt angle curve separations are within the resolution limit for all values of  $K_2$  when the frequency exceeds 30 MHz. The ellipticity curve separations are within the limit for all  $K_2$  at frequencies above 20 MHz. Both the tilt angle and the ellipticity curves show oscillatory behavior for  $K_2 > 10$ .

The spatial gradient amplitude data (Figure 37) are slightly more sensitive to variations of  $K_2$  than to variations of  $\rho_2$ . For frequencies between 20 MHz and 40 MHz, the amplitude curve separations are well within the resolution limit for  $K_2 > 10$ ; the separations for  $K_2 < 10$  are much smaller, but are just within the resolution limit. Oscillatory behavior is seen in the curves when  $K$  exceeds 20. As with Model 16, the phase curves are effectively insensitive to  $K_2$ .

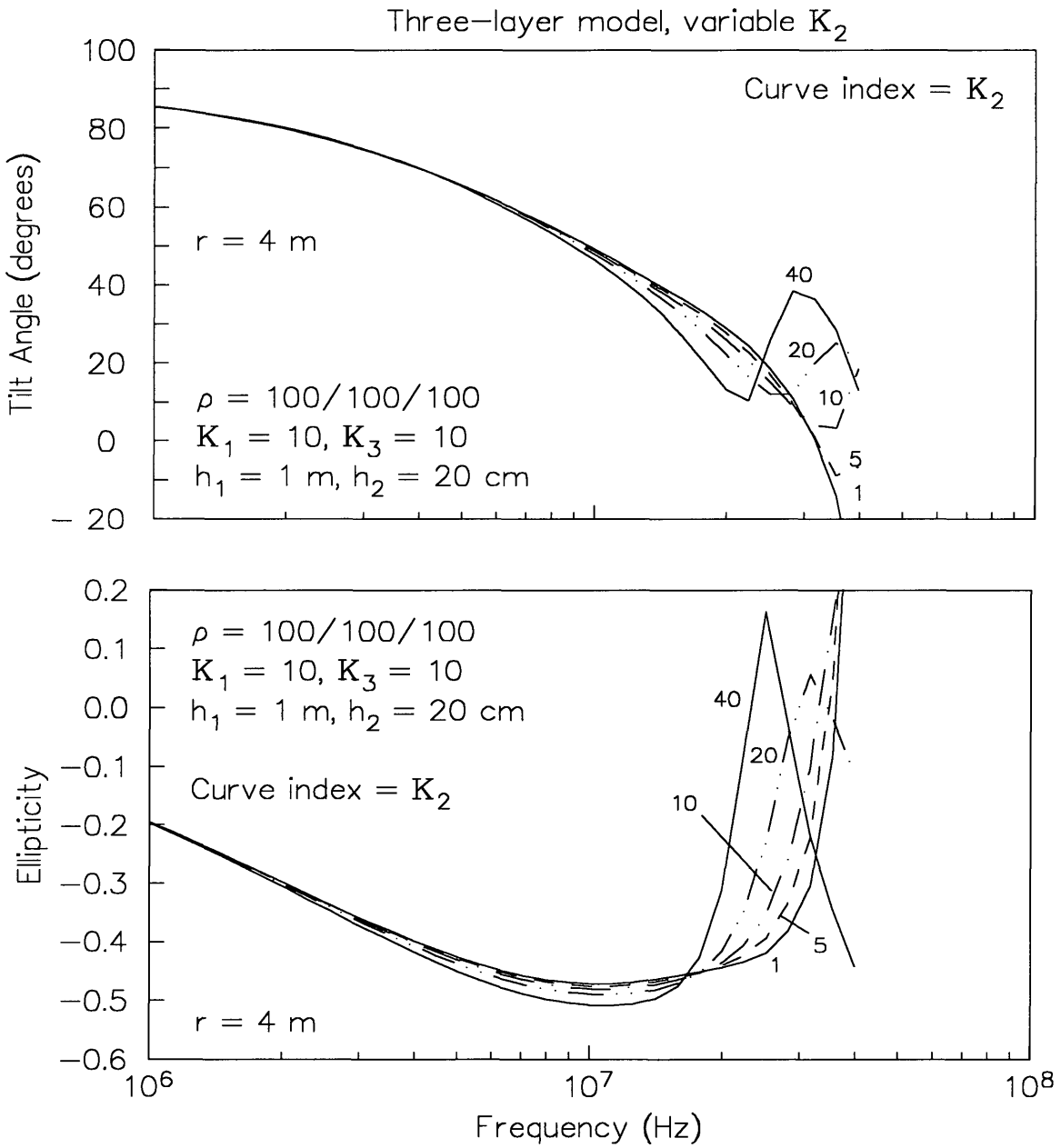


Figure 36. Calculated polarization ellipse tilt angle and ellipticity for a three-layer model with a variable  $K_2$  (Model 17).

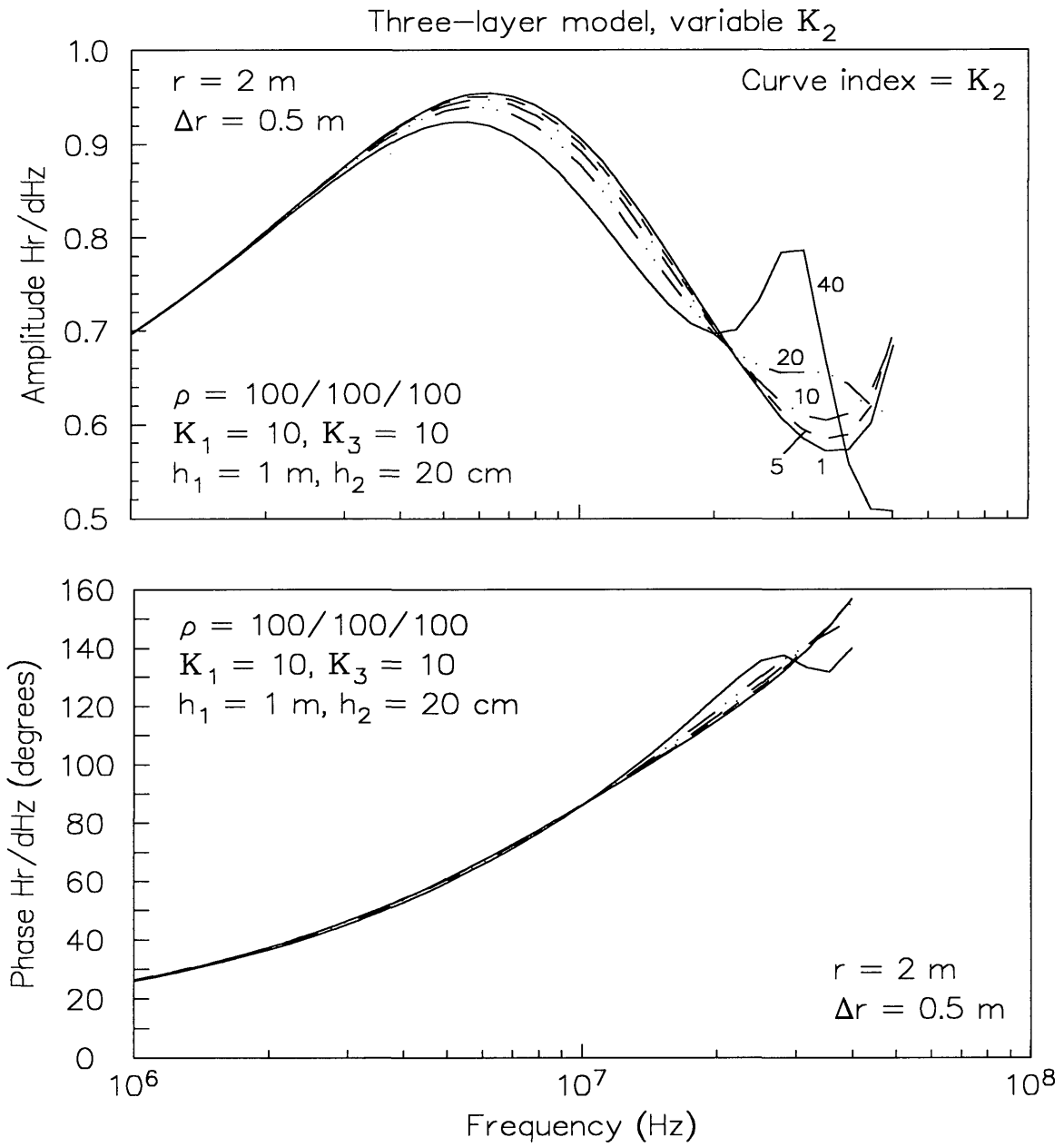


Figure 37. Calculated spatial gradient amplitude and phase for a three-layer model with a variable  $K_2$  (Model 17).

## INSTRUMENTATION

The following sections describe the design of the prototype instrument, some of the instrumental problems encountered and their (partial) solution, and the method of data collection. The shortcomings of the prototype and some desired improvements are discussed and summarized in the conclusions and recommendations chapter. A report is available (*Grover and Stewart, 1990*) which contains a complete description of the electronics of the "first generation" instrument, including detailed circuit diagrams.

The design requirements for a prototype sounder were established by using a normalized  $H_z$  field forward computer program. Initial model studies by *Anderson et al.* (1990), concluded that frequencies from about 100 kHz to 50 MHz and  $r$  spacings up to about 10 m are well suited for resolving geoelectric parameters of the upper few meters of the earth. It was also observed that the choice of  $r$  strongly affects resolving power; thus, the capability to measure at multiple spacings is important.

### System Description

The prototype sounder has a frequency range of 300 kHz to 30 MHz, and  $r$  spacings varying between 0.5 m and 5 m (*Grover and Stewart, 1990*). The system block diagram is shown in Figure 38. The transmitter drives a single-turn horizontal loop of radius 0.1524 m; at frequencies below 3 MHz, the single-turn loop is replaced with a

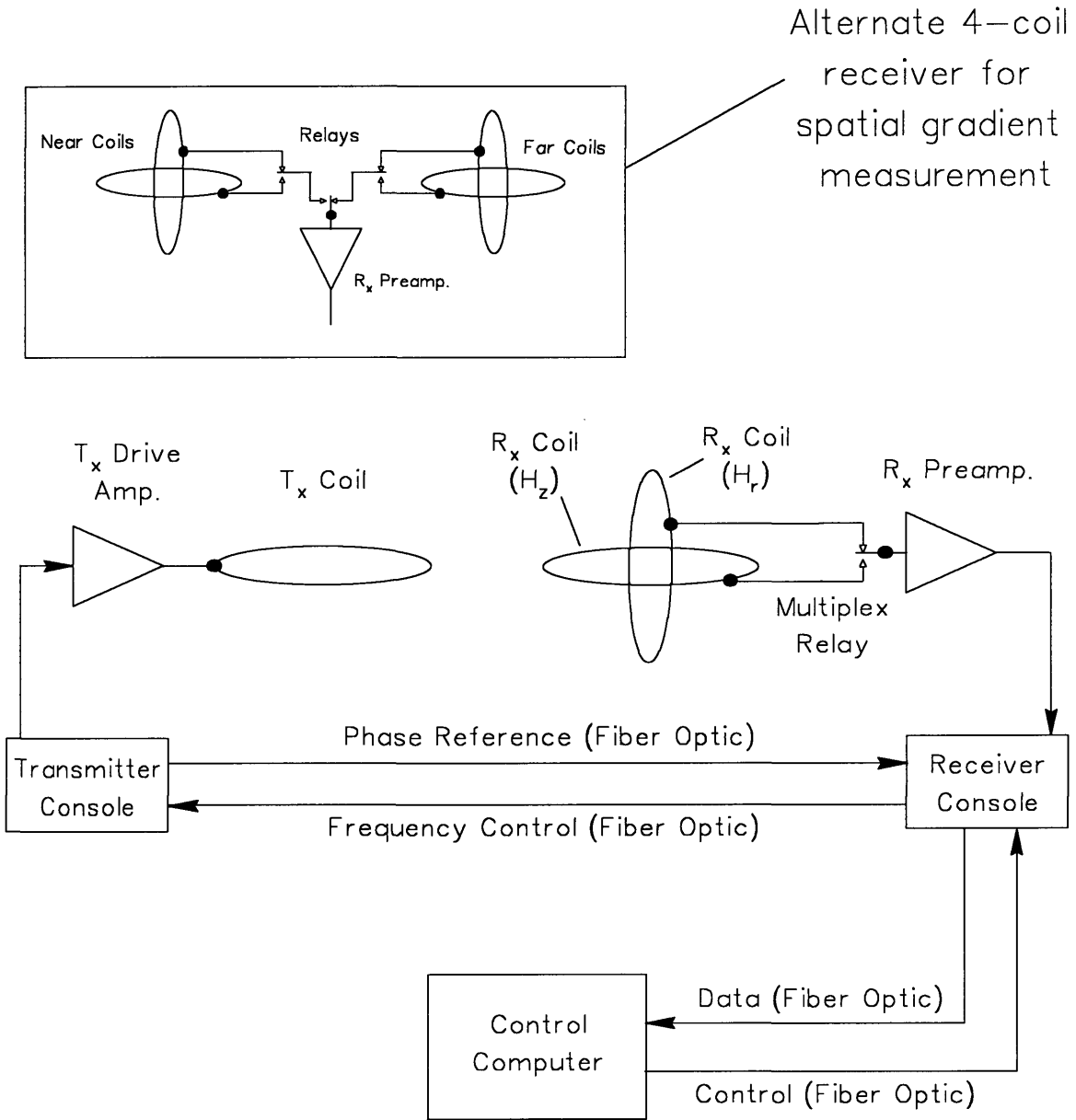


Figure 38. Block diagram of high-frequency sounder.

three-turn loop to increase signal strength. The receiver has two three-turn, 0.1524 m radius loops at right angles to detect the vertical and radial fields; both receiver loops are multiplexed through a single set of electronics by a relay. Data acquisition is either manual or computer controlled, using frequency increments as small as 100 kHz. To reduce coupling problems, fiber optic cables are used instead of metallic cables for phase reference and frequency control links between the transmitter and receiver consoles, and for the computer link. The fiber optic computer cables are 15 m long, to allow a large separation between the instrument and potential EM noise sources in the computer.

The inset of Figure 38 shows a receiver modification which allows sequential measurement at two different  $r$  spacings by connecting an additional set of receiver loops and multiplexing relays to the preamplifier input. This configuration, dubbed "SPATGRAD", is used for measuring spatial gradients of the fields. Since this is a first-generation experimental modification to the original sounder, unresolved design inadequacies limit the two  $r$  spacings to 1.5 and 2 m.

### Instrument Problems

The receiver measures the un-normalized in-phase and quadrature components of the total (primary plus secondary) vertical and secondary radial magnetic fields, where the primary field is the free-space field of the source, and the secondary field is caused by induced currents in the earth. The relation of observed field to the primary, secondary, and total field components of the vertical ( $H_z$ ) field is illustrated by Figure 39. Ideally, the primary field produces only an inphase signal in the receiver; in reality, the system electronics contribute a phase shift which rotates the observed primary field vector away from the inphase axis. This system phase reference must be known to obtain the "true" inphase and quadrature components of the total field.

At present, it is impractical to measure normalized components (*Stewart et al.*, 1990), because this requires exact knowledge of the primary field phase and amplitude, and long-term stability of the instrument gain and phase shift. A mathematical calculation of the primary field coupling between two loops is possible, but the "real world" coupling is complicated at high frequencies by antenna effects in connecting cables and phase shifts in the amplifiers and fiber optic cables. Direct measurement of the primary field would require suspending the instrument high in the air to reduce reflected energy from the earth's surface. Additionally, the instrument gain and phase shift are very sensitive to temperature; calculated or measured primary field values are useless without monitoring the instrument temperature and having precise knowledge of the temperature dependence for each component.

$H_z$  field components

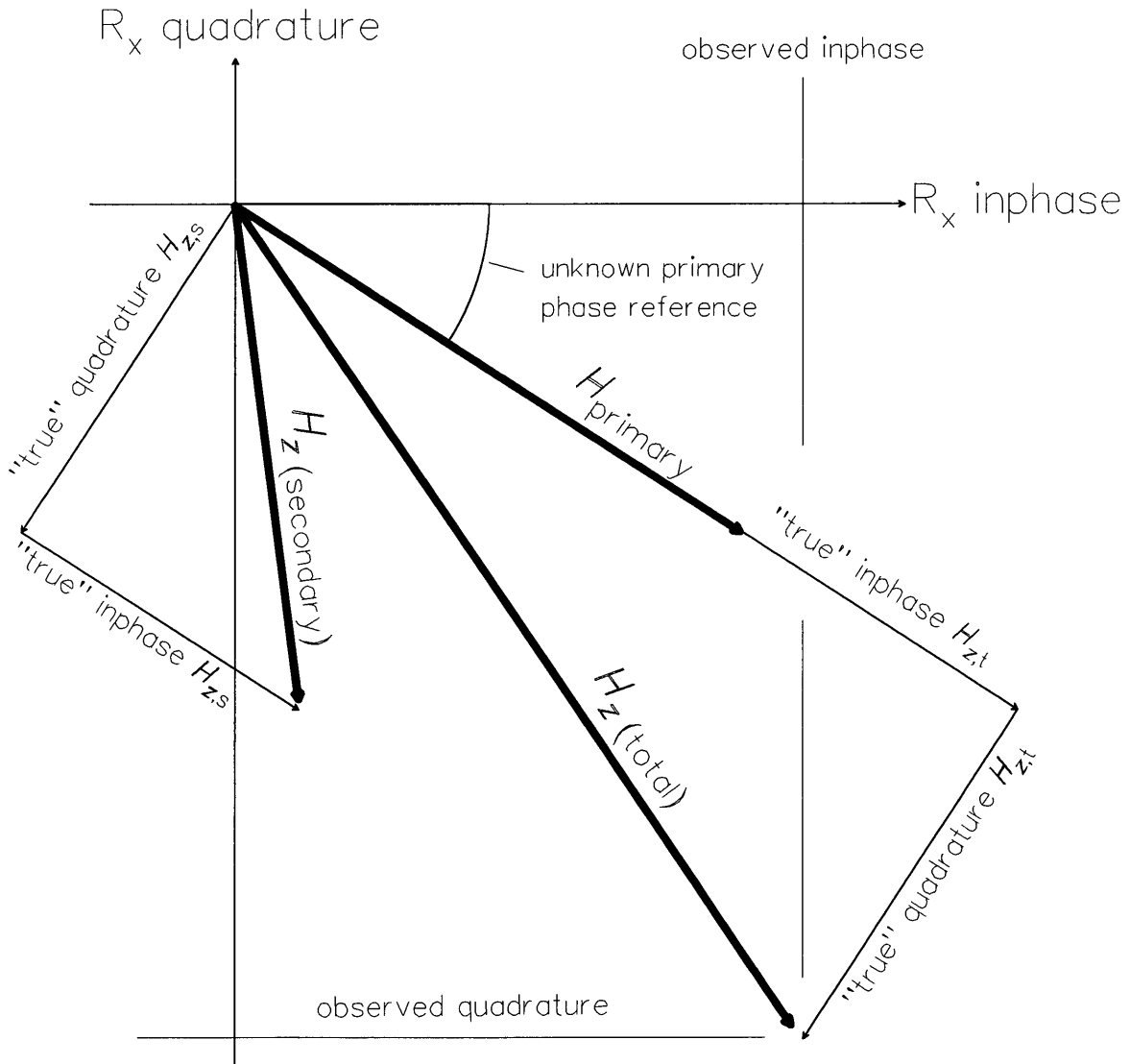


Figure 39. Illustration of the components of the total  $H_z$  field.

Electronic solutions to the above problems are possible but not reliable for routine instrument use. A practical solution is to use in-phase and quadrature measurements to calculate quantities based on field ratios, such as the parameters of the magnetic field polarization ellipse (*Smith and Ward, 1974; Frischknecht et al., 1991*). This is effective for two reasons. First, since these quantities depend on the amplitude ratio and phase difference between observed vertical and radial fields; the unknown primary normalization factor is removed by the amplitude ratio, and the unknown primary phase reference is removed by the phase difference. Second, during the time the instrument measures and records all field components for each frequency, the instrument temperature is effectively constant; thus the unknown temperature-dependent gain and phase shift are also constant and are removed by the calculation. An added advantage is the fact that ellipticity measurements are virtually unaffected by small errors in loop alignment and orientation (*Frischknecht et al., 1991*).

Interference from external noise sources is a serious problem when the additional set of receiver loops is added for the SPATGRAD configuration (see Figure 38). Obviously, it is desirable to minimize the length of connections between the sensing loops and the receiver preamplifier. Since the connecting wires act as an antenna, any signal induced in them will be subject to the same amplification as the desired signal from the sensing loop. For the "basic" single set of loops, the preamplifier and multiplexing relay are located inside the loop housing so that the connecting wires are only a few centimeters long. For the SPATGRAD configuration, the preamplifier and relays are

located midway between the two loop housings, and the connecting wires are about 30 cm long. The additional wire length greatly increases the instrument noise sensitivity. It was found that useful spatial gradient measurements with this particular instrument are only possible for  $r$  spacings between 1 m and 2 m. For smaller spacings, the close proximity of the connecting wires to other metallic cables causes serious coupling problems. For larger spacings, the decrease in signal strength makes measurement error too large.

#### Instrument Sensitivity

The measuring sensitivity of the "basic" sounder was evaluated in the USGS model tank (dimensions 3.7 x 2.8 x 1.5 m) using a brine/sand physical model and  $r$  spacings of 0.5 m and 1 m. For these short spacings, the instrument can resolve changes on the order of 0.5 degrees tilt and 0.5% (0.005) ellipticity. Resolution at longer spacings is degraded by low signal strength; the computer acquisition program compensates somewhat by stacking a preselected number of samples (usually five or ten). Depending on the noise level, the measurement resolution for spacings of 4 m or larger is estimated at about 2 to 5 degrees of tilt and 2 to 5% ellipticity. At present, there are no laboratory data on measuring sensitivity for the SPATGRAD configuration; however, experience with field tests of the instrument places the resolution limit at about 2 degrees change in phase and a change of 0.02 in amplitude, using  $r = 2$  m and  $\Delta r = 0.5$  m.

### Data Acquisition and Reduction

In computer-controlled mode, the receiver selects frequencies and multiplex relay settings based on instructions from the computer. An analog-to-digital converter continuously monitors and updates eight different voltages which respectively represent in-phase signal, quadrature signal, receiver battery voltage, receiver console internal temperature, amplifier gain, gain multiplier, and two system diagnostics from different points in the electronics.

The existing computer acquisition program scans 48 frequencies spaced logarithmically as evenly as allowed by the minimum increment of 100 kHz. The time required to record a single sounding for a single set of receiver loops is two minutes if no stacking is performed; the time increases to twenty minutes if ten samples are stacked. Most of this is "dead time" deliberately included in the computer program; each time a multiplex relay is switched, the computer waits 1.2 seconds before recording to allow damping of amplifier transients.

The data from a sounding is stored for interpretation and printed as shown in Figure 40. Survey and system information are printed as a header, followed by observed data in millivolts. The HCPL and PERP designations refer respectively to the horizontal coplanar ( $H_z$ ) and perpendicular ( $H_r$ ) transmitter-receiver configurations, while the "in" and "qd" designations refer to the in-phase and quadrature components. When the SPATGRAD configuration is used, a separate data set is stored and printed for each pair of loops.

| CSM SURVEY FIELD STA3 REPEAT |         |                    |         |         |
|------------------------------|---------|--------------------|---------|---------|
| DATE: 210391                 |         |                    |         |         |
| HEIGHT(cm): 26.6             |         | COIL SEP.(cm): 200 |         |         |
| BATTERY HIGH = 12.49         |         | LOW = 12.49        |         |         |
| TEMP. HIGH = 67              |         | LOW = 65.9         |         |         |
| AVERAGE GAIN = 3634.2        |         |                    |         |         |
| freq(Khz)                    | in-HCPL | qd-HCPL            | in-PERP | qd-PERP |
| 3                            | -166.9  | 317.6              | 13.2    | -4.5    |
| 4                            | -219.4  | 322.3              | 9.0     | .2      |
| 5                            | -270.7  | 302.7              | 5.1     | -5.8    |
| 6                            | -286.3  | 297.4              | 2.4     | -12.8   |
| 7                            | -311.9  | 282.7              | 6.8     | -5.8    |
| 8                            | -322.4  | 271.5              | 8.8     | -13.8   |
| 10                           | -336.8  | 263.7              | 2.9     | -13.3   |
| 12                           | -358.8  | 253.9              | 1.5     | -17.5   |
| 14                           | -373.9  | 257.1              | 4.6     | -18.7   |
| 18                           | -387.6  | 273.4              | -.4     | -26.0   |
| 21                           | -366.1  | 332.0              | -7.0    | -29.0   |
| 24                           | -371.7  | 341.8              | -8.9    | -32.1   |
| 27                           | -421.8  | 322.8              | -7.7    | -39.0   |
| .                            | .       | .                  | .       | .       |
| .                            | .       | .                  | .       | .       |
| .                            | .       | .                  | .       | .       |
| 220                          | -709.4  | 815.7              | -136.6  | -455.5  |
| 230                          | -507.2  | 368.2              | 9.3     | -322.2  |
| 240                          | -195.0  | 301.3              | -4.1    | -187.4  |
| 251                          | -18.5   | 101.8              | -13.8   | -43.8   |
| 260                          | -75.1   | 342.0              | -43.8   | -82.9   |
| 270                          | -116.8  | 269.5              | -48.7   | -58.5   |
| 280                          | -122.2  | 135.7              | -37.7   | -16.0   |

Figure 40. Sample printout of observed sounder data.

### Polarization Ellipse and Spatial Gradient Calculation

As noted earlier in this chapter, the instrument measures un-normalized components of the magnetic fields. This has no effect on computation of the polarization ellipse parameters, since the same values are obtained whether the fields are normalized or not. To compute the ellipse parameters, observed in-phase and quadrature data is converted to amplitude and phase angle; the tilt angle is then obtained from equation [41] in the chapter on theory, and the ellipticity is obtained from either equation [42] or equation [43].

Computation of spatial gradients by direct insertion of un-normalized observed data into equation [44] does NOT, however, produce the same results as computations using normalized data. The denominator of equation [44] uses  $H_z$  fields recorded at two different  $r$  spacings; therefore the primary field is different for each spacing, and the normalizing factors will not be completely cancelled by the computation. Before the gradient is calculated, one of the  $H_z$  terms must be scaled to account for the different primary field.

Using the geometry shown in Figure 4 in the theory chapter, consider the relation of the normalized and un-normalized fields in the plane of the source loop at two different  $r$  spacings. To normalize the magnetic field measured by a particular receiver loop, the observed amplitude is divided by the amplitude of the primary field at the loop center:

$$H_1^n = \frac{H_1^0}{P_1}, \quad H_2^n = \frac{H_2^0}{P_2} .$$

The superscripts  $n$  and  $o$  denote normalized and observed values respectively; the subscripts denote the different  $r$  spacings. For a dipole approximation, i.e., when the loop dimensions are small compared to  $r$ , the primary field decays as the cube of distance, and the amplitudes are related by:

$$P_2 = P_1 \left[ \frac{(r-\Delta r)}{r} \right]^m ,$$

where  $m = 3$ . The field relations are now expressed using a single primary field amplitude:

$$H_1^n = \frac{H_1^0}{P_1}, \quad H_2^n = \frac{H_2^0}{P_1 \left[ \frac{(r-\Delta r)}{r} \right]^m} .$$

When field ratios are calculated, the primary field amplitude is cancelled and the ratio is the same as that which would be obtained if normalized field components were measured:

$$\frac{\Delta r H_r}{\Delta H_z} = \frac{\Delta r H_{r1}^n}{(H_{z2}^n - H_{z1}^n)} = \frac{\Delta r \left( \frac{H_{r1}^0}{P_1} \right)}{\left( \frac{H_{z2}^0}{P_2} - \frac{H_{z1}^0}{P_1} \right)} = \frac{\Delta r H_{r1}^0}{\left[ H_{z2}^0 \left( \frac{r}{r - \Delta r} \right)^m - H_{z1}^0 \right]} \quad (45)$$

Using equation [45] with  $m = 3$  is inappropriate for the existing instrument because the dipole approximation is not valid. The decay of the primary field over distance is complicated for relatively large loops or close spacings. However, equation [45] still holds true for any given pair of  $r$  spacings if the exponent  $m$  has an appropriate value. Since the computer forward modeling program performs an exact calculation of the primary field for any loop size and spacing, it is relatively simple to compute the necessary values of  $m$  for a given loop radius and selected pairs of  $r$ . Figure 41 shows the behavior of a correction term  $\xi$ , where  $m = 3 + \xi$ , calculated for a loop radius of 0.1524 m and a  $\Delta r$  of 0.5 m. The  $x$ -axis is the  $r$  spacing of the farther loop set. It is clear that  $\xi$  approaches zero as  $r$  increases.

Using instrument measurements, the normalized spatial gradient is calculated by inserting the observed data, the  $r$  spacing of the far loops (2 m), and the  $\Delta r$  value (0.5 m) into equation [45]. For the  $r$  spacing of 2 m, the exponent  $m = 3.0177979$ .

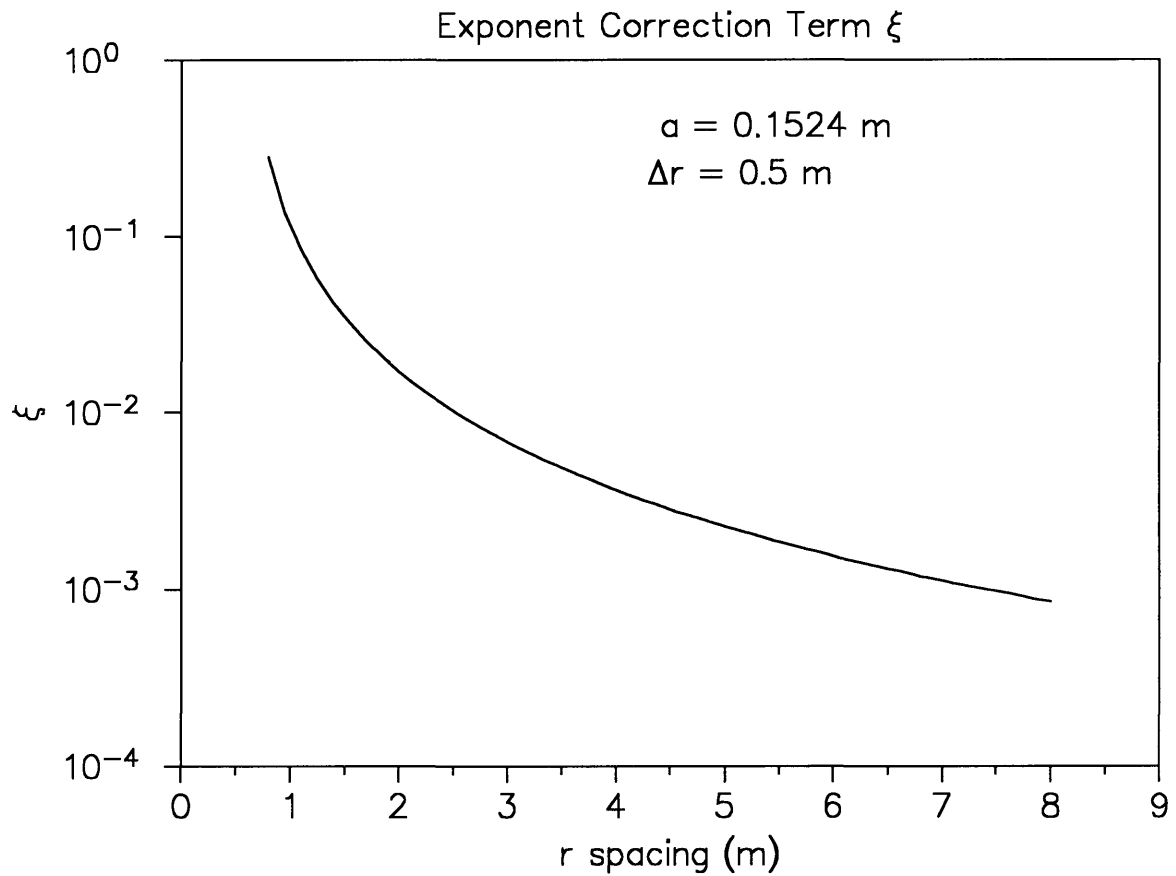


Figure 41. Behavior of exponent correction term for varying  $r$ -spacing of the farther loop set.

## FIELD SURVEY EXAMPLES

The following examples show results of some sounding and profiling field tests. The computer inversion programs were used to interpret polarization ellipse ellipticity data and spatial gradient (SPATGRAD) amplitude data computed from instrument observations. Tilt angle data were also computed, but not used in all inversions because they are sensitive to loop alignment errors. Where tilt data is shown, a shift of about 1.5 degrees has been applied to each observed curve to correct the estimated error; this correction value was estimated by comparing observed low-frequency tilt angles for  $r \leq 1$  m with the expected value of 90 degrees. SPATGRAD phase data were discarded in all cases due to extreme scatter.

### Colorado School of Mines survey

The land-surveying field at Colorado School of Mines in Golden, Colorado, is not an optimum environment for EM methods, since it contains numerous high-tension and residential power lines and is within two miles of several high-power radio and television transmitter towers. As such, it provides an opportunity to evaluate the sounder performance in the presence of excessive EM interference. In fact, this area was chosen for sounder tests because, in an unrelated study, terrain conductivity measurements proved nearly impossible to obtain. The calculation results for this example are

supported by physical sample measurements, and demonstrate the ability of the method to perform accurate soundings in a high-noise environment.

### Polarization Ellipse Measurements

Figure 42 shows observed data and the inverse solution for  $r$  spacings of 2 and 4 m. As was discussed in the chapter on forward models, the sharp peak in the 4 m ellipticity curve indicates the existence of a fairly large  $K$  value somewhere in the section. Such a value is seen in the inversion model of Figure 43, where  $K_2$  equals 41. The relatively low resolution error for  $K_2$  undoubtedly results from the influence of  $K$  on the frequency where the ellipticity peak occurs.

At the sounding location, a geologic map (*Scott, 1972*) shows the geology as thin soil cover over inferred bedrock of Lyons Sandstone (Lower Permian). Assuming the top layer of the inversion model represents the soil cover, the calculated  $K_2$  of 41 is unexpectedly large for a sandstone (see Table 1); a value less than 10 is more common. The calculated depth to the second layer is only about 1 m, so a soil auger was used to examine the section. Samples from the top layer are dry loose soil, consistent with the high  $\rho_1$  and low  $K_1$  of the inversion model. A soft, fine-grained sandstone was encountered at a depth of 1 m; sample fragments contain small amounts of biotite and tourmaline, and have a limonite coating on the quartz grains. Electrical measurements performed on the fragments by the USGS petrophysics laboratory show a  $\rho$  of 100 to 120  $\Omega\cdot\text{m}$  and a  $K$  of 35 to 45 at 1 MHz, decreasing to 10 at 100 MHz. The higher laboratory

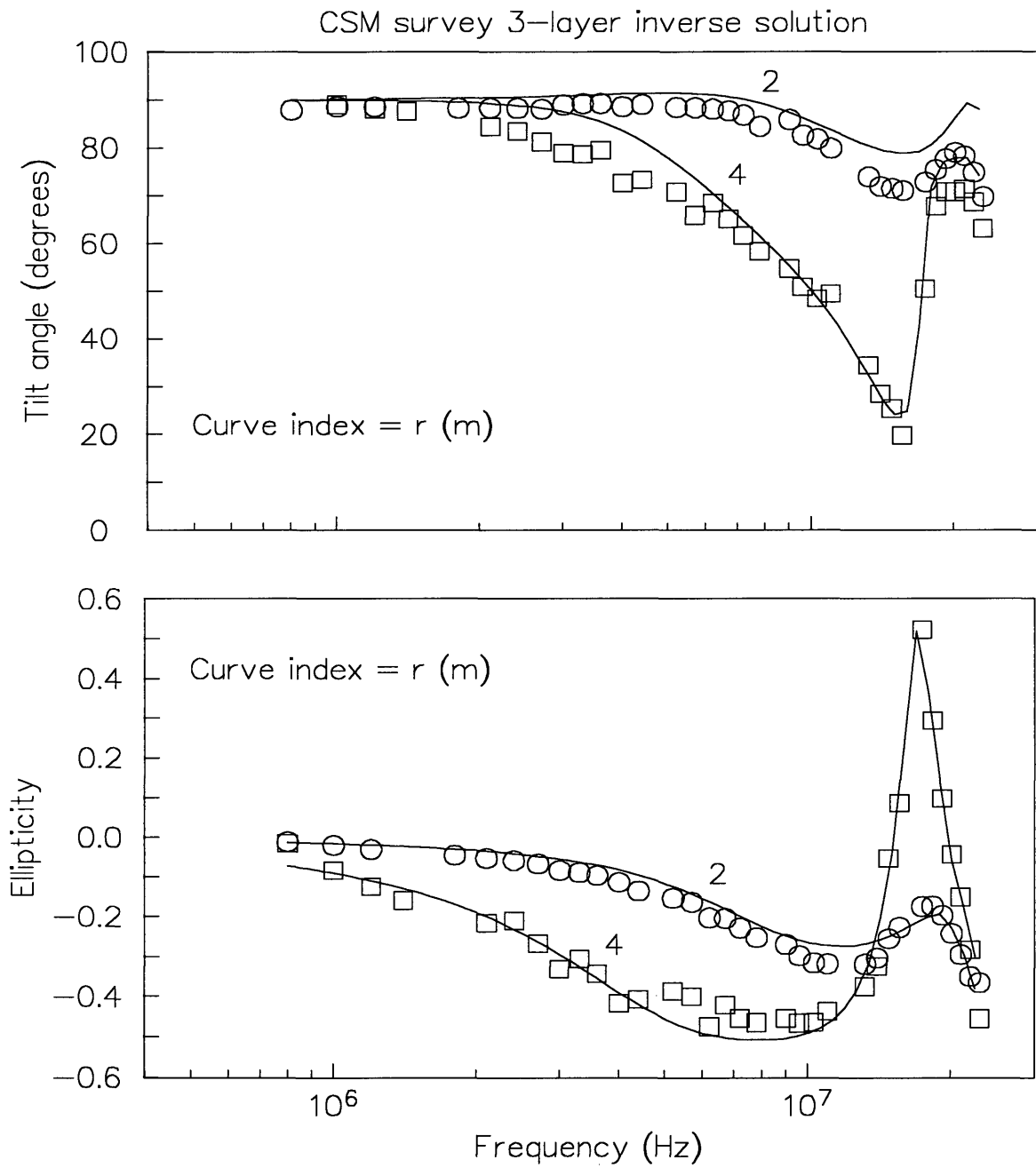


Figure 42. A three-layer inverse solution for polarization ellipse data recorded near Golden, Colorado, using two  $r$  spacings. The symbols are observed data, the solid lines are calculated data.

## CSM survey inversion model

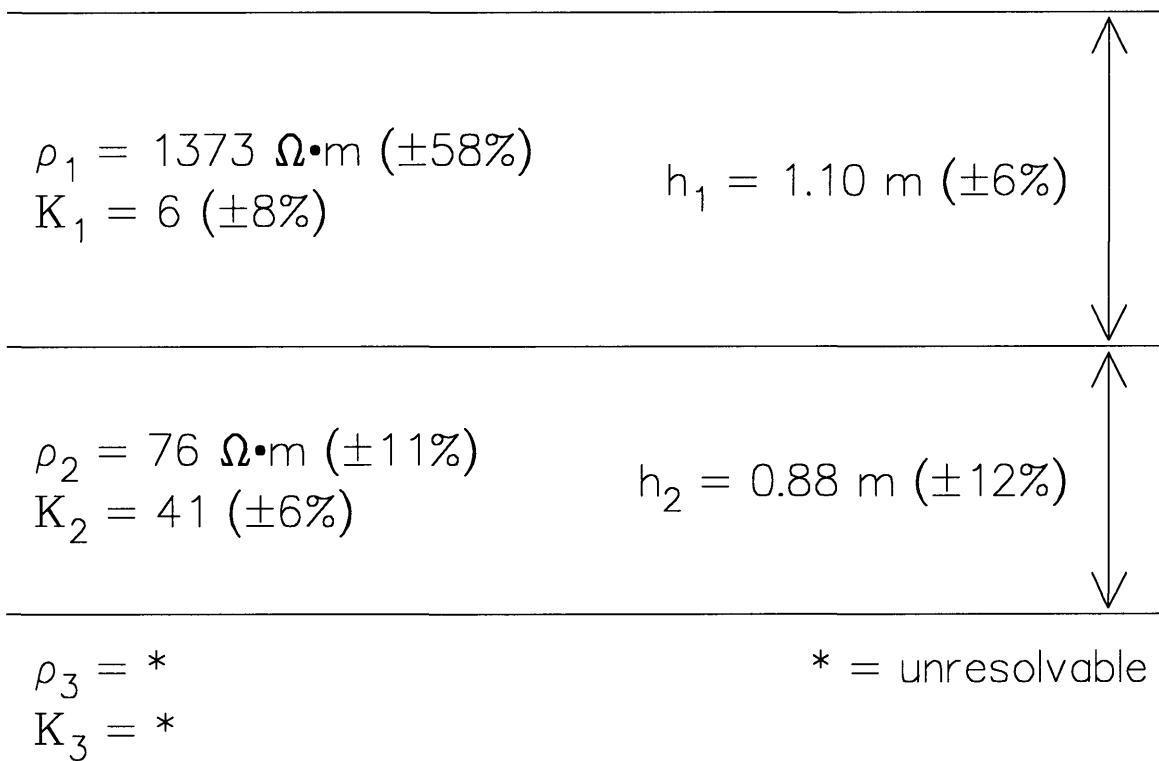


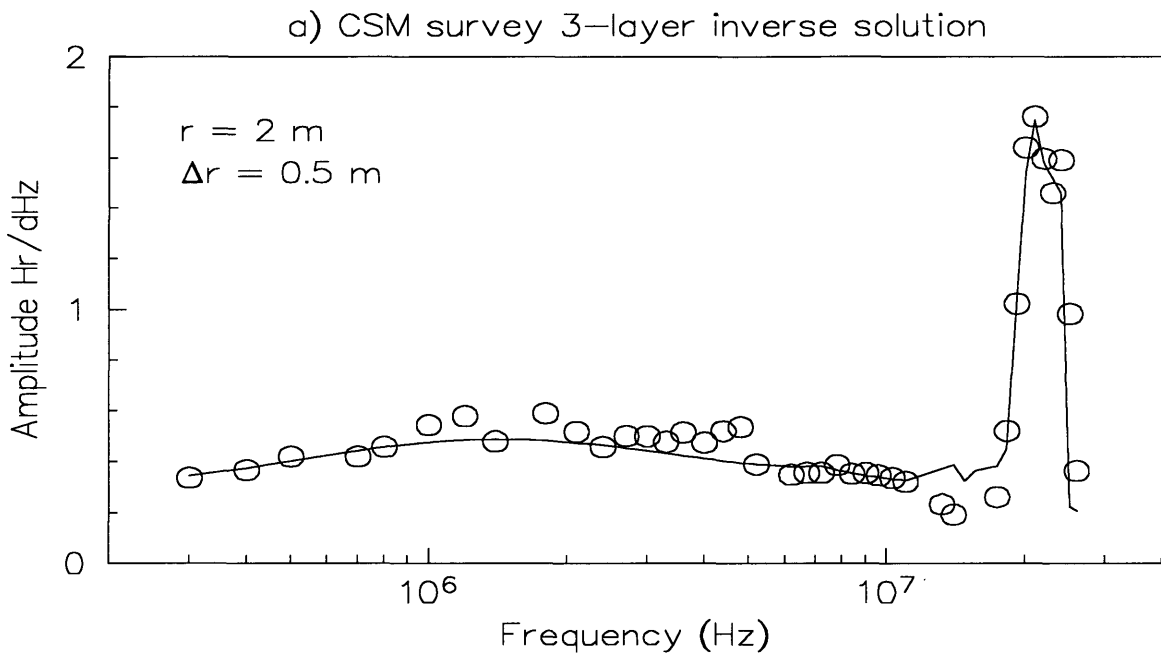
Figure 43. The three-layer model for the inverse solution shown in Figure 42. The numbers in parentheses are parameter resolution errors.

$\rho$  compared to the inversion  $\rho_2$  of 76 is probably due to partial drying of the fragments during handling. Although the laboratory K measurements show strong frequency dependence, they are consistent with the inversion  $K_2$  value for the sounder frequency range.

### Spatial Gradient Measurements

The site was re-occupied with the SPATGRAD sounder about eight months after the polarization ellipse data were recorded. The observed and calculated gradient amplitude data are shown in Figure 44, along with the inversion model. The parameter resolution errors are much larger than those for the polarization ellipse data. This is partly due to the higher EM interference sensitivity of the prototype gradient receiver array (discussed in the instrumentation chapter), and partly due to performing inversion with only a single data curve.

In spite of the large resolution errors, the inverse solution yields layer thicknesses very close to those obtained with the polarization ellipse data, and an identical value for  $K_2$ . The  $K_1$  value has the smallest resolution error but is nearly three times larger than the value from the polarization ellipse data. It is tempting (but speculative) to explain the difference as a variation in soil moisture content because the polarization ellipse data were recorded during a summer dry spell, while the SPATGRAD data were recorded in the spring rainy season.



b) CSM survey inversion model

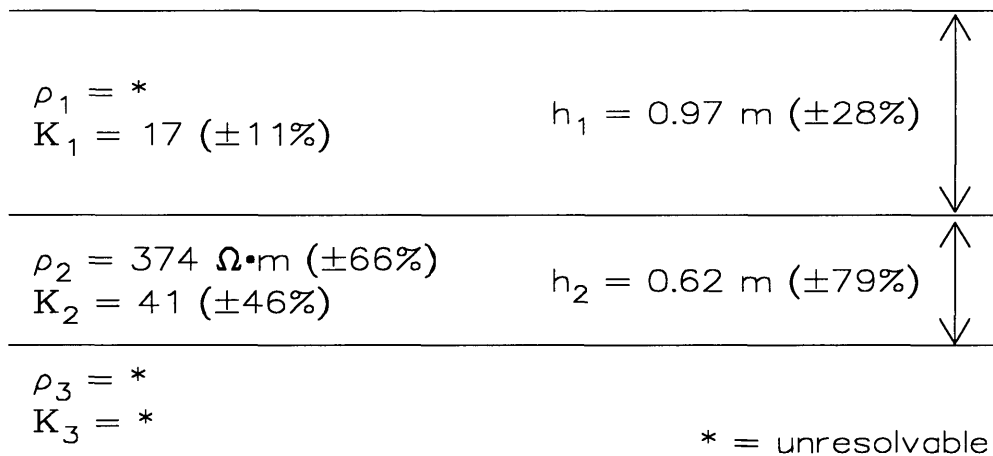


Figure 44. A three-layer inverse solution of SPATGRAD data recorded near Golden, Colorado. (a) Observed data (symbols) and calculated data (solid lines). (b) Inversion model. The numbers in parentheses are parameter resolution errors.

### Iowa Survey

In October of 1989, a polarization ellipse survey was done near Cedar Rapids, Iowa, as part of a groundwater study conducted by the USGS Water Resources Division. This was the first full-scale test of the relatively crude "first generation" (i.e., rough wooden coil mounts and boom) polarization ellipse instrument. An extensive terrain conductivity survey was also performed at this time. In September of 1992, the SPATGRAD instrument was used at the same site. Figure 45 shows the location and layout of the survey grid. SPATGRAD data were recorded along three profiles; polarization ellipse data were recorded along line 00 and extended 260 m beyond station 120NE. The area is flat, brushy, and lightly wooded. A dry slough (marshy low ground) crosses the grid as indicated.

In the time interval between 1989 and 1992, a nearby river flooded and covered the survey area with two meters of water. The only apparent effect of the flood is the addition of a thin (about 10 cm) surface layer of clean, fine-grained sand across the grid between stations 20NE and 40NE. One significant environmental difference between the 1989 and the 1992 survey is the amount of precipitation. The 1989 survey was performed during a dry spell, while the 1992 survey took place during a period of sustained record-setting rainfall (e.g., major flooding occurred 40 miles southeast of the survey area), such that the soil was fully saturated.

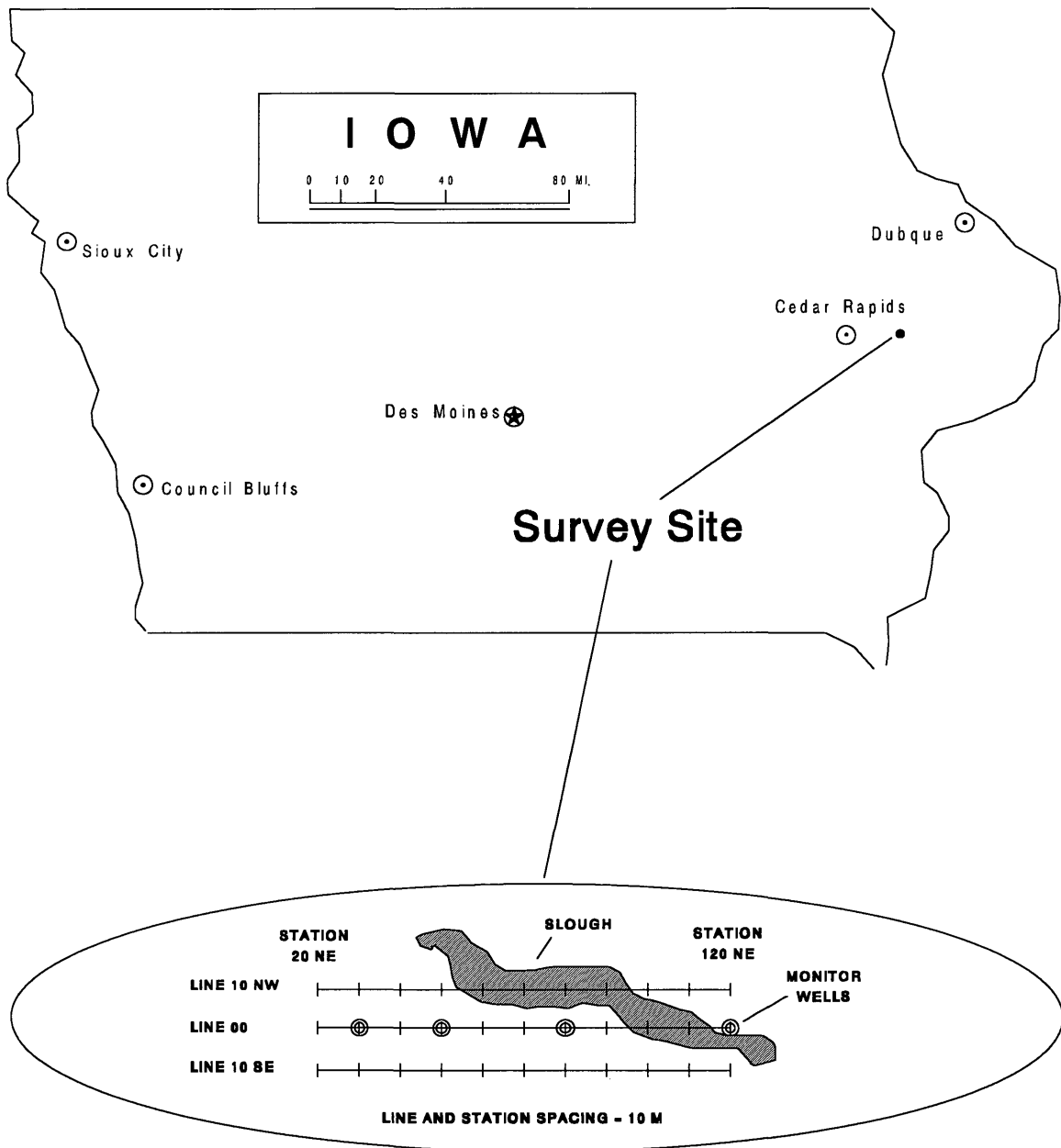


Figure 45. Location map and survey grid for polarization ellipse and SPATGRAD measurements recorded near Cedar Rapids, Iowa.

This example demonstrates the ability to construct detailed shallow profiles from high-frequency soundings, and emphasizes the lack of detailed shallow information provided by terrain conductivity measurements. One important result is that sounding inversions using only a single SPATGRAD amplitude curve yield models with detail and parameter resolution comparable to models based on joint inversion of ellipticity curves for three  $r$  spacings. The surveys themselves showed that the instrument electronics, particularly the fiber optic connections, are capable of performing in subfreezing temperatures and extreme dampness.

#### Polarization Ellipse Measurements

Soundings using loop spacings of 1, 2, and 4 m were made at 18 stations along line 00 between station 40NE and 360NE. Sample plots of observed data and joint inverse solutions are shown for station 100NE and station 360NE in Figure 46 and Figure 47 respectively. Figure 48 shows a shallow geologic cross-section constructed from monitor well information, and a geoelectric cross-section constructed from the inverse solutions for each station. The error of resolution for most parameters is less than 10%. The values shown for  $\rho$  and  $K$  are averages for the layers (or regions of a layer), and are consistent with other observed values for wet silty/clayey soils and sands (Hipp, 1974; Lytle, 1974). The shallow silty sand lenses at each end of the section are clearly identified by the inversion as layers with  $\rho > 100$  and  $K < 20$ . The silty clay layer corresponds to  $\rho \leq 60$  and  $K > 20$ . The deeper boundary is most likely the

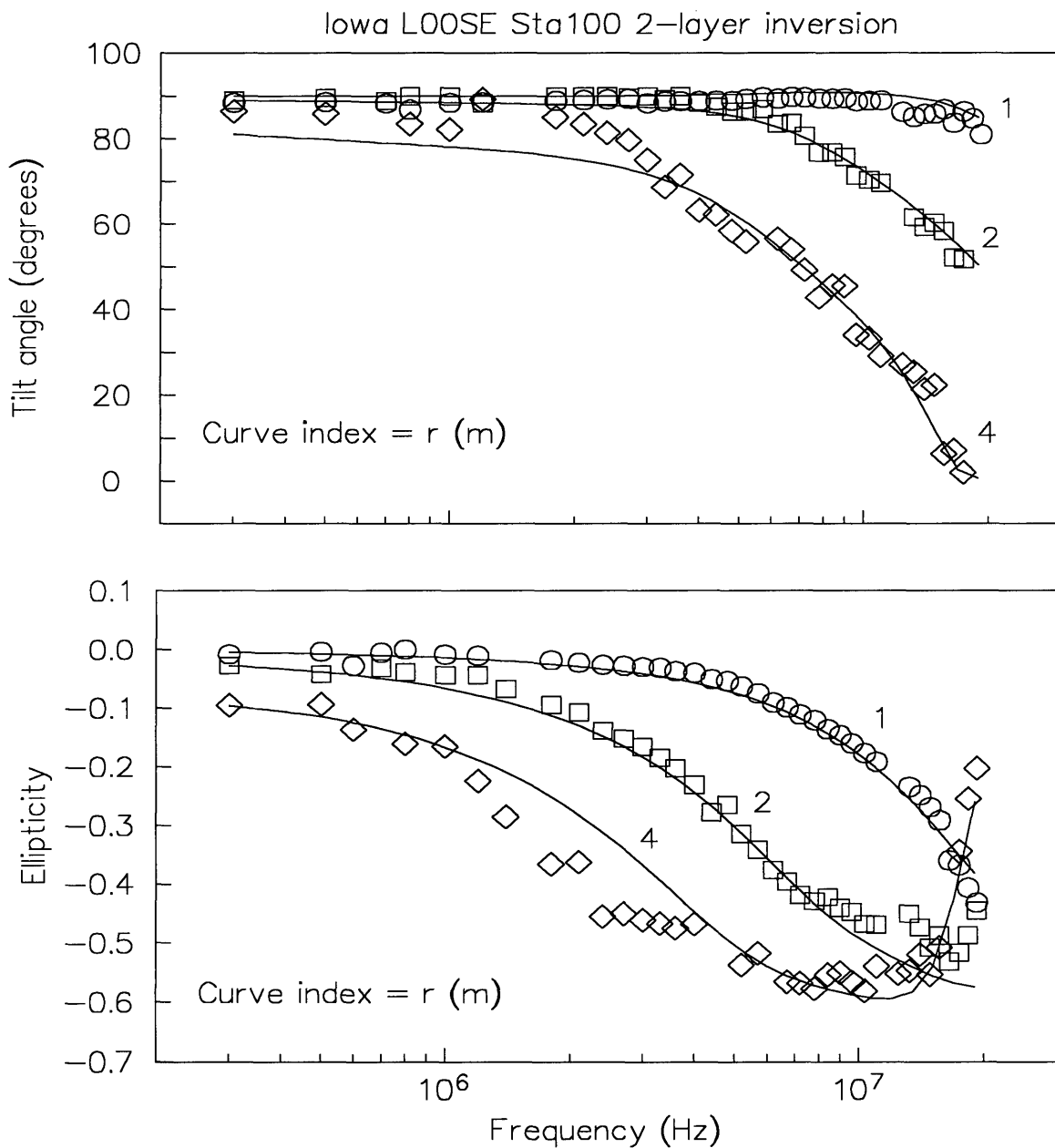


Figure 46. Two-layer inverse solution of polarization ellipse data recorded at station 100NE on line 00 of the Iowa survey grid, using  $r = 1, 2,$  and  $4$  m. The symbols are observed data, and the solid lines are calculated data.

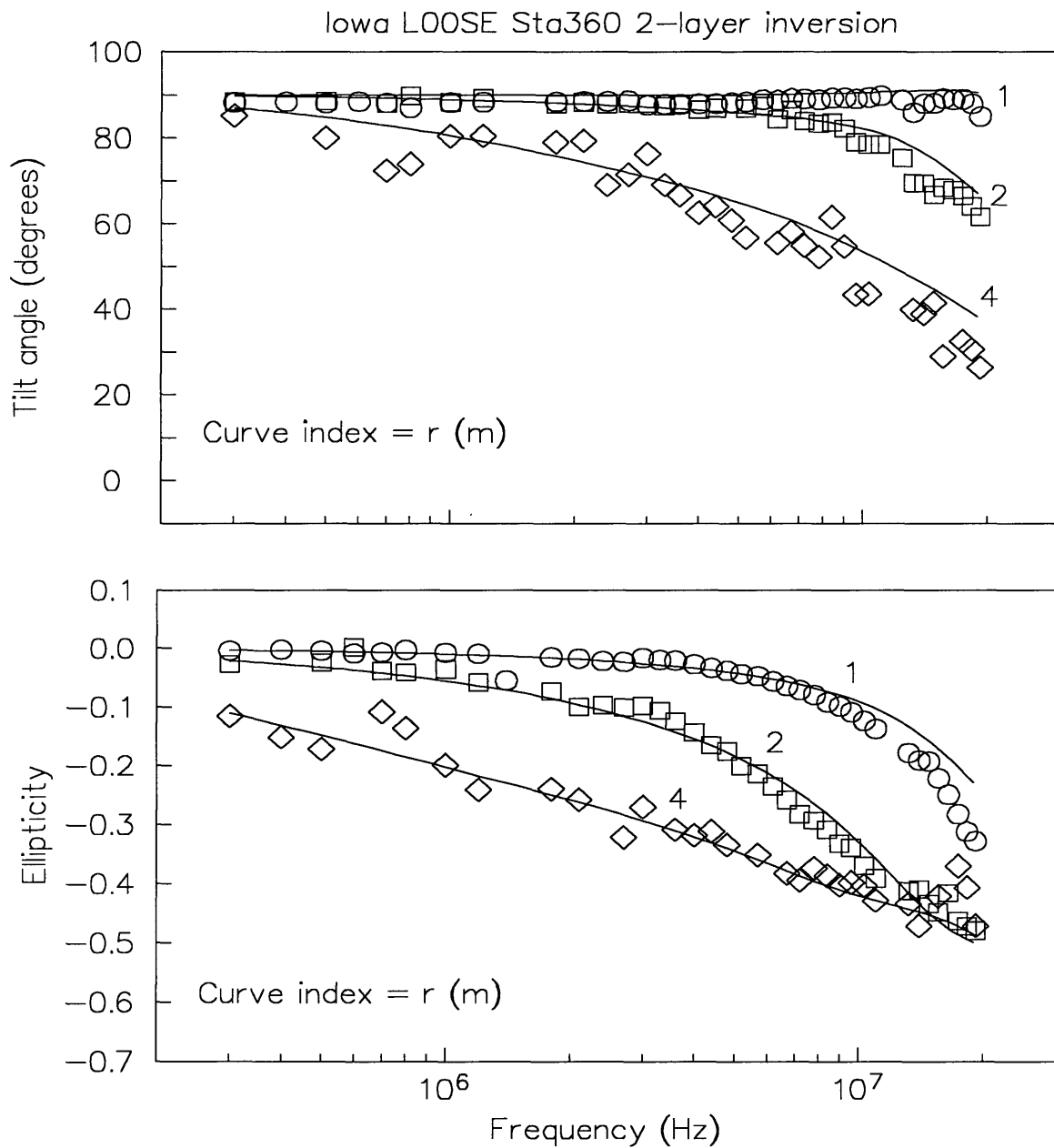


Figure 47. Two-layer inverse solution of polarization ellipse data recorded at station 360NE on line 00 of the Iowa survey grid, using  $r = 1, 2,$  and  $4$  m. The symbols are observed data, and the solid lines are calculated data.

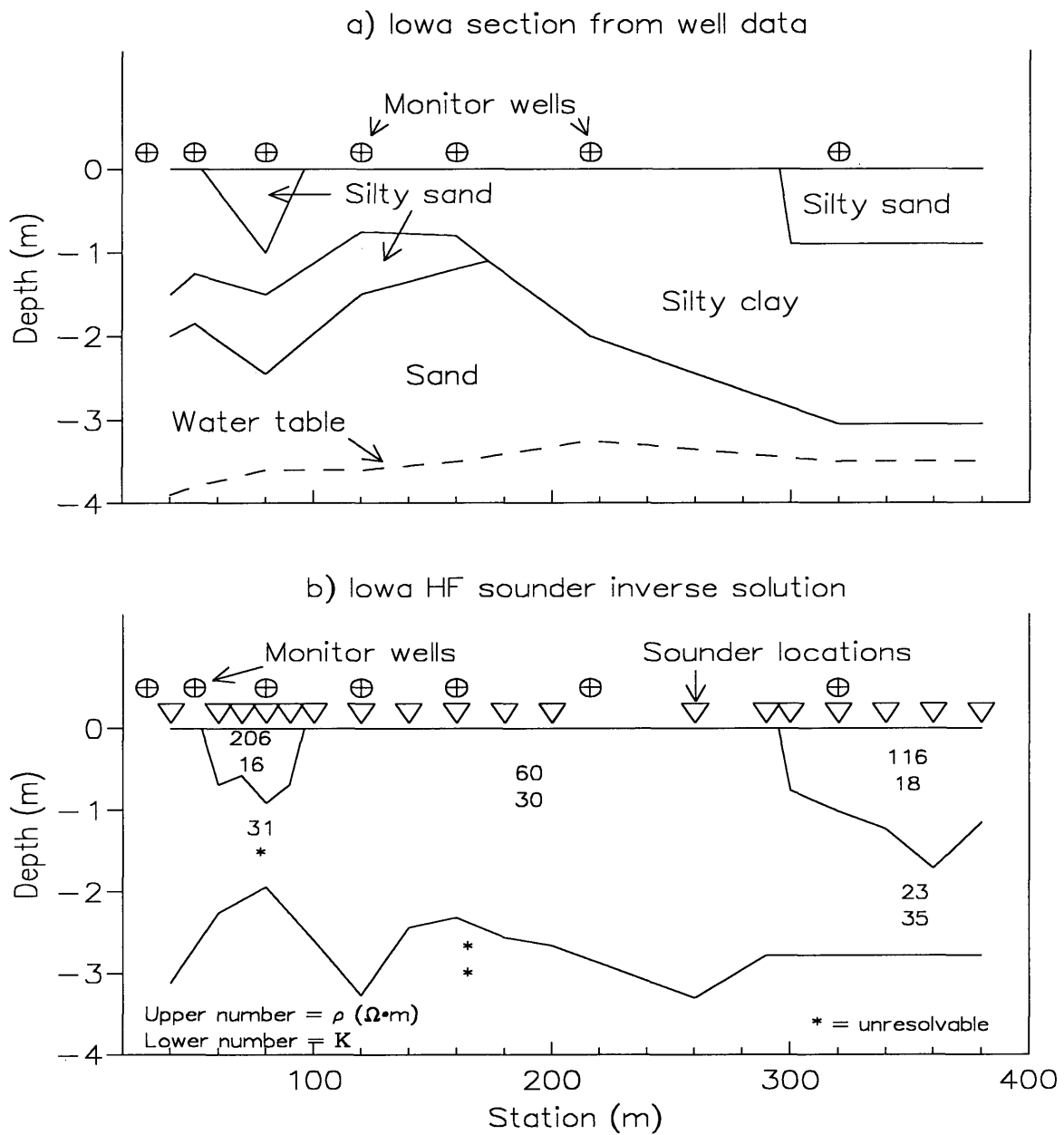


Figure 48. Comparison of a shallow geologic cross-section from monitor well data, and a geoelectric cross-section from inversions of sounder data along line 00 of the Iowa survey grid. (a) Geologic section. (b) Geoelectric section.

capillary fringe above the water table. The electrical parameters of the bottom layer are unresolvable, mainly due to scatter in the 4 m data and also because the maximum frequency was 19 MHz for this survey.

One problem encountered in this survey was the difficulty of placing the transmitter and receiver loops at the same height above the ground; for the 4 m spacing, slight terrain irregularities can cause one end of the instrument boom to "hang in the air". It is possible to dispense with the rigid boom and position each coil independently, but this was not done, as it requires very accurate measurement of coil positions and orientations for data interpretation. The desire to minimize this problem with use of short coil spacings was one reason for experimenting with spatial gradient measurements.

#### Spatial Gradient Measurements

A total of 33 SPATGRAD soundings were recorded on the survey grid. Figure 49 and Figure 50 show sample observed and inversion data from four adjacent stations on line 00. These samples illustrate the complicated curve shapes and degree of response variability possible in high-frequency shallow mapping. It is clear that measurements must be made at many closely spaced frequencies in order to adequately define the curves. For most of the 33 soundings, the parameter resolution errors range between 2% and 20%; a parameter with an error of 50% or more is treated as unresolvable.

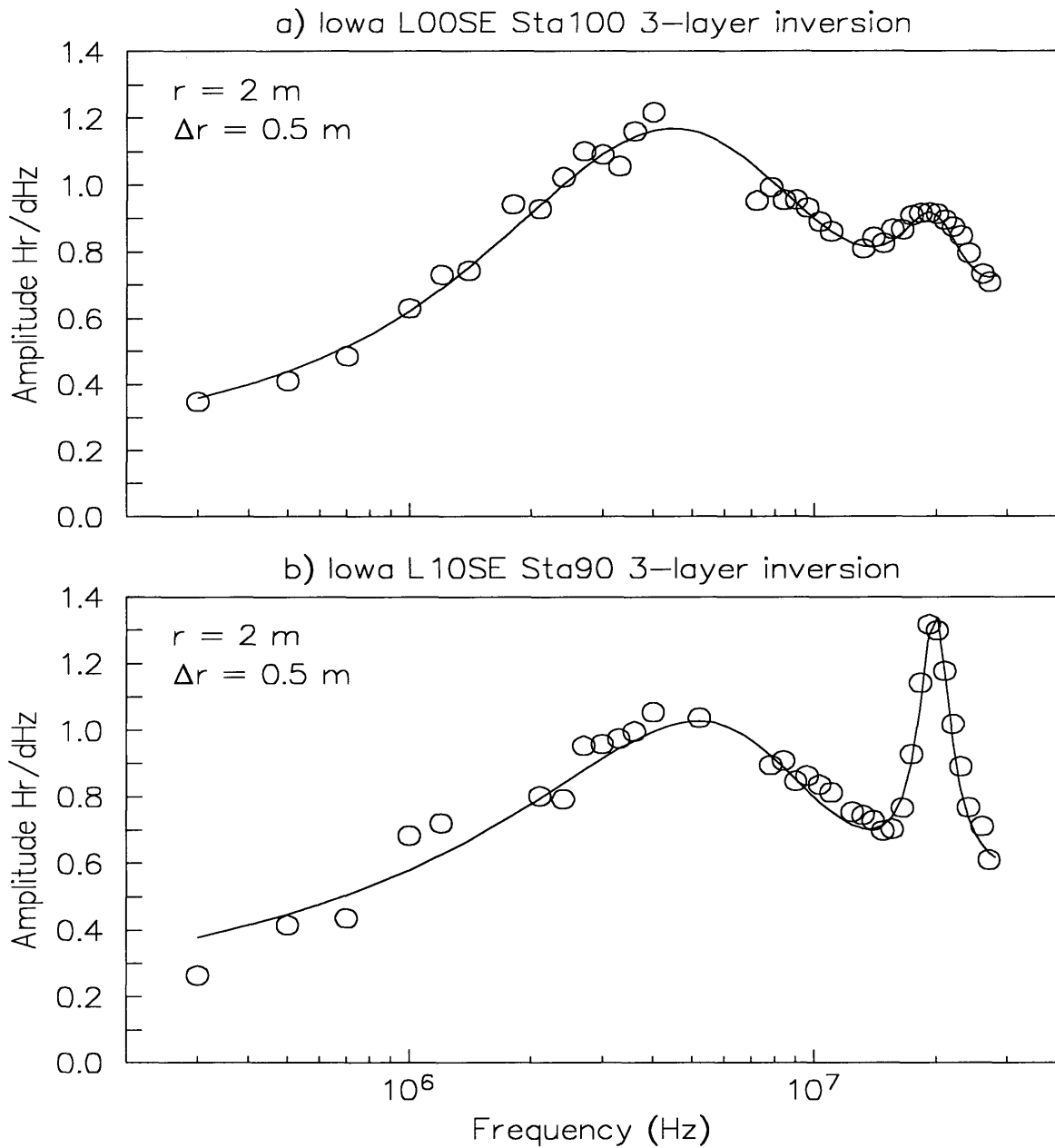


Figure 49. Three-layer inverse solutions of SPATGRAD amplitude data recorded at station (a) 100NE and (b) 90NE on line 00 of the Iowa survey grid. The symbols are observed data, and the solid lines are calculated data.

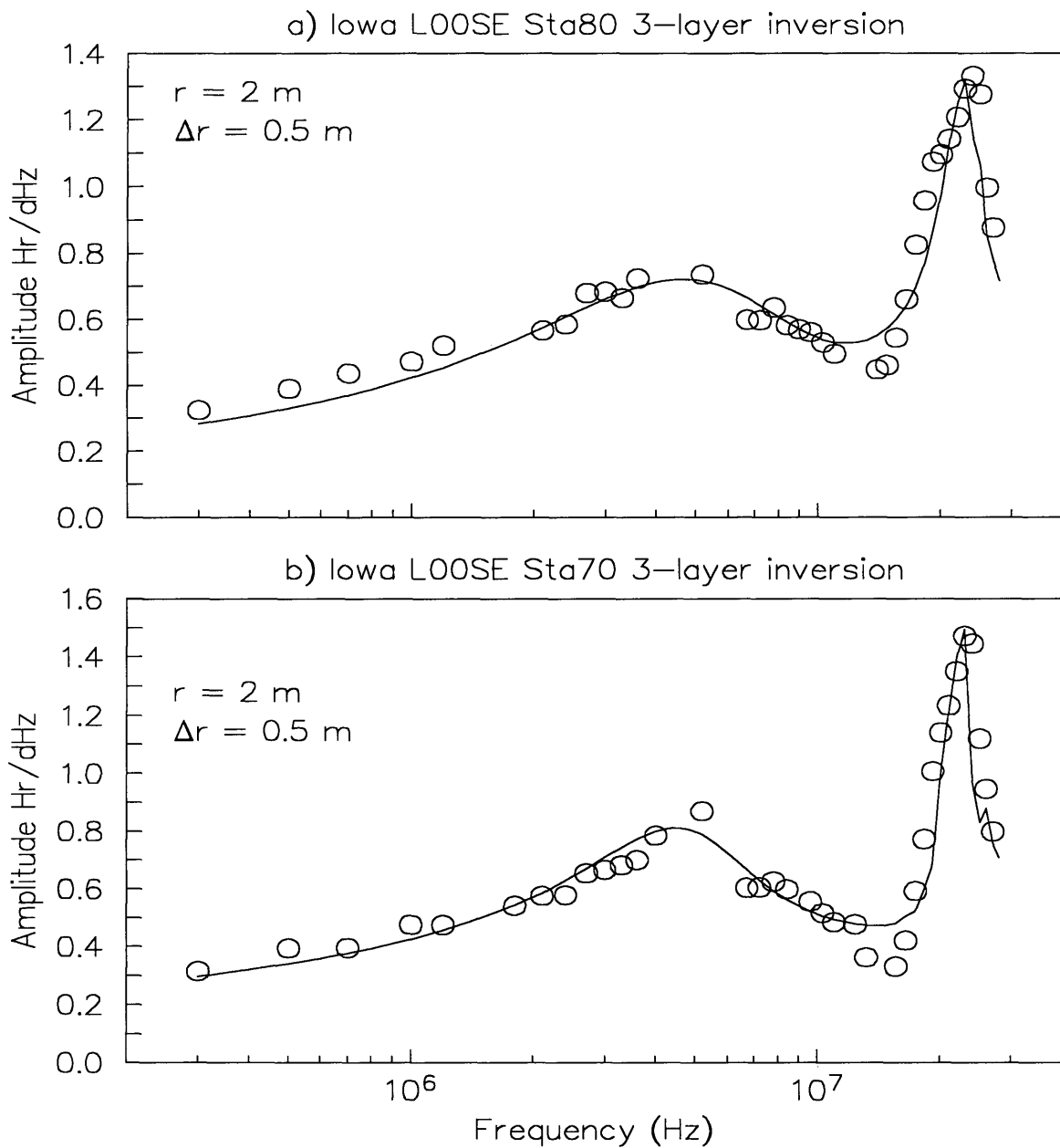


Figure 50. Three-layer inverse solutions of SPATGRAD amplitude data recorded at station (a) 80NE and (b) 70NE on line 00 of the Iowa survey grid. The symbols are observed data, and the solid lines are calculated data.

The variety of sounding curve shapes is reflected by the subsurface variations in the inversion profile of Figure 51. Information from the monitor wells is reproduced above the inversion model; note that the SPATGRAD profile is one third the length of the polarization ellipse profile in Figure 48. The monitor well information is relatively sparse, and thus yields a fairly simple cross-section. The sounder inversions located at well sites are in very good agreement with the well model; however, the additional soundings between monitor well stations reveal a much more complicated subsurface structure. Based on  $\rho$ , the distinction between the silty sand and the silty clay is the same as for the polarization ellipse data (see Figure 48); the silty sand has  $\rho > 100$ , and the silty clay has  $\rho < 60$ . Based on K, the silty clays are similar to Figure 48 ( $K > 20$ ), but the silty sands at stations 30-40 and station 60 have K values much larger than those of Figure 48. This could be a result of a variation in composition, or these zones could be highly-saturated "water traps" where infiltrating rainwater collects.

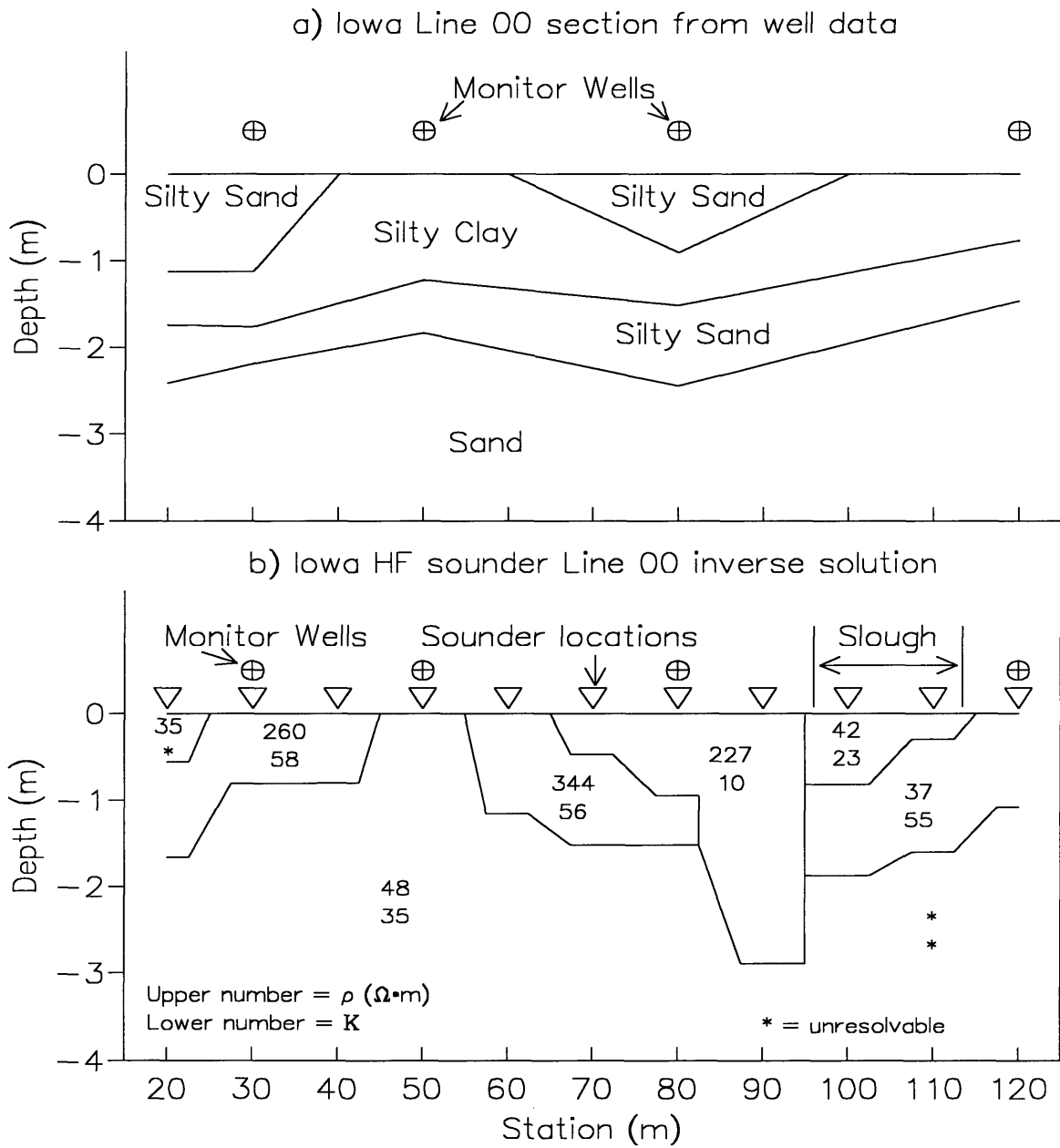


Figure 51. Comparison of a shallow geologic cross-section from monitor well data, and a goelectric cross-section from inversions of SPATGRAD data on line 00 of the Iowa survey grid. (a) Geologic section. (b) Goelectric section.

The inversion cross-section of Figure 51 shows an apparent filled-in shallow drainage channel centered on station 90 and extending from station 60 to station 120 or beyond. The NE edge is filled with silty clay, while the SW edge and deeper center are filled with silty sand. The surface slough is located near the center of the apparent channel. Figure 52 shows cross-sections constructed from data recorded along profiles located 10 m to the NW and SE of line 00. The resolution errors for soundings along line 10NW are relatively large, so construction was rather difficult, but the apparent channel is seen indistinctly, centered at station 100, extending possibly from station 60 to station 120. The surface slough crosses this profile at a shallow angle to the left of the channel center. The cross-section for line 10SE is better resolved, and shows the channel centered at station 90, with its center reduced in depth and edges extending possibly from station 40 to station 120. A possible deeper channel is seen at station 50, but it is a "one station" feature, i.e., adjacent stations do not support the picture; if the sounding for station 50 is discarded, the structure vanishes.

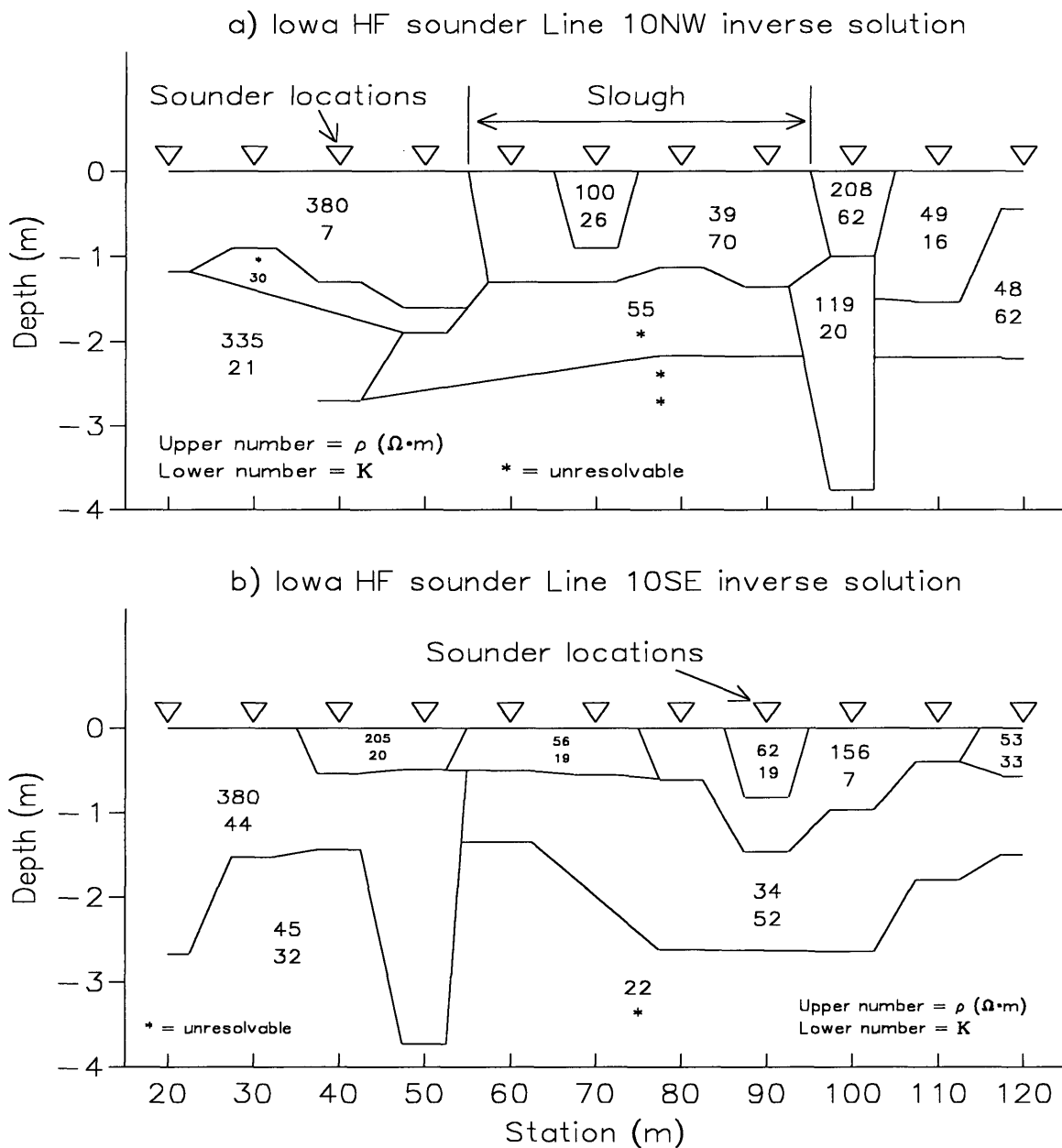


Figure 52. Geoelectric sections from inversions of SPATGRAD data on (a) line 10NW and (b) line 10SE of the Iowa survey grid.

### Terrain Conductivity Measurements

Terrain conductivity measurements were also recorded at the site, allowing comparison of the shallow mapping resolution of terrain conductivity with that of the high-frequency sounder. Vertical and horizontal dipole data were collected at 10 m station intervals with a Geonics EM-31 instrument, and a Geonics EM-34 instrument using coil spacings of 10, 20, and 40 m. Figure 53 shows the well-data geologic cross-section for line 00, including layers below the water table, and a three-layer geoelectric cross-section from inversion of the terrain conductivity data. The location of the cross-sections is the same as in Figure 48; in Figure 53 geologic layers at depths < 4 m are lumped together as the "silty clay" surface layer. The geoelectric cross-section provides no information on layers at a depth less than 10 m, and there is no apparent correlation between the geologic cross-section and the layers shown in the geoelectric sections. The terrain conductivity measurements are unable to map the shallow layers, and do not resolve the deep layers with any degree of accuracy.

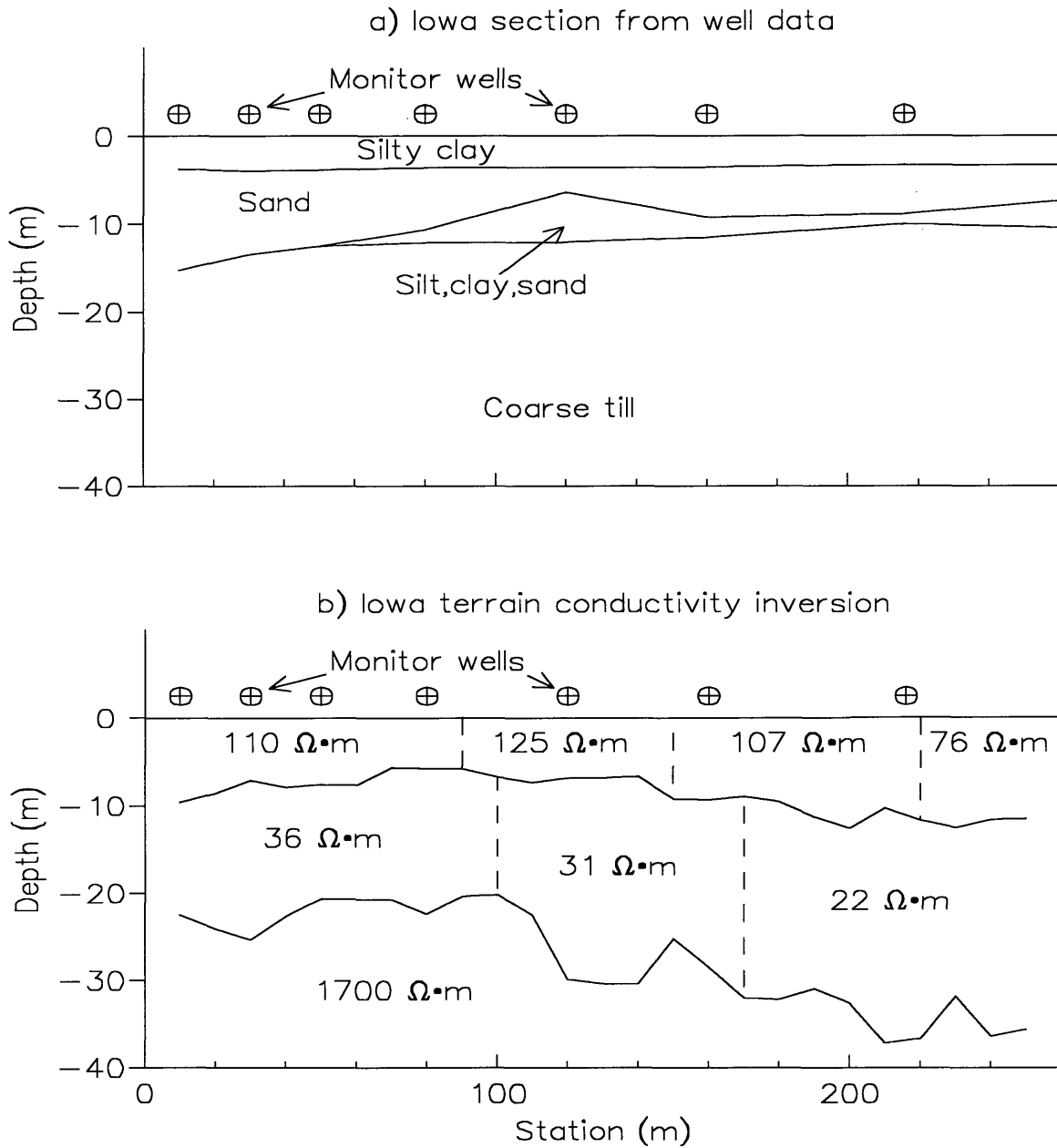


Figure 53. Comparison of (a) a geologic cross-section from monitor well data, and (b) a geoelectric cross-section from inversions of terrain conductivity data on line 00 of the Iowa survey grid. The geologic layers at depths < 4 m are combined into one.

### Nevada Survey

The Pittman site at Henderson, Nevada, is a polluted area that has been studied with a variety of geophysical tools, including seismic reflection (*Miller and Steeples, 1990*), terrain conductivity (*Weber et al., 1984; Weber and Flatman, 1986*), and complex resistivity (*Walther et al., 1983*). The near-surface geology consists of 5 to 15 m of alluvial deposits overlying the siltstone and clay unit of the Muddy Creek Formation (Miocene and Pliocene).

From the viewpoint of electromagnetic geophysics, the site is extremely challenging: conductive alkaline soil, chain-link fences, overhead power lines, nearby radio towers, and buried metallic debris including large hoops and automobile frames. This survey established a high-temperature failure point of 115° Fahrenheit for the instrument electronics (measured inside the receiver console), and serves as a worst-case scenario for cultural contamination. Only polarization ellipse data has been recorded at this site.

### Polarization Ellipse Measurements

In May 1991, soundings were recorded at 11 locations using  $r$  spacings of 2 and 4 m, and a 30 m interval between stations. The cultural noise made inversion difficult, with parameter resolution errors ranging from 5% to 50%. Figure 54 shows a geoelectric cross-section constructed from inversion models selected on the basis of best overall parameter resolution and consistency from station to station. The water table

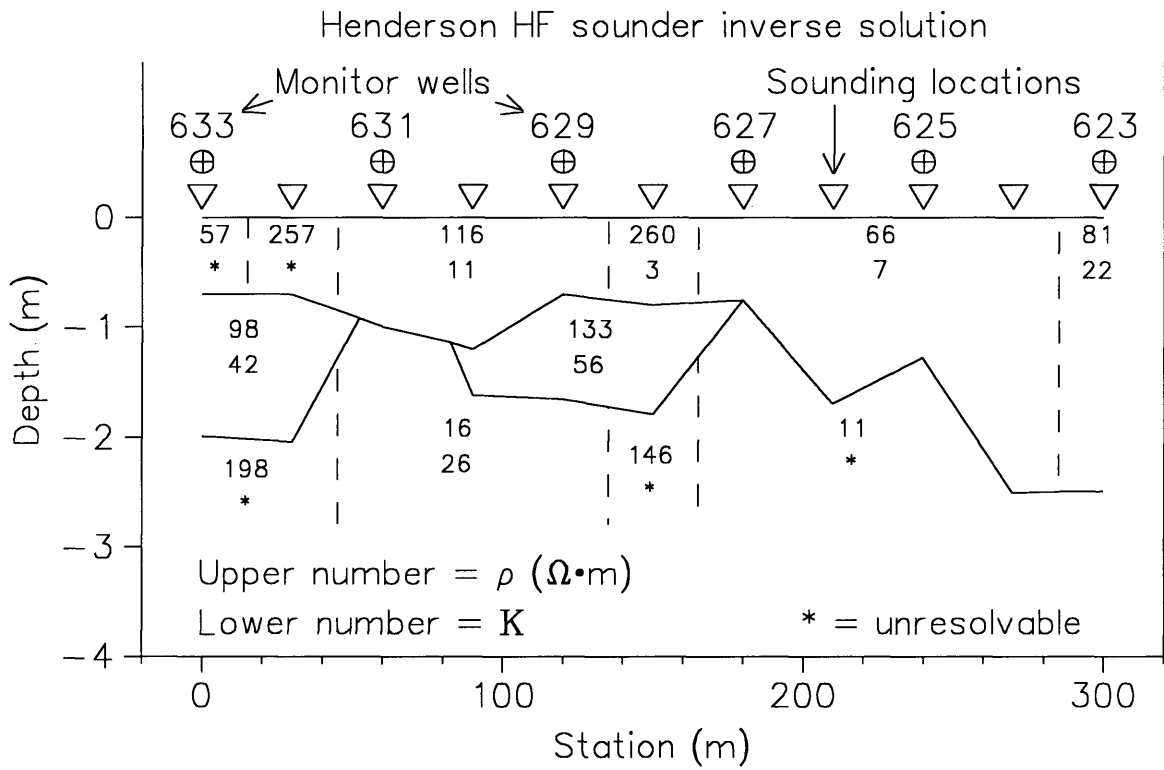


Figure 54. A geoelectric cross-section from inversions of polarization ellipse data recorded at Henderson, Nevada, using  $r$  spacings of 2 and 4 m.

depth is about 5 m, so the section most likely shows layering of the alluvial deposits, with the enclosed zones of high K representing clay lenses.

This section shows a slight correlation with (or at least does not appear to contradict) sparse information available from borehole and terrain conductivity surveys (Figure 55). The low-resistivity portions of the bottom layer in Figure 54 roughly correspond to the low-resistivity regions in the borehole section of Figure 55. Likewise, the pattern of high and low resistivity in the top layer and lenses of Figure 54 roughly corresponds to the resistivity pattern of the top layer in the terrain conductivity section.

Overall, the results of the instrument and inversion program field tests presented here are very satisfying, in that the instrument proved capable of functioning reliably in a variety of climates and the inversion models obtained from the field data are either supported by physical sample measurements and well log information, or are reasonably consistent with parameter values expected for shallow earth media (see Table 1). Although a number of deficiencies were identified during the course of the surveys, given the success of these initial survey tests and the "first generation" experimental nature of the instrument construction and survey procedure, the future potential of this sounding method is very promising.

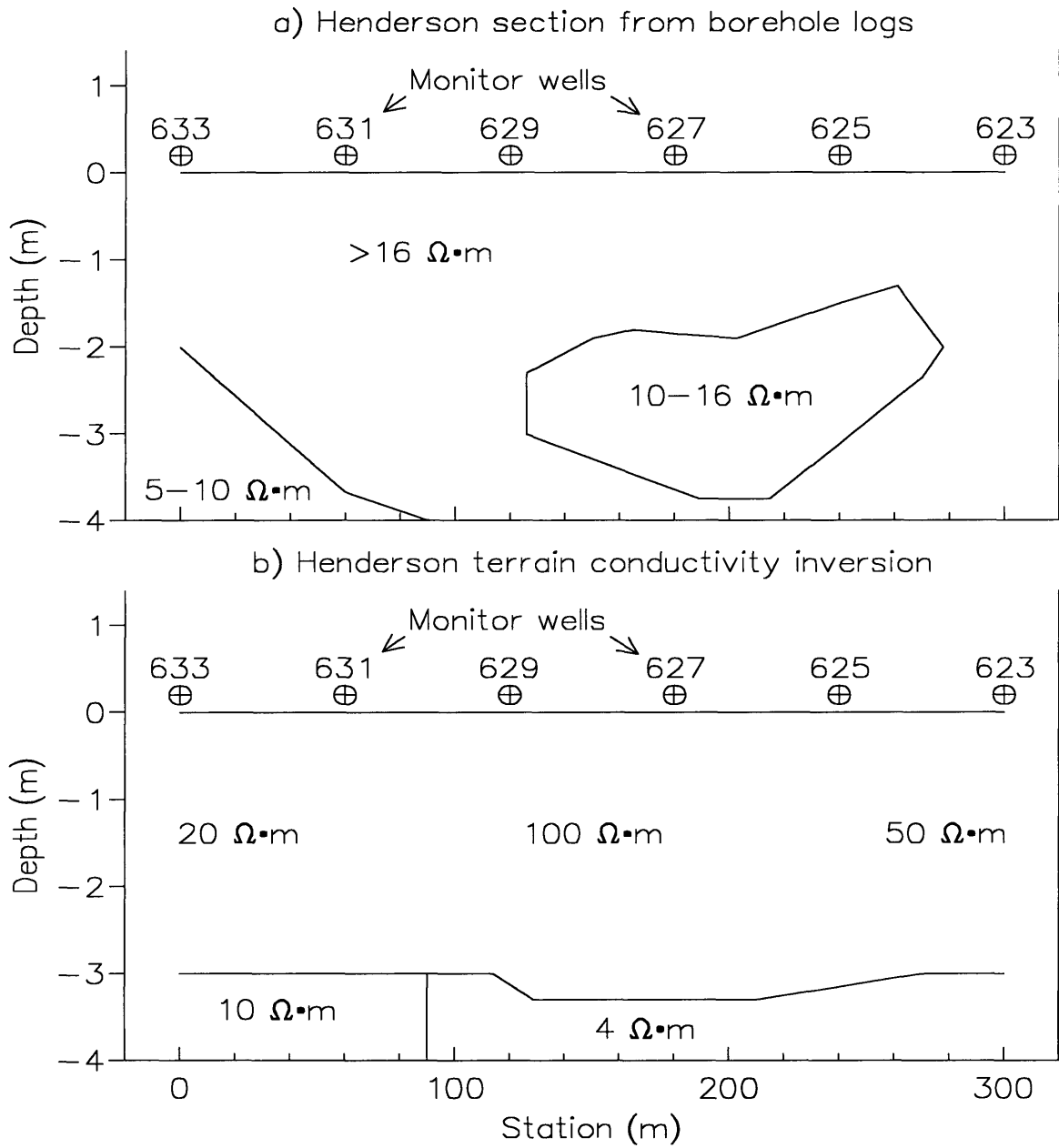


Figure 55. Geoelectric resistivity sections from inversions of (a) borehole induction logs, and (b) terrain conductivity data recorded at Henderson, Nevada. Adapted from Weber and Flatman (1986).

## CONCLUSIONS AND RECOMMENDATIONS

This study has presented the development of a new type of EM sounding for shallow earth mapping applicable to hazardous waste, groundwater, soil engineering, or related areas where investigation of the upper few meters of the subsurface is desired. The particular EM sounding method that was studied uses a horizontal-loop current source placed near the earth's surface, and multiple detection loops placed at short distances from the source. The operational frequency range used was 300 kHz to 30 MHz. Two types of observed field quantities were considered: the polarization ellipse of the total magnetic field, and a quantity based on the spatial gradient of the total vertical magnetic field.

Forward computer programs were used to calculate these quantities for horizontally-layered earth models where the electrical parameters for each layer are electrical conductivity, dielectric permittivity, and thickness. A collection of models and curves was used to examine the influence of selected parameters for various layered-earth cases.

An instrument designed specifically to test this new sounding method was used to collect survey data from a number of sites. The data were interpreted using a computer inversion program which solves for the electrical parameters of a given number of layers. The interpretation results were compared with available data from physical

samples, well logs, and other geophysical methods.

This chapter summarizes the relevant results of this study, and discusses the difficulties and improvements which must be addressed in the continued development of the new method.

### Summary of Method Feasibility

The EM forward models and field survey examples presented indicate that it is possible to measure the properties of electrical resistivity, dielectric permittivity, and layer thickness for shallow earth models.

The forward model examples demonstrate both the importance of dielectric properties at high frequencies, and the potential usefulness of high-frequency sounding for shallow investigation. In particular, the dielectric permittivity influence is shown to enhance the ability to detect and resolve shallow thin layers, regardless of whether the layers have a resistivity or a dielectric contrast. This is especially important for application to pollution problems, because certain contaminants may have a negligible effect on observed  $\rho$ , but a large effect on  $K$ .

The survey examples using the new instrument and computer inversion program demonstrate the feasibility of high-frequency EM sounding and profiling, and illustrate the lack of detailed sounding information provided by terrain conductivity measurements. The high-frequency sounder is designed for good vertical as well as lateral resolution, while terrain conductivity provides mainly lateral resolution.

It is apparent that high-frequency sounding can play a valuable role in shallow earth studies. The method offers good mapping resolution and information on both electrical resistivity and dielectric permittivity values in the subsurface. The results of the field tests show that this method is well within the capabilities of existing electronic and computer technology.

#### Sensitivity Comparison of Polarization Ellipse and Spatial Gradient

Based on the forward models examined in this study, the relative merits of polarization ellipse measurements and spatial gradient measurements are evaluated by assigning each an arbitrary rating of "good", "fair", or "poor" for their response to the different types of models. It must be kept in mind that this rating applies only to the specific types of models presented here, and may not be valid for other combinations of parameters. The basis for each rating is as follows:

**Good:** The separation of the model curves is well within the instrument resolution limit for all values of the variable parameter. Ideally, this condition exists for a broad frequency range, and for both plotted quantities, i.e., both the tilt angle and the ellipticity of the polarization ellipse, or both the amplitude and the phase of the spatial gradient.

**Fair:** The separation of the model curves is at least marginally within the instrument resolution limit for most assigned values of the variable parameter.

**Poor:** The curve separations are outside the instrument resolution limit for all

values of the variable parameter, or are such that only the difference between the largest and the smallest values is resolvable.

Clearly, the absolute rating scale is determined by the measuring sensitivity of the existing instrument. Although the absolute rating for a given case might change if the instrument sensitivity were improved (e.g., a rating of "poor" might become "fair"), the comparative (relative) rating of polarization ellipse versus spatial gradient measurements should not change; a quantity which is rated better than another should still rate better regardless of instrument sensitivity. A real-world factor which might affect comparative ratings is EM interference. A measurement which is rated "good" because of high sensitivity over a particular band of frequencies will be useless if there is excessive noise in that same frequency band.

Half-Space Models: Determination of  $\rho$  or  $K$ . Recommended measurement: either. Both the polarization ellipse and the spatial gradient data are rated "good" for determination of the electrical parameters of a half-space. In the case of determining  $K$  for a relatively conductive half-space, the loss of sensitivity to small values of  $K$  reduces the rating of both to "fair".

Two-Layer Models: Determination of  $h$ . Recommended measurement: spatial gradient. If the top layer is relatively resistive, the spatial gradient data are rated "good" for top

layer thicknesses up to  $h = 5r$ , and "poor" for larger  $h$ . The polarization ellipse data are rated "good" for thicknesses up to  $h = 0.25r$ , and "poor" for larger  $h$ . If the top layer is relatively resistive, the spatial gradient data are "good" up to  $h = 5r$ , and the polarization ellipse data are "good" up to  $h = 0.5r$ . In both cases, the spatial gradient sees the effect of  $h$  to the largest depth.

Two-Layer Models: Determination of  $\rho_2$ . Recommended measurement: spatial gradient. The spatial gradient data are rated "good" for either of the fixed values of  $h$ , regardless of whether the top layer is relatively resistive or conductive. For the top layer thickness of  $h = 0.25r$ , the polarization ellipse data are rated "good" if the top layer is relatively resistive, and "fair" if the top layer is relatively conductive. When the top layer thickness is increased to  $h = 0.5r$ , the ratings for the polarization ellipse data decline respectively to "fair" and "poor".

Two-Layer Models: Determination of  $K_2$ . Recommended measurement: both. For  $h = 1$  m, the polarization ellipse and the spatial gradient sensitivity are complementary; both are needed to assure the ability to resolve  $K_2$ . The polarization ellipse data are rated "fair" if the top layer is relatively resistive, and rated "poor" if the top layer is relatively conductive. Conversely, the spatial gradient data are rated "poor" if the top layer is resistive, and "fair" if it is conductive. Both the polarization ellipse and the spatial gradient data are rated "poor" for  $h > 1$  m.

Three-Layer Models: Determination of  $h_2$ . Recommended measurement: polarization ellipse. The polarization ellipse data are rated "good" for all of the different parameter combinations examined. The spatial gradient data are rated "poor" for all combinations.

Three-Layer Models: Determination of  $\rho_2$ . Recommended measurement: either. Both the polarization ellipse and the spatial gradient data are rated "fair" for the given model.

Three-Layer Models: Determination of  $K_2$ . Recommended measurement: polarization ellipse. The polarization ellipse data are rated "good" for the given model; the spatial gradient data are rated "fair".

#### Recommendations For Future Work

The prototype instrument and computer programs used in this study present a number of obstacles to the efficient application of the method. Most of the problems are a natural result of the process of investigating a previously unused method. The development of the instrument and computer programs, and the selection of operational techniques, was not a predetermined path; instead it was an evolutionary process of setbacks, alternatives, and changed plans. The most desirable and practical approach at this point is to redesign the method "from scratch", using the lessons and information obtained to date.

### Instrument

The present instrument has some operational and design inadequacies which must be improved in future upgrades. The most serious difficulties are: low signal strength for coil spacings larger than 3 m, severe data scatter at frequencies above 20 MHz, poor quality of tilt angle data due to loop misalignment, and coupling effects in the connection wires of the spatial gradient receiver loop array. This last problem (coupling effects) is mainly a result of the somewhat crude "add-on" modification of the instrument for spatial gradient measurements.

Additionally, the forward model studies have shown that the existing upper frequency limit of 30 MHz should be extended to 50 MHz or more to obtain greater sensitivity to dielectric properties and layer thicknesses.

### Computer Inversion Program

The computer inversion program has one drawback that hampers routine production of geoelectric cross-sections. The inclusion of dielectric parameters and use of many frequencies at multiple spacings requires impressive amounts of CPU time for nonlinear least-squares inversion. Using an HP 9000/835 minicomputer, a data set of 48 frequencies for two coil spacings (i.e., two polarization ellipse soundings or a single spatial gradient sounding) may require up to eight minutes to fit a half-space model, and up to two hours to fit a three-layer model. The 18 stations of the Iowa polarization ellipse survey required a total CPU time of about 20 hours for two-layer and three-layer

inversion; the 33 stations of the Iowa spatial gradient survey required about 30 hours.

A fair amount of operator interaction is necessary to work efficiently with the computer inversion program. An inherent feature of inversion algorithms is their tendency to produce models with smooth curves. High-frequency sounding curves often have complicated shapes with sharp peaks and oscillations; purely automatic computer inversion tends to average the oscillations to yield a poorly-fitted model, unless the operator's initial model guess is such that the starting model curves have shapes similar to the field data. Thus, if the inversion appears unable to fit a model to a particular data set, the operator must experiment with the degree of layering and the layer parameters to determine whether the data does not represent a layered-earth, or whether the program is converging to a poorly-fitted local minimum rather than to the "best fit" global minimum.

Obviously, a means for rapid estimation of model parameters is needed for obtaining a reasonable first guess for the inversion program, and for on-the-spot use in the field. For a simple half-space, an estimate of  $K$  can be obtained directly from ellipticity curves if a sharp peak can be identified in the data. This approach may be used for a rough estimate of a  $K$  value of some layers in a multiple-layer model. For example, the 4 m ellipticity data of the CSM survey (Figure 42) has a peak at a frequency of 16.5 MHz. In the graph of Figure 10, 16.5 MHz corresponds to a  $K$  value near 50; the second layer of the CSM survey has a measured  $K$  of 41.

It should be noted that *Anderson* (1991) has partially addressed the accuracy and

efficiency issues by using complex image theory to rapidly approximate least-squares solutions for high-frequency sounding. This approach can be used with PCs in the field for quick reconnaissance work. It must also be noted that the assumption of a 1-dimensional layered earth is not always valid for modeling. As with any geophysical method, the ideal interpretation scheme would accommodate full 3-dimensional earth models.

## REFERENCES

Anderson, W.L., 1982, Adaptive nonlinear least-squares solution for constrained or unconstrained minimization problems (subprogram NLSOL): *U.S. Geol. Surv. Open-File Report* 82-68.

\_\_\_\_\_ 1984, A general interface for producing forward solution programs (subprogram FWDSOL): *U.S. Geol. Surv. Open-File Report* 84-348.

\_\_\_\_\_ 1989, A hybrid fast Hankel transform algorithm for electromagnetic modeling: *Geophysics*, **54**, 263-266.

\_\_\_\_\_ 1991, Approximate inversion of high-frequency electromagnetic soundings using complex image theory: *Geophysics*, **56**, 1087-1092.

Anderson, W.L., Labson, V.F., and Mazzella, A.T., 1990, High-frequency electromagnetic modeling for hazardous waste site detection - a preliminary study: *Technical Research Brief submitted to EPA*.

Beres, M., and Haeni, F.P., 1991, Application of ground-penetrating radar methods in hydrogeologic studies: *Ground Water*, **29**, 375-386.

Birchak, J.R., Gardner, C.G., Hipp, J.E., and Victor, J.M., 1974, High dielectric constant microwave probes for sensing soil moisture: *Proc. IEEE*, **62**, 93-98.

Bitterlich, W., and Kellner, A.W., 1970, Determination of electric rock parameters from the field structure of a magnetic dipole: *Geophys. Prosp.*, **18**, 516-549.

Davis, J.L., and Annan, A.P., 1989, Ground-penetrating radar for high-resolution mapping of soil and rock stratigraphy: *Geophys. Prosp.*, **37**, 531-551.

Dennis, J.E., Gay, D.M., and Welsch, R.E., 1981, An adaptive nonlinear least-squares algorithm: *ACM Trans. on Math. Software*, **7**, 348-368.

Epp, L.W., Mitra, R., and McCormack, R.G., 1988, Summary of methods for measuring electrical properties of geological strata to estimate electromagnetic shielding effectiveness: *U.S. Army Corps Eng., CERL Tech. Rpt. M-88/07*.

Fraser, D.C., Stodt, J.A., and Ward, S.H., 1990, The effect of displacement currents on the response of a high-frequency helicopter electromagnetic system, in Ward, S.H., Ed., *Geotechnical and environmental geophysics, Vol. 2.*, Tulsa: Soc. Expl. Geophys., 89-95.

Frischknecht, F.C., Labson, V.F., Spies, B.R., and Anderson, W.L., 1991, Profiling methods using small sources, in Nabighian, M.N., Ed., *Electromagnetic methods in applied geophysics, Vol. 2.* Tulsa: Soc. Expl. Geophys., 105-270.

Fuller, J.A., and Wait, J.R., 1972, High-frequency electromagnetic coupling between small coplanar loops over an inhomogeneous ground: *Geophysics*, **37**, 997-1004.

Greenhouse, J.P., and Slaine, D.D., 1983, The use of reconnaissance electromagnetic methods to map contaminant migration: *Ground Water Monitoring Review*, **3**, No. 1, 47-59.

Grover, T.P., and Stewart, D.C., 1990, Short wave loop-loop sounder: *U.S. Geol. Surv. Open-File Report* 90-318.

Hayes, P.K., 1982, A single probe on-site method of measuring the dielectric constant and conductivity of soft earth media over a 1-GHz bandwidth: *IEEE Trans. Geosci. Electr.*, **GE-20**, 504-510.

Hipp, J.E., 1974, Soil electromagnetic parameters as functions of frequency, soil density, and soil moisture: *Proc. IEEE*, **62**, 98-103.

Hoekstra, P., and Blohm, M.W., 1990, Case histories of time domain electromagnetic soundings in environmental geophysics, in Ward, S.H., Ed., *Geotechnical and environmental geophysics, Vol. 2*: Tulsa: Soc. Expl. Geophys., 1-15.

Javid, M., and Brown, P.M., 1963, *Field analysis and electromagnetics*. New York: McGraw-Hill Inc.

Katsube, T.J., 1974, Depth of penetration study for high-frequency EM soundings: *Geol. Surv. Can.*, Paper 74-1B, 97-102.

\_\_\_\_\_, 1975, The critical frequency and its effect on EM propagation: *Geol. Surv. Can.*, Paper 75-1A, 101-105.

Kaufman, A.A., and Keller, G.V., 1983, *Frequency and transient soundings*: New York: Elsevier Science Publ. Co., Inc.

Keller, G.V., 1987, Rock and mineral properties, in Nabighian, M.N., Ed., *Electromagnetic methods in applied geophysics, Vol. 1*: Tulsa: Soc. Expl. Geophys., 13-51.

Knight, R.J., and Nur, A., 1987, The dielectric constant of sandstones, 60 kHz to 4 MHz: *Geophysics*, **52**, 644-654.

Kuth, C., and Neubauer, F.M., 1988, Multifrequency inversion of induction logs: *Geophys. Prosp.*, **36**, 66-82.

Lytle, J.R., 1974, Measurement of earth medium electrical characteristics - techniques, results, and applications: *IEEE Trans. Geosci. Electr.*, GE-12, 81-101.

Lytle, J.R., Lager, D.L., and Laine, E.F., 1976, Subsurface probing by high-frequency measurements of the wave tilt of electromagnetic surface waves: *IEEE Trans. Geosci. Electr.*, GE-14, 244-249.

McNeill, J.D., 1980, Electromagnetic terrain conductivity measurement at low induction numbers: *Tech. Note TN-6*, Geonics Ltd.

\_\_\_\_\_, 1990, Use of electromagnetic methods for groundwater studies, in Ward, S.H., Ed., *Geotechnical and environmental geophysics, Vol. 2*: Tulsa: Soc. Expl. Geophys., 191-218.

\_\_\_\_\_ 1993, Written Communication.

Miller, R.D., and Steeples, D.W., 1990, Reflections from geologic interfaces shallower than 30 m at the Pittman lateral, Henderson, Nevada: *60th Ann. Internat. Mtg, Soc. Expl. Geophys., Expanded Abstracts*, 393-396.

Morrison, H.F., Phillips, R.J., and O'Brien, D.P., 1969, Quantitative interpretation of transient electromagnetic fields over a layered half space: *Geophys. Prosp.*, 17, 82-101.

Nabighian, M.N., Ed., 1991, *Electromagnetic methods in applied geophysics, Vol 2*: Tulsa: Soc. Expl. Geophys.

Olhoeft, G.R., 1986, Direct detection of hydrocarbon and organic chemicals with ground penetrating radar and complex resistivity: *Proc. NWWA/API Conf. on Petroleum Hydrocarbons and Organic Chemicals in Ground Water*, Nov. 12-14, Houston, TX, 284-304.

Poley, J., Nooteboom, J.J., and de Waal, P.J., 1978, Use of VHF dielectric measurements for borehole formation analysis: *The Log Analyst*, 19, No. 3, p. 8-30.

Ryu, J., Morrison, F.H., and Ward, S.H., 1970, Electromagnetic fields about a loop source of current: *Geophysics*, **35**, 862-896.

Schmugge, T.J., Jackson, T.J., and McKim, H.L., 1980, Survey of methods for soil moisture determination: *Water Resources Research*, **16**, 961-979.

Scott, G.R., 1972, Geologic map of the Morrison quadrangle, Jefferson County, Colorado: *U.S. Geol. Surv. Map I-790-A*.

Selig, E.T., and Mansukhani, A.M., 1975, Relationship of soil moisture to the dielectric property: *J. Geotech. Eng. Div., Proc. Am. Soc. Civil Eng.*, **101**, 755-770.

Sinha, A.K., 1977a, Influence of altitude and displacement currents on plane-wave EM fields: *Geophysics*, **42**, 77-91.

\_\_\_\_\_ 1977b, Dipole electromagnetic mapping of permafrost terrains: theoretical developments and computer programs: *Geol. Surv. Can.*, Paper 77-13.

Slichter, L.B., 1951, An electromagnetic interpretation problem in geophysics: *Geophysics*, **16**, 431-449.

Smith, B.D., and Ward, S.H., 1974, On the computation of polarization ellipse parameters: *Geophysics*, **39**, 867-869.

Smith-Rose, R.L., 1933, The electrical properties of soil for alternating currents at radio frequencies: *Proc. Royal Soc. London*, **A-140**, 359-377.

Spies, B.R., 1989, Depth of investigation in electromagnetic sounding methods: *Geophysics*, **54**, 872-888.

Stewart, D.C., Anderson, W.L., Grover, T.P., and Labson, V.F., 1990, A new instrument and inversion program for near-surface mapping: EM sounding and profiling in the frequency range 300 kHz to 30 MHz: *60th Ann. Internat. Mtg., Soc. Expl. Geophys., Expanded Abstracts*, 410-413.

Taherian, M.R., Kenyon, W.E., and Safinya, K.A., 1990, Measurement of dielectric response of water-saturated rocks: *Geophysics*, **55**, 1530-1541.

Topp, G.C., Davis, J.L., and Annan, A.P., 1982, Electromagnetic determination of soil water content using TDR: II. evaluation of installation and configuration of parallel transmission lines: *Soil Sci. Soc. Am. J.*, **46**, 678-684.

Ulriksen, P.F., 1982, *Application of impulse radar to civil engineering*: Ph.D. Thesis, Lund Univ., Sweden.

Wait, J.R., 1951, The magnetic dipole over the horizontally stratified earth: *Can. J. Phys.*, **29**, 577-592.

Wait, J.R., 1954, Mutual Coupling of loops lying on the ground: *Geophysics*, **19**, 290-296.

Wait, J.R., 1982, *Geo-Electromagnetism*. New York: Academic Press, Inc.

Walther, E.G., LaBrecque, D.J., Weber, D.D., Evans, R.B., and Van EE, J.J., 1983, Study of subsurface contamination with geophysical monitoring methods at Henderson, Nevada: *Nat. Conf. on Management of Uncontrolled Hazardous Waste Sites*, Oct. 31-Nov. 2, 1983, Washington, D.C., 28-36.

Ward, S.H., and Dey, A., 1971, Lunar surface electromagnetic sounding, a theoretical analysis: *IEEE Trans. Geosci. Electr.*, **GE-9**, 63-71.

Ward, S.H., and Hohmann, G.W., 1987, Electromagnetic theory for geophysical applications, in Nabighian, M.N., Ed., *Electromagnetic methods in applied geophysics, Vol. 1*: Tulsa: Soc. Expl. Geophys., 131-311.

Weber, D.D., and Flatman, G.T., 1986, Statistical approach to groundwater contamination mapping with EM induction, a case study: *Proc. Surface and Borehole Geophys. Meth. and Ground Water Instrumentation Conf. and Expos.*, Oct. 15-17, 1986, Denver, CO, Nat. Water Well Assoc., p. 315-333.

Weber, D.D., Scholl, J.F., LaBrecque, D.J., Walther, E.G., and Evans, R.B., 1984, Spatial mapping of conductive ground water contamination with electromagnetic induction: *Ground Water Monitoring Review*, **4**, No. 4, 70-77.

Wobschall, D., 1978, A frequency shift dielectric soil moisture sensor: *IEEE Trans. Geosci. Electr.*, **GE-16**, 112-118.